Simulation of organic light emitting devices

Blades, Christopher David James

Award date:
2000

Awarding institution:
University of Bath

Simulation of Organic Light Emitting Devices

Christopher David James Blades

September 2000

Submitted in partial fulfilment of the requirements for the degree of Doctor of Philosophy at the University of Bath, Bath, England

ProQuest LLC
789 East Eisenhower Parkway
P.O. Box 1346
Ann Arbor, MI 48106-1346

Abstract

In this thesis a one dimensional drift diffusion model is developed and used to investigate the operation of organic light emitting devices (OLEDs). The model used consists of both bulk limited and contact limited transport mechanisms. The bulk limited mechanisms include: field and temperature dependent mobilities, space charge limited current, carrier trapping using discrete level traps and bimolecular recombination. The injection limited mechanisms include: thermionic emission diffusion, image force lowering of the Schottky barriers to injection, Fowler-Nordheim tunnelling and variable contact types (Schottky or Ohmic). These mechanisms are outlined in chapter 2 and chapter 4

In chapter 3 the drift diffusion model is introduced and 2 methods (SOR) and (DIRECT) are used to simulate unipolar inorganic Schottky contact device structures. Both models proved successful for unipolar systems but could not be generalised to bipolar Schottky contact devices.

In chapter 4 the first order Newton method of SOLVDE is introduced and used to solve both unipolar and bipolar Schottky contact device structures. The SOLVDE model proved stable for single and dual Schottky contact structures and was generalised to include the organic transport mechanisms detailed in chapter 2.

In chapter 5 simulation results are presented for a device based on the poly(phenylene vinylene) (PPV) organic material. The simulations investigate the effect of device length and temperature on the current-voltage characteristic and comparisons made to experimental data.

In chapter 6 simulation results are presented for a variety of single layer device structures based on the organic material poly(methoxy (ethyl-hexyloxy) phenylene vinylene) (MEHPPV). Investigations into the effect of device length, carrier mobility, barriers to injection and hole trapping on the current-voltage characteristic and the recombination rate profile within the device. Finally a prototype 3 layer heterostructure device is investigated as a possible means of improving device performance using a carrier confinement technique.

To my wife Tessa and daughter Matilda.
and my family Mum, Dad, Mike, Paula, Bev, Paul and Mark,
Thank you for all your encouragement, support and CASH!

Acknowledgements

Firstly I would like to thank Alison Jensen and Mike Weaver for motivating the work in this thesis. I would also like to thank the organics group at Sharp Electronics of Europe Ltd. and at the University of Sheffield for experimental data and useful discussions.

A big thanks goes to all those members of the former device modellers group at UEA. This especially includes Steve Woods, Peter Briggs and Jeremy Watling for moral as well as academic support. I would also like to thank the people in the present modelling group at the University of Bath, Diego Oriato and Simon Martin and to the many people at the University of Bath who gave us a new home after our eviction from UEA (probably due to loud music and nonstop parties).

I would also like to thank the following people who have made the last year something to remember. Diego Oriato for many a stimulating conversation regarding such nonsense as the glass envelope effect. Not to mention feeding me and allowing me to crash in several different rooms without the owners consent! Thanks also to Faz for helping me relocate to Attleborough whilst my wife was in labour, and also for explaining how to be a good Muslim whilst drinking, smoking and womanising. Finally I would like to thank Simon Martin, who has taken over my work in OLEDs, and now has to suffer all the bugs I managed to ignore!

Last but by no means least I would like to thank my wife for putting up with a pennyless student for the last 3 years and for giving birth to our daughter Matilda (not that she had much choice!). I would also like to take this opportunity to thank my mother and father, not to mention my father-in-law, for supporting my constant procrastination with generous lumps of cash.

Contents

Chapter 1

Introduction

Organic light emitting diodes (OLEDs) add a new and exciting dimension to conventional display technologies. Due to their ease of manufacture and current level of device stability they are a candidate for both low and high information content displays[1][2]. In the future OLEDs could offer a low cost high volume solution comparable in efficiency and luminosity to current inorganic technologies[3].

This thesis will concentrate exclusively on conjugated polymers, although the device model can, in general, be applied to other organic materials. The two polymer systems investigated in this thesis are shown in figure 1.1 below.

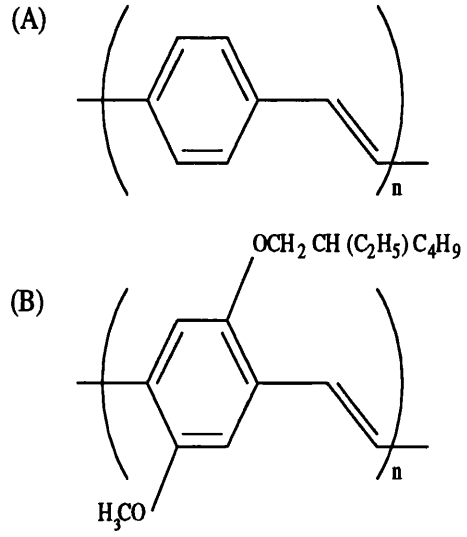

Figure 1.1: Two common polymer structures: (a) PPV and (b) MEHPPV.

Figure 1.1(a) shows poly(phenylene vinylene) (PPV). Figure 1.1(b) shows poly(methoxy (ethylhexoxy) phenylene vinylene) (MEHPPV) which is a soluble form of PPV. There are a number of synthetic routes to PPV, which all produce nominally the same chemical structure. However, the physical properties of the conjugated material depend upon the route used[4].

The semiconducting properties of conjugated polymers arise from the overlap of p_z orbitals that originate from the double or triple bonds[5][6]. Provided this overlap is over several sites, the formation of well delocalised π valence and π^* conduction bands occurs, resulting in a well defined bandgap. These materials therefore exhibit strong intra-chain coupling but quite weak inter-chain coupling, and so to some extent can be considered to be one-dimensional semiconductors. In contrast to inorganic semiconductors, the polymer bands along the chain are so broad that the electrons and holes have masses close to that of the free electron. Additionally, the amorphous nature of polymer structures leads to a broadening of the energies of the chain segments which results in a hopping type transport[7]. However, inorganic models such as: thermionic emission diffusion, Fowler Nordheim tunnelling and space charge limited injection with traps have proved successful in investigating OLEDs[8][9][10][11].

A simplistic view of the operation of OLEDs is therefore based on the following 3 mechanisms: charge injection, carrier transport and recombination. This is shown schematically in figure 1.2 below.

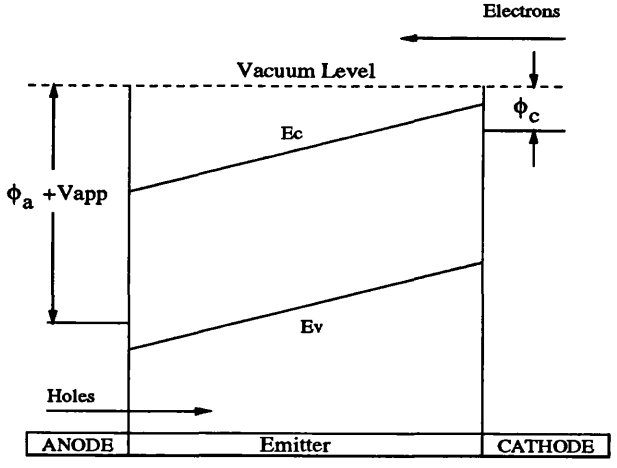

Figure 1.2: Simple OLED device model, where ϕ_a and ϕ_c are the work function of the anode and cathode. E_c and E_v are the conduction and valence bands.

Electrons and holes are injected into the organic emitting layer from the cathode

and anode, respectively. The injected carriers then drift under the influence of the applied electric field and recombine to form excitons, ideally in the centre of the emission layer.

Several carrier injection processes have been suggested, these include: thermionic emission[8][12], field emission[9][13] and space charge limited injection[10][11][14]. The underlying principles for these injection mechanisms are very different. In the case of space charge limited injection, the low carrier mobilities result in a build-up of injected carriers at the contact which limits further injection. Therefore, it is the carrier mobilities that determine the device operating voltage and ultimately limit performance. However, for field emission and thermionic emission it is the barriers to injection that determine the operating voltage indicating that lower work function metals are required to improve device performance. For bulk transport it is the low carrier mobility that place a fundamental limit on the rate at which the carriers can be moved away from the injecting contact. In PPV conjugated polymers the hole mobility is known to be greater than the electron mobility which has been attributed to the presence of electron trapping [11] leading to a dispersive electron mobility. Therefore, a key improvement to OLED performance will be in the development of efficient electron and hole transport materials[3]. A wide variety of hole transport materials have been studied but at present there are relatively few electron transport materials due to the low electron affinities of organics. Electron transport materials include tris-hydroxy-quinoline-aluminum Alq_3 and cyano-substituted PPV's (CN – PPV).

Figure 1.3 shows 3 example OLED geometries. Geometry (a) consists of a single layer of emitting material sandwiched between the electron and hole injecting contacts and represents the simplest device to manufacture. The principle aim is to achieve balanced electron and hole injection into the emission layer, assuming the carrier mobilities are sufficiently high to prevent space charge limited injection, but not so high that carriers exit the device before having the opportunity to recombine. If these condition were achieved then this structure could in principle be very efficient. However, in single layer devices, the carrier mobilities are not generally balanced and are low enough to be a cause of space charge limited injection. In addition it is difficult to form high quality electron injecting contacts, as reactive low work function materials, are needed to ensure a good match to the polymer electron affinity. These problems lead to poor device efficiency as the recombination rate is limited by the carrier with the lower mobility, see

chapter 6.

Figures 1.3(b) and (c) introduce transport layers in an attempt to compensate for the mismatched mobilities and barriers to injection. For example a hole transport layer (HTL) is designed to enhance the hole mobility, improve the barrier to injection for holes and to block electrons. In this fashion, carrier confinement of electrons and holes is achieved at either the transport layer/emission layer boundary (device (b)) or within the emission layer (device (c)).

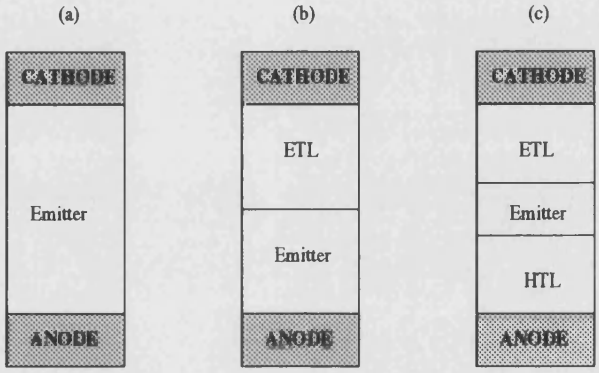

Figure 1.3: Example OLED device structures: single layer geometry (a), two layer geometry (b) and three layer geometry (c).

To date, no single mechanism can adequately describe the behaviour of OLED devices. Therefore, a device model that treats all transport mechanisms on an equal footing is required.

In chapter 2 transport mechanisms that have been suggested as important in OLEDs will be detailed. In chapter 3 the simulation method, a one-dimensional drift diffusion model, will be presented and two unipolar methods evaluated. In Chapter 4 a bipolar model will be developed and tested against inorganic device data. This model will then be generalised to include the transport mechanisms associated with OLEDs. In chapter 5 simulation results for device length and temperature dependence will be presented and compared to experimental current-voltage data. In chapter 6 a single layer OLED will be investigate for the carrier mobilities, barriers to injection, carrier trapping and device length dependence. In addition results will be presented for an optimised single layer OLED and a 3 layer heterostructure similar to that shown in figure 1.3(c).

References

[1] D. D. C. Bradley, *Synthetic Metals*, **54**, 401-415, 1993.

[2] J. H. Burroughs, D. D. C. Bradley, A. R. Brown, R. N. Marks, K. Mackay, R. H. Friend, P. L. Burns and A. B. Holmes, *Nature*, **347**, 539-541, 19990.

[3] L. J. Rothberg and A. J. Lovinger, *Journal of Material Research*, **85**, 3174-3187, 1996.

[4] R. N. Marks, *Ph.D. Thesis*, University of Cambridge, Downing College, (1993).

[5] R. Friend, D. Bradley and A. Holmes, *Physics World*, November 1992.

[6] CDT Technology Ltd. (1999).[WWW] http://www.cdtltd.co.uk/TechnologyBackgrounder.htm (February 1999).

[7] CDT Technology Ltd. (2000).[WWW] http://www.cdtltd.co.uk/technologyBanner.htm (August 2000).

[8] P. S. Davids, I. H. Campbell and D. L. Smith, *Journal of Applied Physics*, **82**, 6319-6325, 1997.

[9] I. D. Parker, *Journal of Applied Physics*, **75**, 1656-1666, 1993

[10] P. W. M. Blom, M. J. M. Vleggaar, *Applied Physics Letters*, **68**, 3308-3310, 1996.

[11] . A. J. Campbell, D. D. C. Bradley and D. G. Lidzey, *Journal of Applied Physics*, **82**, 6326-6342, 1997.

[12] I. H. Campbell, P. S. Davids and D. L. Smith, *Applied Physics Letters*, **72**, 1863-1865, 1998.

[13] J. M. Lupton and I. D. W. Samuel, *Journal of Physics D: Applied Physics*, **32**, 2973-2984, 1999.

[14] Y. Kawabe, M. M. Morrell, G. E. Jabbour, S. E. Shaheen, B. Kippelen and N. Peyghambarian, *Journal of Applied Physics*, **84**, 5306-5314, 1998.

Chapter 2

Charge Injection and Transport

Charge injection and carrier transport mechanisms, which determine the behaviour of organic light emitting devices (OLEDs) are still an area of debate. The mechanisms are identified by fitting analytical models to experimental data [1] [2] [3] and numerical simulation of device structures [4] [5] [6][7]. Two distinct categories exist: injection limited and bulk dominated processes.

When two semiconductor materials with differing electron affinities, or a semiconductor and a metal, are brought into contact a potential barrier will be formed that acts to limit the current flow. In OLEDs it is usually the case that one or both contacts form potential barriers to carrier injection [6] [8]. It is therefore necessary to consider the metal semiconductor interface in detail for our device model. There are two basic processes whereby carriers may cross a potential barrier, namely thermionic emission, where carriers with sufficient energy can surmount the potential barrier, and field emission where carriers can tunnel through the potential barrier. Therefore, the metal semiconductor interfaces and the two dominant carrier injection mechanisms will be covered in this chapter.

In the case where the contact has no significant effect upon the current flow then the bulk properties of the material will dominate. For OLEDs, and in particular PPV where no significant dopants are introduced, space charge limited current (SCLC) will dominate. Therefore, injected carriers will dominate the current flow and the build up and diffusion of space charge, due to the low carrier mobilities, will limit the injection rates at the contacts. Due to the amorphous nature of

organic materials, the existence of both electron and hole trapping have been suggested[2] [3] and will be considered along with SCLC in this chapter.

Analytical models for injection limited and bulk limited current flow will be discussed in terms of a electron only device, although for much of the work in later chapters, a bipolar model will be used to investigate recombination and electroluminescence. Therefore the carrier processes for hole dominated devices will be detailed where necessary.

2.1 Overview of Device Contacts

Metal semiconductor junctions can exhibit ohmic or rectifying behaviour, where the exact nature will be determined by the work function of the metal (ϕ_m) and the quasi-Fermi potential (ϕ_s) within the semiconductor material.

Figures 2.1a and 2.1b show the barrier formation for a metal semiconductor Schottky junction diode. For panel (a), as the metal is brought into contact with the semiconductor material, thermal equilibrium will be established and the Fermi levels in the metal and semiconductor will be continuous and equal through both materials. In order for the Fermi levels to align, electrons from the semiconductor must transfer to the metal leaving behind ionised donors (positive charges) in the semiconductor. Therefore the bands bend down as shown in figure 2.1a and a Schottky junction diode, will be formed provided $\phi_m > \phi_s$ for n-type semiconductor. In the case of p-type semiconductor, a Schottky junction diode will be formed provided $\phi_m < \phi_s$ (figure 2.1b), where electrons are injected into the semiconductor from the metal causing a negative charge on the semiconductor side.

The barrier heights (ϕ_{Bn} and ϕ_{Bp}) as a first approximation can be considered to be largely independent of the field and can be calculated by the following expressions

$$q\phi_{Bn} = q\phi_m - \chi_c \tag{2.1}$$

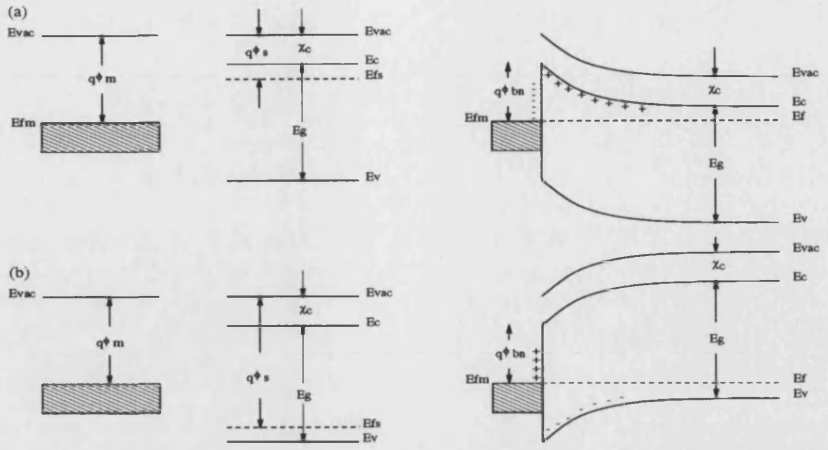

Figure 2.1: Formation of a metal-semiconductor Schottky contact device for (a) an n-type semiconductor material and (b) a p-type semiconductor material.

$$q\phi_{Bp} = E_g - q\phi_{Bn}, \tag{2.2}$$

where ϕ_{Bn} and ϕ_{Bp} are the barriers to electron and hole injection from the metal to the semiconductor respectively and χ_c is the electron affinity of the semiconductor material. In a similar manner the built-in potential can be determined, which is the barrier to carrier transport from the semiconductor to the metal

$$qV_{bi} = q\phi_m - q\phi_s, \tag{2.3}$$

where V_{bi} is the built-in potential. The depletion width W can be calculated in a similar manner to that of a p^+n junction diode, as there is no depletion in the metal. Assuming no mobile charge in the depletion region and charge neutrality outside this region, the solution to Poisson's equation gives

$$E(x) = -\frac{qN_d}{\epsilon_0\epsilon_s}(W - x) \tag{2.4}$$

$$W = \sqrt{\frac{2\epsilon_0\epsilon_s(V_{bi} - V_{app})}{qN_d}}, \tag{2.5}$$

where $E(x)$ is the field profile through the depletion region. The donor density

is N_d and V_{app} is the applied potential.

An ohmic contact can be formed at a metal semiconductor junction. For an ohmic contact two approaches are possible. Firstly if a metal work function is chosen that is less than that of the n-type semiconductor material then no barrier will be formed to carrier injection. However, this is not usually the approach taken, as the barrier height will be pinned by the high interface state density at the contact [23]. A practical ohmic contact uses a metal semiconductor interface that is identical to the Schottky junction diode discussed above. For an ohmic contact to be formed the semiconductor is heavily doped at the interface, which produces a narrow depletion width and a potential barrier that is thin enough for carriers to easily tunnel through.

2.2 Forward and Reverse Bias Operation

Figures 2.2a and 2.2b depict the conduction band profiles for a metal contact on a n-type semiconductor material for forward and reverse bias respectively. If the device is forward biased the potential barrier to electron flow from the semiconductor to the metal ($J_{s\rightarrow m}$) is reduced and the current density increases; additionally the depletion width reduces in accordance with equation (2.5). The potential barrier to electrons from the metal to the semiconductor ($J_{m\rightarrow s}$) is independent of the applied electric field, if image forces are neglected. It can therefore be considered as a fixed contribution to the current flow which will be balanced exactly at thermal equilibrium by $J_{s\rightarrow m}$. However, for reverse bias the potential barrier to the electron flow from semiconductor to metal increases substantially, as does the depletion width. The dominant limit in reverse bias will therefore be the contribution from ($J_{m\rightarrow s}$).

This leads to a highly asymmetric current-voltage characteristic, shown in figure 2.3, similar to that of a pn junction diode. Although the current-voltage characteristics of these two structures are similar, the Schottky junction diode is dominated by majority carrier transport, whereas minority carrier transport is the dominant transport mechanism for pn junction diodes.

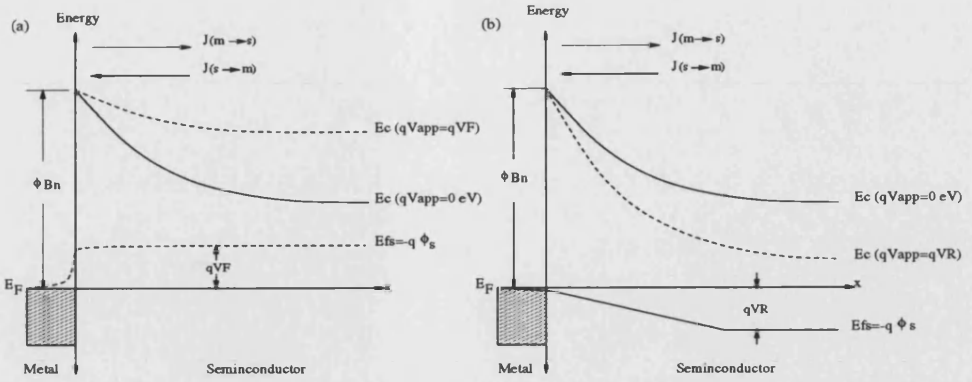

Figure 2.2: Conduction band profiles for a Schottky contact device. Panel (a) shows the band profiles for equilibrium (solid) and forward bias (qV_F) (dashed). Panel (b) shows the band profiles for equilibrium (solid) and reverse bias (qV_R) (dashed).

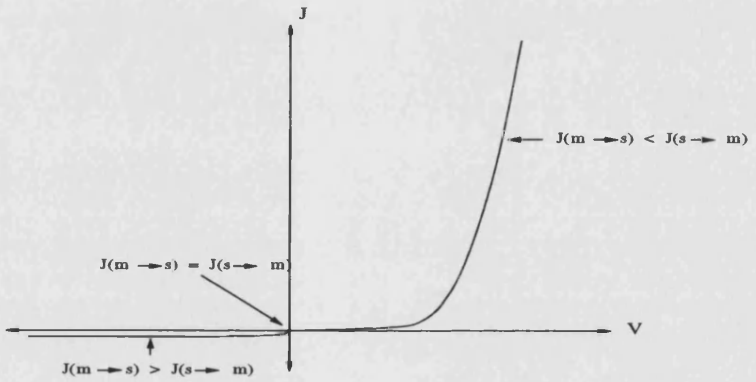

Figure 2.3: Representation of a current density-voltage characteristic for a metal-semiconductor Schottky diode.

2.3 Current Processes in Metal Semiconductor Devices

Figure 2.4 shows the transport mechanisms for a metal semiconductor device under applied bias V. The diagram shows the conduction band (E_c), the valence band (E_v), the Fermi level in the metal (E_F) and the Fermi level in the semiconductor (E_{fs}), with the barrier height ϕ_{Bn} described previously. The image force lowering of this barrier ($\Delta\phi_{Bn}$) will be covered later in chapter 4 section 4.5.

Current transport in metal semiconductor contacts can be separated into four processes, shown in figure 2.4 below for a n-type semiconductor material. These are[10]:

(a) Transport of electrons from the semiconductor over the potential barrier into the metal. This will be the dominant process for moderately doped semiconductors;

(b) Field emission of electrons through the barrier. This process will be important for narrow depletion widths, for example ohmic contacts where the semiconductor is heavily doped;

(c) Recombination in the depletion region;

(d) Recombination in the neutral region.

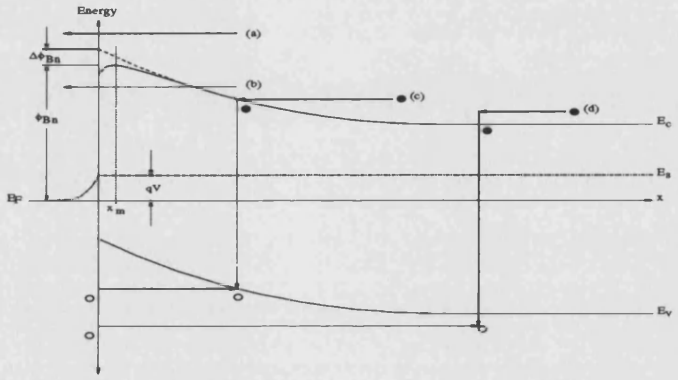

Figure 2.4: Depicted band profile for a Schottky diode under a applied bias (V), showing the conduction band (E_c) the valence band (E_v) and the Fermi level in the semiconductor (E_s) and the metal (E_F) (Reproduction of diagram in S.M. Sze, *Physics of Semiconductor Devices*, John Wiley and Sons, New York (1981), section 5.4[10]).

Two common analytical models for Schottky contact devices will be summarised. Pure thermionic emission theory, where carriers with sufficient energy may surmount the potential barrier at the interface, and diffusion theory where the current in the depletion region depends upon the local field and the carrier concentration gradient. An analytical model that combines these two approaches, thermionic emission diffusion (TED) theory, will be described in detail, where the boundary conditions can be used in our numerical model. As field emission has been suggested as an important process in OLEDs[4] [5] [6] a possible implementation will be discussed.

2.3.1 Thermionic Emission Theory

The assumptions made in thermionic emission theory derived by Bethe are: the barrier height is larger than k_BT; thermal equilibrium is established at the emission plane and that the current flow does not affect the equilibrium at the emission plane. This allows the two current flows $J_{m\to s}$ and $J_{s\to m}$ to be superimposed, therefore the shape of the barrier can be neglected and the current flow will only depend upon the height of the potential barrier[10].

The current flux $J_{s\to m}$ will be dependent upon the concentration of electrons with sufficient energies to overcome the potential barrier. The current flux $J_{m\to s}$ is assumed to be independent of electric field and will therefore be equal and opposite to $J_{s\to m}|_{V=0}$. The total current is the sum of these two components and the net current at thermal equilibrium ($V = 0$) will therefore be zero

$$J_{s\to m} = \int_{E_F+q\phi_{Bn}}^{\infty} qv_x \, \mathrm{d}n \tag{2.6}$$

$$J_{total} = J_{s\to m} + J_{m\to s}, \tag{2.7}$$

where v_x is the carrier velocity in the direction of transport and the lower limit on the integral $E_F + q\phi_{Bn}$ is the minimum energy required for thermionic emission. The current flow from the semiconductor to the metal can be shown to be[10]

$$J_{s\to m} = A^*T^2 \exp(\beta V) \exp(-\beta\phi_{Bn}), \tag{2.8}$$

with the current flow from the metal to the semiconductor given by

$$J_{m\to s} = -A^*T^2 \exp(-\beta\phi_{Bn}), \tag{2.9}$$

where $\beta = \frac{q}{k_BT}$ and $A^* = \frac{4\pi q m^* k_B^2}{h^3}$ is the effective Richardson constant for thermionic emission, k_B is Boltzmann's constant, T is the temperature in Kelvin, m^* is the effective mass, q is the electron charge and h is Plank's constant. Adding

these two current components leads to

$$J_{total} = A^* T^2 \exp\left(-\beta\phi_{Bn}\right)\left[\exp\left(\beta V\right) - 1\right]. \tag{2.10}$$

2.3.2 Diffusion Theory

The current flow in the depletion region is composed of two components: a drift contribution due to the local field and a diffusion contribution due to the carrier concentration gradient. This can be expressed by the drift diffusion equation for electrons

$$J = q\left(\mu_n n(x)E + D_n\frac{\partial n}{\partial x}\right), \tag{2.11}$$

where the diffusion coefficient can be expressed as $D_n = (k_B T/q)\mu_n$. Substituting for $E = -\partial V/\partial x$, the resulting differential equation can be solved by using an integrating factor $\gamma = \exp\left(-qV(x)/k_B T\right)$ to give

$$J\int_0^W \exp\left(-\frac{qV(x)}{k_B T}\right)\mathrm{d}x = qD_n\left[n(x)\exp\left(-\frac{qV(x)}{k_B T}\right)\right]_0^W \tag{2.12}$$

After applying boundary conditions for the electron density (n) and the applied potential (V) at x_m and W, the current density can be shown to be[10]

$$J \approx \frac{q^2 N_c D_n}{k_B T}\left[\frac{q(V_{bi} - V)2N_D}{\epsilon_0\epsilon_s}\right]^{1/2}\exp\left(-\beta\phi_{Bn}\right)\left[\exp\left(\beta V\right) - 1\right], \tag{2.13}$$

which can be further simplified by substituting for D_n and $E(x = 0)$

$$J \approx qN_c\mu_n E(x = 0)\exp\left(-\beta\phi_{Bn}\right)\left[\exp\left(\beta V\right) - 1\right] \tag{2.14}$$

$$E(x=0) = \sqrt{\frac{2qN_D\left(V_{bi}-V\right)}{\epsilon_0\epsilon_s}} \tag{2.15}$$

2.3.3 Thermionic Emission Diffusion Theory

Thermionic emission diffusion (TED) theory will now be covered in detail. This model uses the concept of an effective recombination velocity at the potential energy maximum, near the metal semiconductor interface (x_m) but within the semiconductor, and was proposed by Crowell and Sze [11] and later used as a boundary condition by Choo et al [12] in a numerical drift diffusion model for Schottky contact devices. Under forward bias, the current density J through the depletion region ($x_m < x < W$) will be given by

$$J_D = -q\mu_n n\frac{\mathrm{d}\phi_n}{\mathrm{d}x}, \tag{2.16}$$

where μ_n is the electron mobility and ϕ_n is the quasi-Fermi level in the semiconductor. Assuming non-degenerate Maxwell Boltzmann statistics, the electron density can be expressed as

$$n = N_c \exp\left[\beta\left(\phi_n - \psi\right)\right], \tag{2.17}$$

where N_c is the density of states in the conduction band and ψ is the electrostatic potential.

Assuming that the barrier interface region ($0 < x < x_m$) acts as a perfect sink for electrons, then the current flow at x_m can be expressed in terms of an effective recombination velocity v_{rn} at the potential energy maximum

$$J_b = qv_{rn}\left(n - n_{eq}\right), \tag{2.18}$$

where J_b is the current density at x_m and n_{eq} is the equilibrium electron density. Using equations (2.16), (2.17) the electron density can now be eliminated

$$\frac{J_D}{q\mu_n N_c}\exp\left(-\beta\psi\right) = \exp\left(-\beta\phi_n\right)\frac{\mathrm{d}\phi_n}{\mathrm{d}x}. \tag{2.19}$$

Separating the differential in ϕ_n, on the right hand side of equation (2.19), and integrating from x_m to W leads to

$$\frac{J_D}{\mu_n k_B T N_c} I^{\psi} = \exp\left(\beta V\right) - \exp\left(-\beta\phi_n(x_m)\right) \tag{2.20}$$

$$I^{\psi} = \int_{x_m}^{W} \exp\left(-\beta\psi\right)\mathrm{d}x. \tag{2.21}$$

Here we have assumed that the quasi-Fermi level at the depletion width edge will be equal to the applied potential. Using equation (2.18) and eliminating $\phi_n(x_m)$ from the right hand side of equation (2.20) gives

$$\frac{J_D}{\mu_n k_B T N_c} I^{\psi} = \exp\left(\beta V\right) - \left[\frac{J_b}{qV_{rn}N_c}\exp\left(\beta\phi_{Bn}\right) + 1\right], \tag{2.22}$$

which can be rearranged into the following expression using conservation of current ($J = J_D = J_b$)

$$J = \frac{qN_c v_{rn}}{1 + v_{rn}/v_{dn}}\exp\left(-\beta\phi_{Bn}\right)\left[\exp\left(-\beta V\right) - 1\right], \tag{2.23}$$

where v_{dn} is an effective diffusion velocity associated with the transport of electrons from the edge of the depletion layer to the potential energy maximum.

$$v_{dn}^{-1} = I^{\psi}\frac{q}{\mu_n k_B T}\exp\left(\beta\phi_{Bn}\right) = \int_{x_m}^{W}\frac{q}{\mu_n k_B T}\exp\left[\beta\left(\phi_{Bn} + \psi\right)\mathrm{d}x\right]. \tag{2.24}$$

The effective recombination velocity (v_{rn}) is given by equation (2.25) below. If the electron distribution is Maxwellian for ($x \geq x_m$), and if no electrons are backscattered from the metal other than those associated with the current density

$qn_{eq}v_{rn}$, then the semiconductor will act as a thermionic emitter

$$v_{rn} = \sqrt{\frac{k_B T}{2m^* \pi}} = \frac{A^* T^2}{qN_c}. \tag{2.25}$$

There are two possible limiting cases for current density. For the case where $v_{dn} \ll v_{rn}$, then equation (2.23) reduces to the diffusion theory of Schottky

$$J \approx qN_c \mu_n E(x = 0) \exp(-\beta \phi_{Bn}) [\exp(-\beta V) - 1], \tag{2.26}$$

where $E(x = 0)$ is the electric field at the contact, and using the substitution $v_{dn} = \mu_n E$ for field independent mobilities. For the case where $v_{dn} \gg v_{rn}$, then equation (2.23) reduces to the thermionic theory of Bethe

$$\begin{aligned} J &\approx qN_c v_{rn} \exp(-\beta \phi_{Bn}) [\exp(-\beta V) - 1] && (2.27) \\ &\approx A^* T^2 \exp(-\beta \phi_{Bn}) [\exp(-\beta V) - 1]. && (2.28) \end{aligned}$$

In summary, the TED model can be viewed as being made up of two currents flowing in series: a diffusion current from the depletion region edge to the potential energy maximum and a thermionic emission current over the barrier. Therefore, it is evident that the smaller of these two processes will be limiting factor for the current density.

2.3.4 Field Emission Theory

There are situations where the contribution to the current flow due to thermionic emission over a potential barrier is small, for example where the barrier to injection is large or the temperature is low [14]. Then in these cases, the current flow will be limited by tunnelling of carriers through the potential barrier. This type of injection is known as field emission or thermally assisted field emission as the current flow is always associated with a high electric field. In OLEDs Fowler

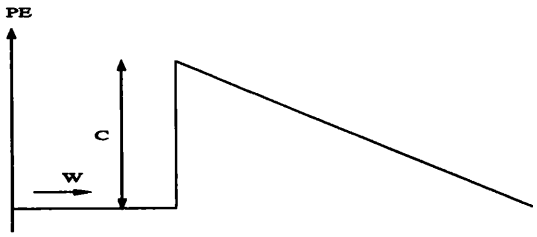

Figure 2.5: Depiction of potential barrier of height C.

Nordheim tunnelling through a triangular barrier has been suggested by many authors[4] [8] [15] [16] [17]. This approach will be covered here.

The current density, due to tunnelling through a potential barrier of height C shown schematically in figure 2.5, can be expressed by[17]

$$J = \frac{16\pi mq}{Ch^3}\int_0^{\mu} W^{1/2}(C-W)^{1/2}(\mu - W)\exp\left(-\frac{4\kappa(C-W)^{3/2}}{3E}\right)\mathrm{d}W. \quad (2.29)$$

Here, μ is the chemical potential, W is the electron kinetic energy normal to the barrier, $\kappa = 8\pi^2 m/h^2$ and E is the electric field. The above equation can be expressed in a more compact form as follows

$$J = \frac{2A}{3\beta}\int_0^{\mu} g(W)\frac{\mathrm{d}f}{\mathrm{d}W}\mathrm{d}W, \quad (2.30)$$

where the following substitutions have been made

$$A = \frac{16\pi mq}{Ch^2} \quad (2.31)$$

$$\beta = \frac{4\kappa}{3E} \quad (2.32)$$

$$f(W) = \exp\left(-\beta(C-W)^{3/2}\right) \quad (2.33)$$

$$g(W) = \left(W^{1/2}\mu - W^{3/2}\right). \quad (2.34)$$

$$(2.35)$$

Integration by parts gives

$$I = -\frac{2A}{3\beta}\int_0^{\mu} \exp\left(-\beta(C-W)^{3/2}\right)\left(\frac{1}{2}W^{-1/2}\mu - \frac{3}{2}W^{1/2}\right) \mathrm{d}W. \tag{2.36}$$

This integral can be solved using the following mean value theorem

$$J = \int_a^b f(x)g(x)\mathrm{d}x \approx g(\zeta)\int_a^b f(x)\mathrm{d}x \quad (a \leq \zeta \leq b). \tag{2.37}$$

Applying this theorem to equation (2.36) and substituting $C = \chi - \mu$ gives

$$J = -\frac{2A}{3\beta}\exp\left(-\beta\chi^{3/2}\right)\int_0^{\mu}\exp\left(-\frac{3\beta}{2}\chi^{1/2}(\mu - W)\right)\left(\frac{\mu W^{-1/2}}{2} - \frac{3W^{1/2}}{2}\right)\mathrm{d}W, \tag{2.38}$$

where χ is the thermionic work function. Equation (2.38) can then be solved to give the familiar Fowler Nordheim equation

$$J \approx \frac{q}{2\pi h}\left(\frac{\mu^{1/2}}{(\chi+\mu)\chi^{1/2}}\right)E^2\exp\left(-\frac{4\kappa\chi^{3/2}}{3F}\right), \tag{2.39}$$

which is commonly expressed as [2]

$$J = \frac{q^3}{8\pi h\phi_B}E^2\exp\left[-\frac{8\pi\sqrt{(2m^*)}}{3qh}\frac{\phi_B^{3/2}}{E}\right]. \tag{2.40}$$

Equation (2.40) is valid for low temperatures. If the carriers tunnel from energies significantly above the Fermi level then a thermally assisted tunnelling model is required. In OLEDs there is evidence that the above expression, for tunnelling is applicable at room temperatures [8].

2.4 Bulk Properties

For the case where one of the injecting contacts is ohmic and the semiconductor is un-doped, then the current flow will be dominated by the injected carriers. The build up and diffusion of the injected space charge in the semiconductor material will control the injection rate at the ohmic contacts. The space charge in the device, as a first approximation, will be proportional to the applied bias. This type of behaviour can be described by single carrier space-charge-limited current (SCLC) flow, which can be generalised to include the effect of traps.

2.4.1 Space Charge Limited Current

In developing the SCLC model the drift diffusion equation will be used, shown previously for electrons in equation (2.11). Several assumptions will be made; firstly the injecting contact is assumed to be ohmic with the other contact acting as an efficient sink for the injected charge. Secondly the diffusion current is assumed to be negligible compared with the drift current. Thirdly the intrinsic carrier density is assumed to be negligible in comparison to the injected charge density. Finally the mobilities are assumed to be field independent. Therefore the electron drift diffusion equation can be simplified to

$$J = q\mu_n nE(x) = \text{constant}. \tag{2.41}$$

Using Poisson's equation, shown below, the field can be linked to the background charge density. Here n and n_{tj} are the electron density and the trapped electron density at the j^{th} discrete trap energy level respectively and ϵ is the permittivity of the semiconductor

$$\frac{\mathrm{d}E(x)}{\mathrm{d}x} = \frac{q}{\epsilon}\left(n - n_0 + \sum_j (n_{tj} - n_{tj0})\right). \tag{2.42}$$

Assuming that the insulating material is trap free and there are no thermally free carriers n_0; substituting equation (2.41) into equation (2.42) for n leads to

$$\frac{J}{q\mu_n\epsilon} = E\left(\frac{\mathrm{d}E}{\mathrm{d}x}\right), \tag{2.43}$$

which can be easily integrated to form

$$E(x) = \left(\frac{2J}{\epsilon\mu_n}\right)^{\frac{1}{2}} x^{\frac{1}{2}}, \tag{2.44}$$

where the boundary condition $E(0) = 0$ has been used. Substituting for $E = -\mathrm{d}V/\mathrm{d}x$, in the above equation, and applying the boundary condition $V(L) = V_{app}$ leads to the trap free square law (TFSL) for current injection into insulators [13]

$$\begin{aligned} V(x) &= \sqrt{\left(\frac{2J}{\epsilon\mu_n}\right)}\int_0^x x^{\frac{1}{2}}\mathrm{d}x \\ J &= \frac{9}{8}\epsilon\mu_n\left(\frac{V_{app}^2}{L^3}\right). \end{aligned} \tag{2.45}$$

If there are n_0 thermal free carriers per volume then Ohm's law will dominate the current behaviour for low voltages. There will be a transition from Ohm's law to TFSL when the number of charge carriers injected into the material becomes comparable to n_0. This point can be determined by equating the expressions for Ohm's law and TFSL

$$\begin{aligned} \left(\frac{9}{8}\right)\epsilon\mu_n\left(\frac{V_\omega^2}{L^3}\right) &= q\mu_n n_0\left(\frac{V_\omega}{L}\right) \\ V_\omega &= \left(\frac{8}{9}\right)qn_0\left(\frac{L^2}{\epsilon}\right). \end{aligned} \tag{2.46}$$

2.4.2 Insulator with Traps

The presence of traps in the insulator will result in a reduction of the free carrier density, as a proportion of the injected carriers will be immobilised in the traps. This results in a reduction of the current density. The thermal equilibrium and injected electron densities are given by the following relationship for non-degenerate insulators

$$\begin{aligned} n_0 &= N_c \exp\left[\left(\frac{E_{f0} - E_c}{k_B T}\right)\right] \\ n &= N_c \exp\left[\left(\frac{E_f - E_c}{k_B T}\right)\right], \end{aligned} \tag{2.47}$$

where E_{f0} and E_f are the equilibrium and non-equilibrium Fermi levels. The trapped electron density is given by the Fermi-Dirac expression

$$\begin{aligned} n_{tj0} &= \frac{N_t}{1 + (1/g)\exp\left[\left(\frac{E_t - E_{f0}}{k_B T}\right)\right]} \\ n_{tj} &= \frac{N_t}{1 + (1/g)\exp\left[\left(\frac{E_t - E_f}{k_B T}\right)\right]}, \end{aligned} \tag{2.48}$$

where E_t is the trap energy level below the conduction band edge, N_t is the trap concentration and g the degeneracy factor for the traps. Figure 2.6 shows a representation of the band diagram for thermal equilibrium and under an applied bias, where the equilibrium of the trap occupancy results from a balance between electrons captured by the traps and their thermal re-emission into the conduction band[13].

It is instructive to analyse traps existing at a single energy level, such as those outlined above, where there are two possible distinct cases: shallow and deep traps, represented in figure 2.6(a) and (b) for the shallow trap case and figure 2.6(c) and (d) for the deep trap case. For the shallow trap case $\{(E_t - E_{f0})/k_B T > 1\}$

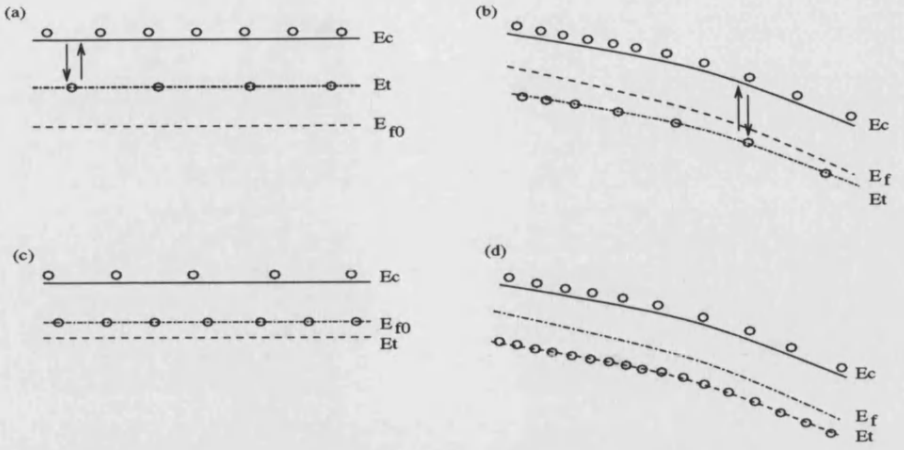

Figure 2.6: Representation of the conduction band E_c, the trap energy level E_t and the Fermi level E_f within the insulator. Shallow Traps: thermal equilibrium (a) and under bias (b). Deep traps: thermal equilibrium (c) and under bias (d).

the majority of the traps will be empty at equilibrium. Under bias the traps will fill or empty dependent upon the relative position of the Fermi level to the trap energy level. For the deep level case $\{(E_{f0} - E_t)/k_BT > 1\}$ the majority of the traps will be filled at equilibrium. The traps rapidly fill to the maximum occupation concentration N_t for an applied bias $V_{app} > 0.7k_BT$. The effect of deep and shallow traps upon the current-density voltage (JV) characteristics are shown schematically in figure 2.7(a) and (b) respectively.

For shallow traps the JV curve initially follows Ohm's law ($J \propto V$). As the Fermi level impinges upon the trap energy level, the traps begin to fill and the JV curve moves onto the shallow trap square law $J \propto V^2$ at $V_{app} = V'_{\omega}$. As the majority of the traps are filled ($E_f > E_t$), injected carriers dominate the current flow, and the JV curve rapidly switches to the TFSL limit at $V_{app} = V_{\omega S}$. For deep traps the JV curve initially follows Ohm's law and rapidly switches to the TFSL limit at ($V_{app} = V_{\omega d}$)

The shallow trap square law relationship can be shown to be[13]

$$J \approx \left(\frac{9}{8}\right)\theta\epsilon\mu_n\left(\frac{V_{app}^2}{L^3}\right), \tag{2.49}$$

where $\theta = n/n_t$. The transition from Ohm's law to the shallow trap square law

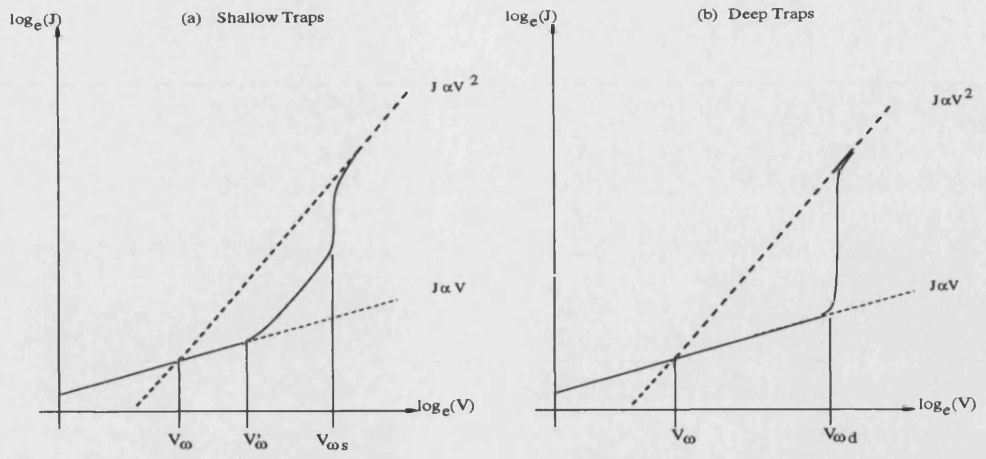

Figure 2.7: Depiction of current-density voltage characteristics for (a) shallow traps and (b) deep traps.

is given by

$$V'_\omega = \frac{8}{9} q n_0 \left(\frac{L^2}{\theta \epsilon} \right), \tag{2.50}$$

and the transition at the trap fill limit, for deep and shallow traps, is given by

$$\begin{aligned} V_{\omega s} &= \frac{8}{9} q N_t \left(\frac{L^2}{\theta \epsilon} \right) \\ V_{\omega d} &= \frac{8}{9} q p_{t0} \left(\frac{L^2}{\epsilon} \right), \end{aligned} \tag{2.51}$$

where p_{t0} is the number of unoccupied traps at thermal equilibrium $(N_t - n_{t0})$

2.5 Conclusion

In this chapter several different carrier transport mechanisms have been discussed. These may be characterised as either contact limited or bulk limited processes. For OLEDs based on the organic material poly(phenylene vinylene)

(PPV) both contact limited and bulk limited mechanisms have been proposed as important. Possible contact limited mechanisms include current injection via thermionic emission and, for high fields, Fowler Nordheim tunnelling. Proposed bulk dominated effects are space charge limited current and trapping of carriers.

To date, no single transport mechanism adequately describes the current-voltage characteristic. The most successful methods, currently used in modelling OLEDs, use a combination of transport mechanisms including: thermionic emission and field emission[4] [16] or space charge limited current with carrier trapping [2] [3]. Therefore, a model that treats these mechanisms on an equal footing is required.

References

[1] L. Bozano, S. A. Carter, J. C. Scott, G. G. Malliaras and P. J. Brock, *Applied Physics Letter*, **74**, 1132-1134, 1998.

[2] A. J. Campbell, D. D. C. Bradley and D. G. Lidzey, *Journal of Applied Physics*, **82**, 6326-6342, 1997.

[3] P. W. M. Blom, M. J. M. Vleggaar, *Applied Physics Letters*, **68**, 3308-3310, 1996.

[4] J. M. Lupton and I. D. W. Samuel, *Journal of Physics D: Applied Physics*, **32**, 2973-2984, 1999.

[5] I. H. Campbell, P. S. Davids and D. L. Smith, *Applied Physics Letters*, **72**, 1863-1865, 1998.

[6] P. S. Davids, I. H. Campbell and D. L. Smith, *Journal of Applied Physics*, **82**, 6319-6325, 1997.

[7] P. W. M. Blom, M. J. M. de Jong, C. T. H. F. Liedenbaum and J. J. M. Vleggaar, *Synthetic Metals*, **85**, 1287-1288, 1997.

[8] I. D. Parker, *Journal of Applied Physics*, **75**, 1656-1666, 1993 .

[9] M. S. Tyagi, *Introduction to Semiconductor Materials and Devices*, John Wiley and Sons, New York (1991).

[10] S. Sze, *Physics of Semiconductors*, John Wiley and Sons, New York (1981).

[11] C. R. Crowell and S. M. Sze, *Solid State Electronics*, **9**, 1035-1048, 1966.

[12] S. C. Choo, *Solid State Electronics*, **38**, 2085-2093, 1994.

[13] M. A. Lampert and P. Marks, *Current injection in Solids*, Academic Press, New York and London, (1970).

[14] R. N. Marks, *Ph.D. Thesis*, University of Cambridge, Downing College, (1993).

[15] Y. Kawabe, M. M. Morrell, G. E. Jabbour, S. E. Shaheen, B. Kippelen and N. Peyghambarian, *Journal of Applied Physics*, **84**, 5306-5314, 1998.

[16] P. S. Davids, Sh. M. Kogan, I. D. Parker and D. L. Smith, *Applied Physics Letters*, **69**, 2270-2272, 1996.

[17] R. H. Fowler and L. Nordheim, *Proceedings of the Royal Society*, **119**, 173-181, 1928.

Chapter 3

Simulation Method

In the last decade the number of approaches used in modelling organic electroluminescent devices (OELDs) has increased. To date there are two common numerical methods: drift diffusion[1][2] and real space based Monte Carlo[3][4]. In addition there are numerous analytical approaches: such as space charge limited current models (SCLC), Pool Frenkel emission and Fowler Nordheim tunnelling [1] [5] [6] [7].

The approaches listed above all have limitations. Semiclassical approaches such as real space Monte Carlo can shed light upon the carrier transport between polymer chains and can be used to study time of flight data but these methods cannot be scaled up to useful device lengths at present. Classical approaches, such as drift diffusion, are inappropriate for short device lengths ($L < 50nm$)[8] but can be used to study entire devices, providing detailed information on internal fields, recombination (light emission) position and magnitude, potential profiles and carrier densities. The experimental data available for poly(para-phenylene-vinylene) PPV and poly(methoxy(ethyl-hexyloxy)-phenylene-vinylene) MEHPPV have well defined hole mobilities and fitting methods such as those outlined above have shown that a rigid band model such as drift diffusion can be used[9].

For the purposes of this thesis we have chosen drift diffusion as our simulation method and this chapter will introduce this numerical method in detail. The drift diffusion equations are outlined in section 3.1. Discretisation and methods

of solving these equations are discussed in sections 3.2 and 3.3, with a selection of results for devices with both ohmic and Schottky contacts given in sections 3.4.1 and 3.4.2 respectively.

3.1 Drift Diffusion Model

The derivation of the drift diffusion equations contain a diffusion term which is dependent upon the carrier concentration gradients, and a drift term which is a function of the local field experienced by the carriers. Coupling Poisson's equation with the drift diffusion equations forms 3 partial differential equations that are highly non-linear and it is this non-linearity that makes numerical solutions both complex and unstable. Analytical approaches to solving the drift diffusion equations are centred around simplifying the equations to find a closed form solution[10]. As the speed and memory size of computers has improved, numerical approaches to solving these equations have largely superceded these earlier techniques. The drift diffusion method has been successfully applied to model the D.C. and A.C. characteristics of a whole range of devices from junction diodes through to heterostructure transistors and beyond. This approach can be readily applied in one, two and even three dimensions without prohibitive simulation times or memory usage.

3.1.1 Current Equations

The drift diffusion equations have their origins in the second moment of the Boltzmann transport equation[11] (BTE). The second moment of the BTE[12] can be expressed as

$$\frac{\partial \mathbf{J}}{\partial t} = \frac{q}{m^*} n\mathcal{F} - \frac{\mathbf{J}}{\langle \tau \rangle} + \frac{q}{m^*} \nabla_r \left(n k_B T \right), \tag{3.1}$$

where $\mathbf{J}$ is the current, q is the electron charge and T is the temperature. $\mathcal{F}$ represents a force, n is the electron density, m^* is the effective mass and k_B is Boltzmann's constant. The drift diffusion equations can be derived by assuming

an isotropic parabolic band and that the energy of carriers are due to thermal contributions only (non-degeneracy and no hot carrier effects). The relaxation time, $\tau_p = \langle \tau \rangle$ is related to the effective electron mobility by

$$\mu = \frac{q\tau_p}{m^*}. \tag{3.2}$$

Substituting equation (3.2) into (3.1), the transport for electrons in an electric field E is given by

$$\tau_p \frac{\partial \mathbf{J}}{\partial t} = q\mu n E - \mathbf{J} + \mu \nabla_r \left(n \; k_B T \right). \tag{3.3}$$

The left hand side of equation (3.3) can be assumed to be zero if the scattering time τ_p is much smaller than the time scales of interest in our devices. Thus in one spatial dimension the drift diffusion equations for electrons and holes can be described by the following equations

$$\mathbf{J}_n = qn\mu_n E + \mu_n k_B T \nabla n \tag{3.4}$$

$$\mathbf{J}_p = qp\mu_p E - \mu_p k_B T \nabla p. \tag{3.5}$$

The electron and hole velocities are given by

$$\nu_n = \mu_n E \tag{3.6}$$

$$\nu_p = \mu_p E. \tag{3.7}$$

This assumption can be relaxed by substituting $\nu_n(E)$ and $\nu_p(E)$ for $\mu_n E$ and $\mu_p E$. $\nu_n(E)$ and $\nu_p(E)$ are obtained from Monte Carlo simulations in the case

of inorganic devices, and analytical fits to experimental time of flight data in organic devices [13] [14]. This is the so called realistic mobility model.

The electron and hole diffusion coefficients (D_n and D_p) are related to the mobilities by Einsteins relationship

$$D_{n,p} = \frac{k_B T}{q} \mu_{n,p}, \tag{3.8}$$

which although derived at thermal equilibrium can be extended to the non-equilibrium case [15].

The electron and hole thermal equilibrium densities are defined by the introduction of quasi-Fermi levels. These are shown below for Maxwell Boltzmann statistics

$$n = N_C \exp\left(\frac{-q\phi_n + q\psi + \chi_c}{k_B T}\right) \tag{3.9}$$

$$p = N_V \exp\left(\frac{q\phi_p - q\psi - \chi_c - E_g}{k_B T}\right), \tag{3.10}$$

where ϕ_n and ϕ_p are the quasi-Fermi potentials within the device and are related to the electron and hole Fermi levels by $E_{fn} = -q\phi_n$ and $E_{fp} = -q\phi_p$ respectively. The 2 drift diffusion equations (3.4) and (3.5), when combined with the carrier density equations, can be expressed in a more stable form suitable for numerical approaches. These are shown below

$$\mathbf{J}_n = -qn\mu_n \nabla \phi_n \tag{3.11}$$

$$\mathbf{J}_p = -qp\mu_p \nabla \phi_p. \tag{3.12}$$

3.1.2 Continuity Equations

The continuity equations for electrons and holes are given below

$$\frac{\partial n}{\partial t} = \frac{1}{q}\nabla \cdot J_n - R + G \tag{3.13}$$

$$\frac{\partial p}{\partial t} = -\frac{1}{q}\nabla \cdot J_p - R + G, \tag{3.14}$$

where R and G are the carrier recombination and generation rates respectively.

The model used in this thesis considers the static D.C. case only. As the carrier concentrations do not vary with time the left hand side of equations (3.13) and (3.14) can be set to zero. The recombination-generation terms depend upon the particular devices modelled and can be made up of 5 separate terms for inorganic devices: i. trapping, ii. impact ionisation, iii. Auger recombination, iv. surface recombination and v. optical recombination. For OLEDs only trapping (R_{SRH}) and optical recombination (R_{OPT}) are important.

For inorganic semiconductors the thermal recombination rate is due to phonon transitions aided by traps, which can be represented by the Shockley-Read-Hall (SRH) model and is shown in equation (3.15) below [16].

$$R_{SRH} = \frac{np - n_i^2}{\tau_n (p + n_i) + \tau_p (n + n_i)}, \tag{3.15}$$

$$n_i^2 = N_C N_V \exp\left[-\frac{E_g}{K_B T}\right]. \tag{3.16}$$

where τ_n and τ_p are the characteristic electron and hole recombination times. The intrinsic charge density n_i is given in equation (3.16); E_g is the energy gap, N_C and N_V are the densities of state in the conduction and valence bands respectively. For optical recombination equation (3.17) is used, where C_{opt} is the optical capture emission rate[17].

$$R_{OPT} = C_{opt}\left(np - n_i^2\right) \tag{3.17}$$

3.1.3 Poisson's Equation

The electrostatic potential associated with a fixed donor and acceptor distribution and mobile electron and hole charge distribution in a semiconductor material is given by Poisson's equation. For a one dimensional device Poisson's equation is given for a heterostructure device by

$$\frac{\mathrm{d}^2\psi}{\mathrm{d}x^2} = -\frac{q}{\epsilon_0\epsilon_s(x)}\left(p - n + N_D^+ - N_A^-\right) - \frac{1}{\epsilon_s(x)}\frac{\mathrm{d}\psi}{\mathrm{d}x}\frac{\mathrm{d}\epsilon_s(x)}{\mathrm{d}x}. \tag{3.18}$$

where N_A^- and N_D^+ are the ionised acceptor impurity concentrations.

One also needs the equations linking the electron and hole densities with the potential. With the non-degenerate statistics assumed here, this is derived from the Maxwell-Boltzmann distribution

$$n = N_C \exp\left[\frac{q}{k_B T}\left(\psi - \phi_n + \frac{\chi_c}{q}\right)\right] \tag{3.19}$$

$$p = N_V \exp\left[-\frac{q}{k_B T}\left(\psi - \phi_p + \frac{E_g}{q} + \frac{\chi_c}{q}\right)\right], \tag{3.20}$$

where χ_c is the electron affinity of the device.

3.2 Discretisation Scheme

Figure 3.1 shows the variable mesh used in the one dimensional model. A 3-point discretisation scheme is used in solving the 3 drift diffusion equations. The mesh consists of an array of i node points and j half node points. The state variables

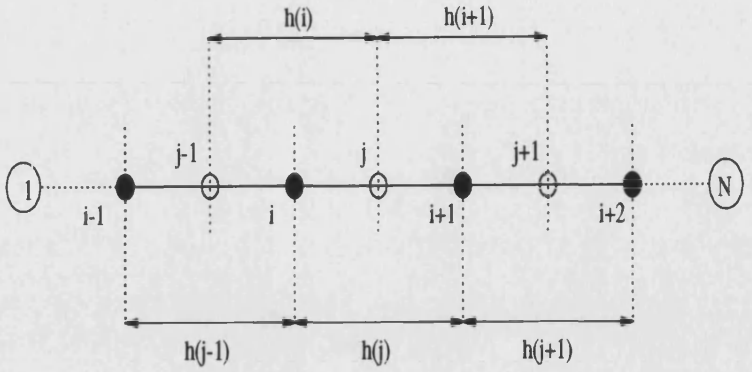

Figure 3.1: One dimensional variable mesh.

n, p and ψ (or related state variables for SOLVDE, see chapter 4) are defined on the i^{th} node points, whereas their derivatives are defined on the j^{th} half node mesh points. The relationship between these mesh points is given by

$$h'(i) = \left(\frac{h(j-1) + h(j)}{2} \right). \tag{3.21}$$

This discretisation scheme increases the accuracy of the 3 point discretisation of the original differential equations and, in principle, should increase the stability of any method used to solve them.

The following approximations for 1st order and 2nd order derivatives at the i^{th} mesh point will be used [18][19]

$$\frac{\mathrm{d}A_i}{\mathrm{d}x_i} = \frac{A_j - A_{j-1}}{h'_i} = \frac{A_{i+1} - A_{i-1}}{h_j + h_{j-1}} \tag{3.22}$$

$$\frac{\mathrm{d}^2 A_i}{\mathrm{d}x_i^2} = \frac{A_{i+1} - 2A_i + A_{i-1}}{h_j h_{j-1}}. \tag{3.23}$$

3.2.1 Discretisation of Poisson's Equation

For the discretisation of Poisson's equation the electric displacement D was used, where D is related to the electric field by

$$D = \epsilon_0 \epsilon_s E. \tag{3.24}$$

Poisson's equation can now be discretised with respect to D, which has the advantage that at a heterojunction D is continuous. Therefore the same discretisation scheme can be used whether considering a homojunction or heterojunction device. In terms of D, Poisson's equation is given by

$$\frac{\mathrm{d}D}{\mathrm{d}x} = \frac{\mathrm{d}(E\epsilon_s\epsilon_0)}{\mathrm{d}x} = \rho(x), \tag{3.25}$$

with the the derivative of D at the i^{th} mesh point equal to

$$\frac{\mathrm{d}D_i}{\mathrm{d}x_i} = \frac{D_j - D_{j-1}}{h_i'} = \frac{E_j\epsilon_j - E_{j-1}\epsilon_{j-1}}{h_i'}. \tag{3.26}$$

This leads to the fully discretised Poisson's equation

$$-\psi_{i+1}\left[\frac{\epsilon_j}{h_j h_i'}\right] + \psi_i\left[\frac{\epsilon_j}{h_j h_i'} + \frac{\epsilon j - 1}{h_{j-1} h_i'}\right] - \psi_{i-1}\left[\frac{\epsilon_{j-1}}{h_{j-1} h_i'}\right] = \frac{q}{\epsilon_0}\rho_i. \tag{3.27}$$

3.2.2 Discretisation of the Continuity Equations

The Scharfetter-Gummel Slotboom variable discretisation method is used and is similar to that proposed by Lin[20]. The current densities at the i^{th} mesh point for both holes and electrons are discretised assuming a constant field between adjacent mesh points. This method resolves well the rapid variations in carrier densities and also yields a diagonally dominant coefficient matrix.

Converting the quasi-Fermi potentials, ϕ_n and ϕ_p in equations (3.11) and (3.12) to Slotboom variables gives

$$J_n = -\frac{\mu_n}{\beta}\frac{n}{u}\frac{\mathrm{d}u}{\mathrm{d}x} = C_n \exp[\beta\psi]\frac{\mathrm{d}u}{\mathrm{d}x} \tag{3.28}$$

$$u = \exp[-\beta\phi_n] \tag{3.29}$$

$$C_n = \frac{\mu_n N_C}{\beta}, \tag{3.30}$$

and

$$J_p = -\frac{\mu_p}{\beta}\frac{p}{v}\frac{\mathrm{d}v}{\mathrm{d}x} = C_p \exp[-\beta\psi]\frac{\mathrm{d}v}{\mathrm{d}x} \tag{3.31}$$

$$v = \exp[\beta\phi_p] \tag{3.32}$$

$$C_p = \frac{\mu_p N_V}{\beta}, \tag{3.33}$$

where u and v are the Slotboom variables for electrons and holes respectively, $\beta = \frac{q}{K_B T}$. Using the chain rule, on the above current equations (3.28) and (3.31), on the i^{th} mesh point and coupling them with the current continuity equations (3.13) and (3.14) gives for electrons

$$\begin{aligned}\frac{\mathrm{d}J_n^i}{\mathrm{d}x} &= \frac{J_n^j - J_n^{j-1}}{h_i'} = -qR_i \\ &= \frac{C_n^i}{h_j h_n'} B(-\beta(\psi_{i+1} - \psi_i)) \exp(\beta\psi_i)(u_{i+1} - u_i) \\ &- \frac{C_n^i}{h_{j-1} h_i'} B(-\beta(\psi_i - \psi_{i-1})) \exp(\beta\psi_{i-1})(u_i - u_{i-1}) = -q(R_i),\end{aligned} \tag{3.34}$$

and for holes

$$\begin{aligned}\frac{\mathrm{d}J_p^i}{\mathrm{d}x} &= \frac{J_p^j - J_p^{j-1}}{h_i'} = qR_i \\ &= \frac{C_p^i}{h_j h_i'} B(\beta(\psi_{i+1} - \psi_i)) \exp(-\beta\psi_i)(v_{i+1} - v_i) \\ &- \frac{C_p^i}{h_{j-1} h_i'} B(\beta(\psi_i - \psi_{i-1})) \exp(-\beta\psi_{i-1})(v_i - v_{i-1}) = qR_i, \quad (3.35)\end{aligned}$$

where the Bernoulli functions B, C_n^i, C_p^i are given below:

$$\begin{aligned}B(y) &= \frac{y}{exp\,(y) - 1} \\ C_n^i &= \frac{\mu_n^i N_c^i}{\beta} \\ C_p^i &= \frac{\mu_p^i N_v^i}{\beta}. \quad (3.36)\end{aligned}$$

3.2.3 Boundary Conditions

For a particular solution to the drift diffusion equations more information, in the form of boundary conditions, has to be provided. The boundary conditions represent the physics of the simulated contacts and can be broken down into two specific types:

(i) **Dirichlet boundary conditions**, where $u = f(u, g)$, relates the unknown variable u in terms of u and some given boundary parameter, g[21].

Boundary conditions such as these can be used to simulate ohmic contacts. Ohmic contacts can be formed by heavily doping a semiconductor n^+ or p^+. A more practical ohmic contact is formed by bringing a metal into contact with a semiconductor where the work function of the metal (ϕ_m) is less than the semiconductor work function (ionisation potential) (ϕ_s) for an n-type semiconductor material. Alternatively $\phi_m > \phi_s$ will form an ohmic contact for p-type semiconductor ma-

terial. In either case a contact will be formed that is in thermal equilibrium and that is charge neutral. Therefore, the mass action law can be used to determine the carrier densities, where $\phi_n = \phi_p$ at the boundary. This is given below for Boltzmann statistics

$$np = n_i^2 = N_c N_v \exp\left(-\beta \frac{E_g}{q}\right). \tag{3.37}$$

If we assume that the dopants in the contact region are totally ionised then the boundary conditions for the electron and hole densities can be expressed as:

$$\begin{array}{lll} & \underline{\text{n}-\text{type}} & \underline{\text{p}-\text{type}} \\ n_{\max} = N_D & , & p_{\max} = N_A \\ p_{\min} = \dfrac{n_i^2}{N_D} & , & n_{\min} = \dfrac{n_i^2}{N_A}, \end{array} \tag{3.38}$$

where the subscripts max and min denote the majority and minority carrier boundary conditions respectively. The potential boundary conditions can be derived from the Boltzmann statistics for the electron and hole densities, see equations (3.19) and (3.20). Rearranging these two equations for potential gives:

$$\begin{array}{ll} \underline{\text{n}-\text{type}} & \underline{\text{p}-\text{type}} \\ \psi = \dfrac{1}{\beta}\log_e\left(\dfrac{n}{N_c}\right) + \phi_n - \dfrac{\chi_c}{q} & , \quad \psi = \dfrac{1}{\beta}\log_e\left(\dfrac{N_v}{p}\right) + \phi_p - \dfrac{\chi_c}{q} - \dfrac{E_g}{q}. \end{array} \tag{3.39}$$

where the applied potential can be introduced through the quasi-Fermi potentials, for example $\phi_n = \phi_p = V_{app}$ at the left hand contact and $\phi_n = \phi_p = 0$ at the right hand contact. The ohmic boundary conditions are listed in table 3.1 for a pn junction diode, where the bias is applied at the left hand side contact, with the right hand side contact pinned at zero volts.

	Left hand ohmic contact	Right hand ohmic contact
n	$n_{\min} = n_i^2/N_A$	$n_{\max} = N_d$
p	$p_{\max} = N_A$	$p_{\min} = n_i^2/N_A$
u	$u = \exp(-\beta V_{app})$	$u = 1.0$
v	$v = \exp(\beta V_{app})$	$v = 1.0$
$q\psi$	$q\psi = \frac{q}{\beta}\log_e\left(\frac{N_v}{p_{\max}}\right) + qV_{app} - \chi_c - E_g$	$q\psi = \frac{q}{\beta}\log_e\left(\frac{n_{\max}}{N_c}\right) - \chi_c$

Table 3.1: Sample boundary conditions for a pn junction diode with the bias applied on the left hand side.

(ii) **Neumann boundary** conditions can be defined in terms of the normal flux, $\mathcal{F}$ through the boundary surface, $\mathcal{F} = f(u, g)$ or $\mathcal{F} = 0$, where u is the unknown and g a boundary parameter[21].

Boundary conditions such as these can be used to simulate Schottky contacts and are formed by bringing a metal into contact with a semiconductor material. However for this case a Schottky contact will be formed on n-type semiconductor material if $\phi_m > \phi_s$ and conversely for p-type semiconductor material $\phi_m < \phi_s$. A considerable amount of literature is available on Schottky diodes (references [10] [22] - [33]). These papers tend to deal with analytical solutions to the drift diffusion equations, for a full numerical approach see references [34] - [36].

Widely used boundary conditions for the electron and hole current densities are shown in equations (3.40) and (3.41) [10] [35]:

$$\begin{aligned} J_{nb} &= qV_{rn}\left(n(x_m) - n_{eq}\right) \quad , \quad V_{rn} = \sqrt{\frac{k_B T}{2\pi m_c^*}} \\ J_{pb} &= -qV_{rp}\left(p(x_m) - p_{eq}\right) \quad , \quad V_{rp} = \sqrt{\frac{k_B T}{2\pi m_v^*}} \end{aligned} \tag{3.40}$$

$$\begin{aligned} n(x) &= N_c \exp\left(-\beta\left(\phi_{Bn} - \phi_n\right)\right) \quad , \quad n_{eq} = N_c \exp\left(-\beta\left(\phi_{Bn}\right)\right) \\ p(x) &= N_v \exp\left(\beta\left(\phi_{Bp} - \phi_p\right)\right) \quad , \quad p_{eq} = N_v \exp\left(-\beta\left(\phi_{Bp}\right)\right). \end{aligned} \tag{3.41}$$

Here V_{rn} and V_{rp} are the electron and hole recombination velocities, $n(x_m)$ and $p(x_m)$ are the electron and hole densities adjacent to the metal contact within the semiconductor and n_{eq} and p_{eq} are the equilibrium electron and hole densities at x_m that would occur if it were possible to reach equilibrium without altering the position or magnitude of the potential energy maximum. The barriers to electron and hole injection at the Schottky contact are ϕ_{Bn} and ϕ_{Bp} respectively. These can be estimated from

$$q\phi_{Bn} = q\phi_m - \chi_c \tag{3.42}$$

$$q\phi_{Bp} = E_g - q\phi_{Bn}. \tag{3.43}$$

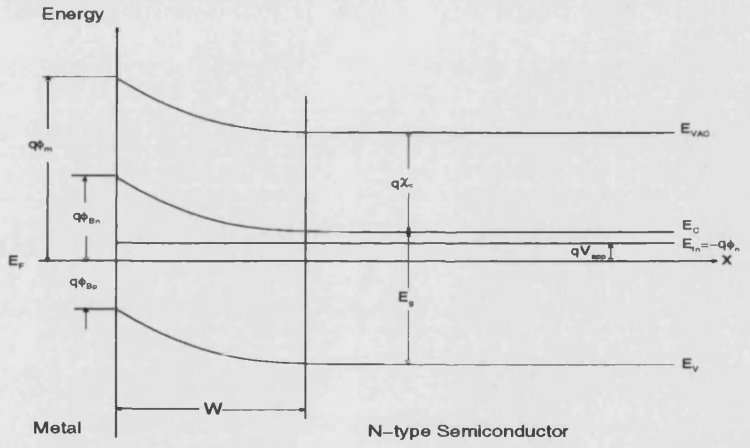

Figure 3.2: Band diagram for a unipolar Schottky interface (RHS is assumed ohmic in nature).

Figure 3.2 shows a representation of a metal n-type semiconductor interface. The conduction band E_C decreases from the Schottky contact towards the bulk semiconductor thus forming a barrier to the electron flow from the metal to the semiconductor ($J^e_{m\to s}$) and from the the semiconductor to the metal ($J^e_{s\to m}$). $J^e_{s\to m}$ is strongly dependent upon the applied potential, whereas $J^e_{m\to s}$ is independent of the applied potential if barrier height lowering effects are ignored. The valence band E_V follows the same trend as the conduction band but is offset by the energy gap of the semiconductor. A similar condition exists for the hole current density contributions $J^h_{m\to s}$ and $J^h_{s\to m}$. Therefore, with respect to thermionic emission, a symmetric situation exists for electron and hole injection that is

strongly dependent upon the barriers to injection ϕ_{Bn} and ϕ_{Bp}.

The boundary conditions on the u and v state variables can be derived by discretising the current density equations (3.40) and (3.41). Using conservation of current through the device these discretised equations can then be equated with their respective boundary condition. For example, the electron current density can be given by

$$J_{nb} = qV_{rn}N_c \exp\left(-\beta\phi_{Bn}\right)\left(u_{i-1} - 1\right) = k_B T N_c \exp\left(-\beta\phi_{Bn}\right)\left(\frac{u_i - u_{i-1}}{h}\right), \tag{3.44}$$

where the potential boundary condition is given by ϕ_{Bn}. Rearranging for the Slotboom variable u_{i-1} gives

$$u_{i-1} = \left(\frac{1 + \frac{\mu_n}{\beta V_{rn} h} u_i}{1 + \frac{\mu_n}{\beta V_{rn} h}}\right). \tag{3.45}$$

Using the same method the relationship for the hole Slotboom equation can be derived, to give

$$v_{i-1} = \left(\frac{1 - \frac{\mu_p}{\beta V_{rp} h} v_i}{1 - \frac{\mu_p}{\beta V_{rp} h}}\right). \tag{3.46}$$

Equation (3.45), and the v Slotboom equivalent for holes allow the boundary conditions for u, v, n and p at the left hand contact to float dependent upon their interior mesh points. The boundary conditions are shown in table (3.2), for a metal-contact/semiconductor/ohmic-contact structure, where the bias is applied on the right hand side ohmic contact.

n-type	Left hand Schottky contact	Right hand ohmic contact
$q\psi$	$q\psi = -q\phi_{Bn}$	$q\psi = \frac{q}{\beta}\log_e\left(\frac{n_{\max}}{N_C}\right) + qV_{app} - \chi_c$
u	$u_{i-1} = \left(1 + \frac{\mu_n}{\beta V_{rnh}} u_i\right) / \left(1 + \frac{\mu_n}{\beta V_{rnh}}\right)$	$u = \exp\left(\beta V_{app}\right)$
n	$n(x_m) = N_C \exp\left(-\beta\left(\phi_{Bn} + \phi_n\right)\right)$	$n_{\max} = N_D$
p-type	Left hand Schottky contact	Right hand ohmic contact
$q\psi$	$q\psi = -q\phi_{Bp}$	$q\psi = \frac{q}{\beta}\log_e\left(\frac{N_V}{p_{\max}}\right) + qV_{app} - \chi_c - E_g$
v	$v_{i-1} = \left(1 - \frac{\mu_p}{\beta V_{rph}} v_i\right) / \left(1 - \frac{\mu_p}{\beta V_{rph}}\right)$	$v = \exp\left(\beta V_{app}\right)$
p	$p(x_m) = N_V \exp\left(\beta\left(\phi_p - \phi_{Bp}\right)\right)$	$p_{\max} = N_A$

Table 3.2: Sample boundary conditions for a Schottky diode, bias applied on the right hand side.

3.3 Methods of Solution

There are 3 discretised 2nd order partial differential equations to be solved: Poisson's equation 3.27, the electron continuity equation (3.34) and the hole continuity equation (3.35). These 3 discretised equations can be represented in matrix form as:

$$\mathbf{A} \cdot \psi = \mathbf{r} \text{ (For Poisson's equation.)} \tag{3.47}$$

$$\mathbf{A} \cdot \mathbf{u} = \mathbf{r} \text{ (For the electron continuity equation.)} \tag{3.48}$$

$$\mathbf{A} \cdot \mathbf{v} = \mathbf{r} \text{ (For the hole continuity equation.),} \tag{3.49}$$

where state variables ψ, $\mathbf{u}$, and $\mathbf{v}$ have been factored out of the original equations and $\mathbf{A}$ is a square matrix with dimensions equal to the number of internal mesh points. Taking equation (3.49) as an example, we can represent this as

$$a_i v_{i-1} + b_i v_i + c_i v_{i+1} = r_i, \tag{3.50}$$

This leads to the matrix form shown below.

$$\begin{pmatrix} b_1 & c_1 & 0 & 0 & 0 & 0 & 0 & 0 \\ a_2 & b_2 & c_2 & 0 & 0 & 0 & 0 & 0 \\ 0 & a_3 & b_3 & c_3 & 0 & 0 & 0 & 0 \\ 0 & 0 & \cdot & \cdot & \cdot & 0 & 0 & 0 \\ 0 & 0 & 0 & \cdot & \cdot & \cdot & 0 & 0 \\ 0 & 0 & 0 & 0 & a_{N-2} & b_{N-2} & c_{N-2} & 0 \\ 0 & 0 & 0 & 0 & 0 & a_{N-1} & b_{N-1} & c_{N-1} \\ 0 & 0 & 0 & 0 & 0 & 0 & a_N & b_N \end{pmatrix} \begin{pmatrix} v_1 \\ v_2 \\ v_3 \\ \cdot \\ \cdot \\ v_{N-2} \\ v_{N-1} \\ v_N \end{pmatrix} = \begin{pmatrix} r_1 - a_1 \\ r_2 \\ r_3 \\ \cdot \\ \cdot \\ r_{N-2} \\ r_{N-1} \\ r_N - c_N \end{pmatrix} \tag{3.51}$$

The coefficients a_1 and c_N are the boundary conditions, previously discussed in section 3.2.3, for the state variable v.

A method of solving matrix equations of this form is shown in figure 3.3 and is called the Gummel block iteration method[37]. This method allows the equations for ψ, u and v to be decoupled and solved separately. Referring to the Gummel flow chart the solution is formed in the following iterative manner:

1. Initial guesses for the 3 state variables are calculated. We used a linear rising form for all 3 state variables;

2. For the k^{th} Gummel loop a new solution to a predefined accuracy is formed for ψ_k using n_{k-1} and p_{k-1}, where ψ_k forms the guess for the next Gummel iteration $k+1$;

3. The electron Slotboom variable u_k is then solved to a predetermined accuracy and the electron density updated. Again the u_k solution forms the guess for the next Gummel iteration $k+1$;

4. Finally the hole Slotboom variable v is solved to a predetermined accuracy and the hole density updated. The new solution forms the guess for the next Gummel iteration $k+1$;

5. After performing steps (2)-(4) we test the error between the new solutions (k) and the old solutions $(k-1)$, if the error is less than a user defined tolerance then a converged solution has been formed otherwise steps (2)-(4) are repeated. This process is repeated until a solution is found or the

number of Gummel loops exceeds a user defined maximum, in which case the system has failed to converged.

Two possible methods of solving the above equations using the Gummel flow chart will now be shown. These are the Successive Over Relaxation (SOR) method and the Direct matrix (Direct) approach.

3.3.1 Successive Over Relaxation (SOR) Method

Using the previous equation (3.50) ($\mathbf{A} \cdot \mathbf{v} = \mathbf{r}$) as an example, we can form a new solution at the i^{th} mesh point in terms of the old solution plus a correction. Therefore,

$$v_i^{new} = v_i^{old} - \omega \frac{\epsilon_i}{\epsilon_i'} \tag{3.52}$$

$$\epsilon_i = a_i v_{i-1} + b_i v_i + c_i v_{i-1} - r_i \tag{3.53}$$

$$\epsilon_i' = \frac{\mathrm{d}}{\mathrm{d}x}(v_i - r_i), \tag{3.54}$$

where ϵ_i is found from rearranging equation (3.50) and ϵ_i' is the derivative with respect to the state variable at the i^{th} mesh point. The relaxation variable ω has a value between 1 and 2 and can be optimised using the following equation [39]

$$\omega = \frac{1}{2 + \sqrt{1 - \rho^2}}, \tag{3.55}$$

where the spectral radius $\rho = \cos\left(\frac{\pi}{N-1}\right)$.

There are several advantages to using the SOR method: (i) stability of solution; (ii) limited memory requirements; (iii) easily generalised to more complex discretisation techniques.

The relative error used to determine convergence within a Gummel iteration is

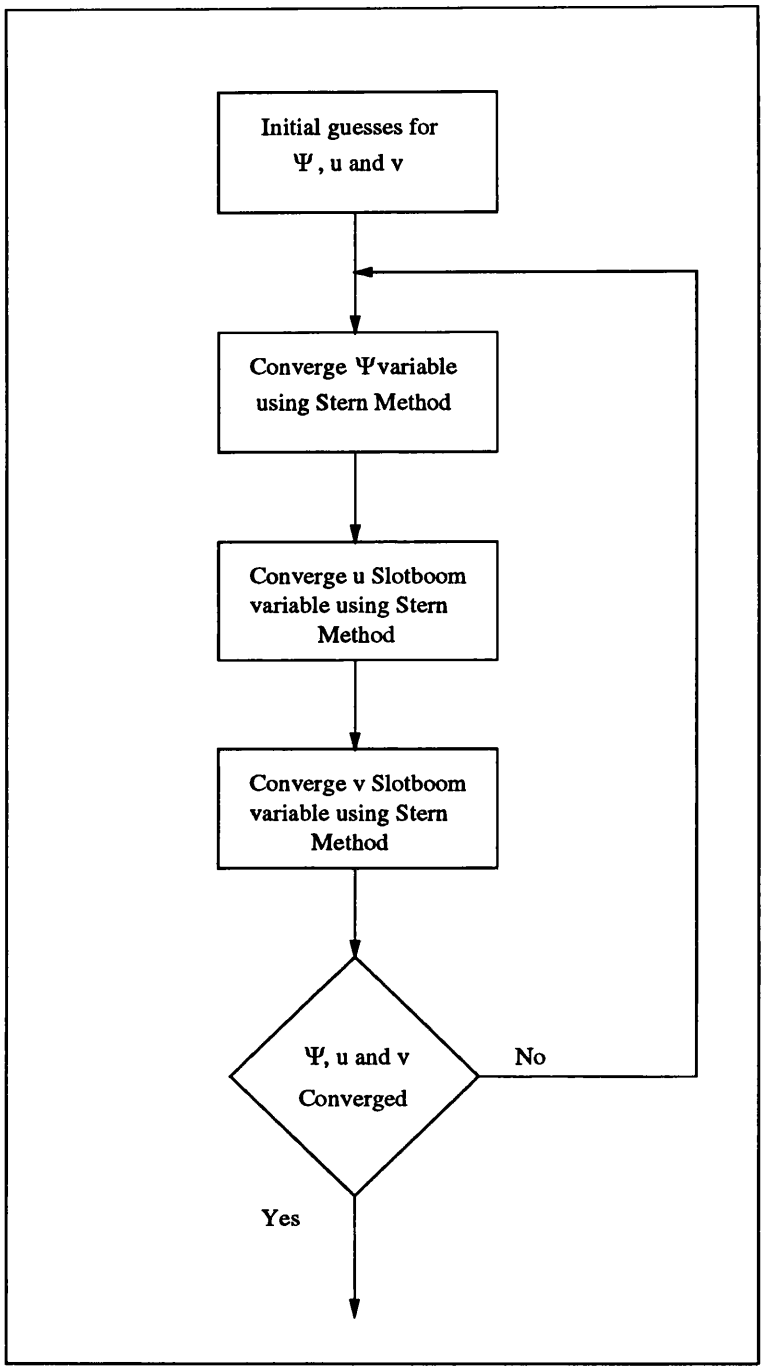

Figure 3.3: Flow chart for simplified Gummel convergence loop using Stern's convergence method[38].

defined as

$$\sigma = \frac{\sum_{i=1}^{N-1} \Delta_i}{\max(A_i)} \tag{3.56}$$

$$\Delta_i = \frac{\epsilon_i}{\epsilon_i'}, \tag{3.57}$$

where A_i is the maximum value of the state variable within the device. When σ for all 3 state variables has a value less than a predefined user tolerance then convergence has been achieved.

3.3.2 Direct Method

The Direct method involves solving the 3 matrices (3.47) - (3.49) in one operation rather than the iterative method of SOR. As the three matrices are tridiagonal LU decomposition can be used to form a memory efficient and fast solution to these equations. The method used can be found in Numerical Recipes [40] and consists of the 2 subroutines banddec and banbks.

The method of solution consists of forming a new solution by solving the matrix equations. A fraction of the current solution is then mixed into the old solution which forms the new solution. The magnitude of the mixing fraction is important as this will dictate the stability and the speed of convergence. Stern's method[41] is used to optimise the speed of convergence versus stability, see equations below

$$v_{k+1}^i = v_{k-1}^i + \lambda_k^i \omega_k^i \tag{3.58}$$

$$\omega_k^i = v_k^i - v_{k-1}^i \tag{3.59}$$

$$\lambda_k^i = \frac{\lambda_{k-1}^i}{1 - \Omega_k^i / \Omega_{k-1}^i} \tag{3.60}$$

$$\Omega_k^i = \text{sign}\left(\max|\omega_k^i|\right) \ , \ \Omega_{k-1}^i = \text{sign}\left(\max|\omega_{k-1}^i|\right), \tag{3.61}$$

where the indices k and i represent the Gummel loop and the mesh point respectively. The convergence fraction λ_k consists of a fraction from the previous solution λ_{k-1} and the maximum signed value of ω over all mesh points during the k and $k-1$ Gummel loops which can be positive or negative.

The relative error used to determine convergence within a Gummel iteration is defined as

$$\sigma = \frac{\sum_{i=1}^{N-1} \Delta_i}{\max(A_i)} \tag{3.62}$$

$$\Delta_i = \omega_k^i, \tag{3.63}$$

where A_i is the maximum value of the state variable within the device. When σ for all 3 state variables has a value less than a predefined user tolerance then convergence has been achieved.

3.4 Results

This section presents results for the numerical drift diffusion model, discussed previously in this chapter, and compares them with independent numerical methods and analytical solutions where possible. The material parameters for GaAs and Si semiconductor materials are presented in table 3.3[10] below.

3.4.1 Ohmic Device

The bipolar (ohmic contact) numerical drift diffusion solver can cope with a variety of ohmic device structures, such as: purely n-type or p-type; nip or pin; np junction diodes and nin devices. It is impractical to present results for all these structures, however the np/pn junction diode with ohmic contacts has been well covered in [17]-[21] and accurate numerical solutions for this structure are available to validate the code. Figure 3.4 shows the geometry of the simulated

Drift Diffusion Variables	GaAs Material	Si Material	Units
T	300	300	K
ϵ	13.1	11.8	-
N_c	4.7x10^{23}	2.8x10^{25}	m^{-3}
N_v	7.0x10^{24}	1.04x10^{25}	m^{-3}
μ_n	0.85	0.15	m^2/(Vs)
μ_p	0.04	0.045	m^2/(Vs)
E_g	1.424	1.12	eV
χ_c	4.07	4.01	eV
m_e^*	0.067	0.33	-
m_h^*	0.47	0.55	-

Table 3.3: Material parameters for GaAs and Si device simulations.

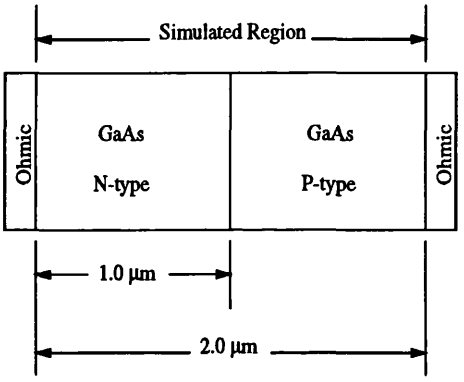

Figure 3.4: Geometry of pn junction diode.

device and tables 3.3 and 3.4 list the material parameters used for the simulation.

Figures 3.5a and 3.5b show numerical solutions to the band structure and quasi-Fermi levels for $V_{app} = 0V$ and $V_{app} = 0.5V$. For zero bias the band profiles for a pn diode are clearly distinguishable, with the quasi-Fermi levels flat and equal through the entire device, as expected. Under forward bias the quasi-Fermi levels separate in the depletion region by the magnitude of the applied bias $V_{app} = 0.5V$. Additionally the built in potential $V_{bi} = |\psi_{lhs} - \psi_{rhs}|$ reduces by the applied bias magnitude and the device conducts. Figures 3.6a and 3.6b show the electron and hole densities through the device structure for the previously mentioned biases. It can be seen that the carrier densities in the centre of the depletion region increase substantially (approximately 3 orders of magnitude) with forward bias, as expected.

Material Parameter	Value	Units
N_a	$1x10^{22}$	m^{-3}
N_d	$1x10^{22}$	m^{-3}
τ_n	$1x10^{-9}$	s
τ_p	$1x10^{-9}$	s

Table 3.4: Device parameters for figure 3.4.

Figure 3.7a shows current density-voltage (JV) curves for device (a). The code (Direct Method) was tested against two independent methods, Wilson et al (SOR Method)[42], and an analytical solution, see Sze section 2.4[10]. It can be seen that the 2 drift diffusion methods, Direct and SOR, are in agreement over the entire applied voltage range. Figure 3.7b shows the JV curves as per figure 3.7a but differs in that both numerical methods have SRH recombination, equation (3.15), turned on. This results in the classic dual gradient JV characteristic, see Sze section 2.42[10], which demonstrates that SRH recombination dominates for applied biases in the range ($0V < V_{app} < 0.7V$). Again it can be seen that the 2 drift diffusions methods are in agreement over the entire applied voltage range.

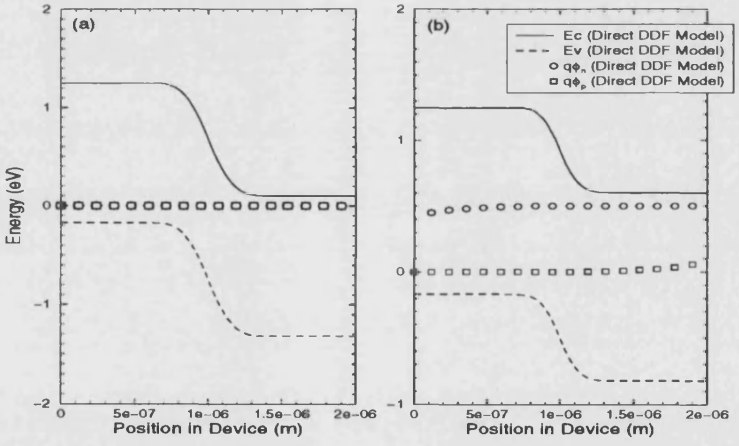

Figure 3.5: Conduction band (solid), valence band (dash), electron quasi-Fermi level (○) and hole quasi-Fermi level (□) for a bipolar GaAs pn junction diode. Panel (a) shows the band profiles within the pn diode for $V_{app} = 0.0V$. Panel (b) shows the band profiles for $V_{app} = 0.5V$.

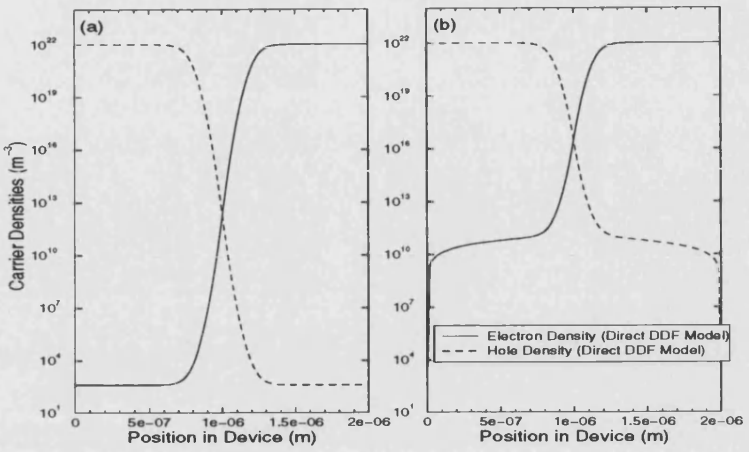

Figure 3.6: Electron density (solid) and hole density for a bipolar GaAs pn junction diode. Panel (a) shows the carrier densities within the pn diode for $V_{app} = 0.0V$. Panel (b) shows the carrier densities for $V_{app} = 0.5V$.

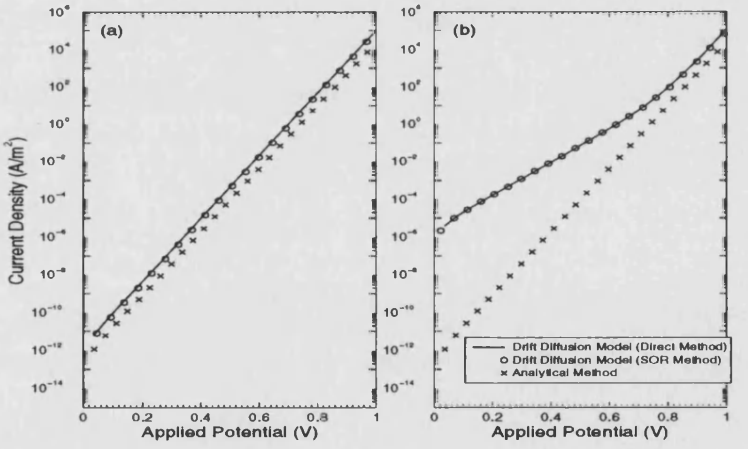

Figure 3.7: Comparison of current density curves for numerical solutions to the drift diffusion equations (Direct method (solid) and SOR (o)) and an analytical method (x); for a bipolar GaAs pn junction diode. Panels (a) and (b) show the current density curves for no SRH recombination and panel and with SRH recombination respectively.

3.4.2 Schottky Devices

The unipolar Schottky contact drift diffusion model, like the ohmic contact variant, can handle a variety of device structures. For brevity only a small selection of results that have an independent means of corroboration have been included. The devices studied are shown in figures 3.8a - 3.8d, with the material parameters used in the model shown in tables 3.3 and 3.5.

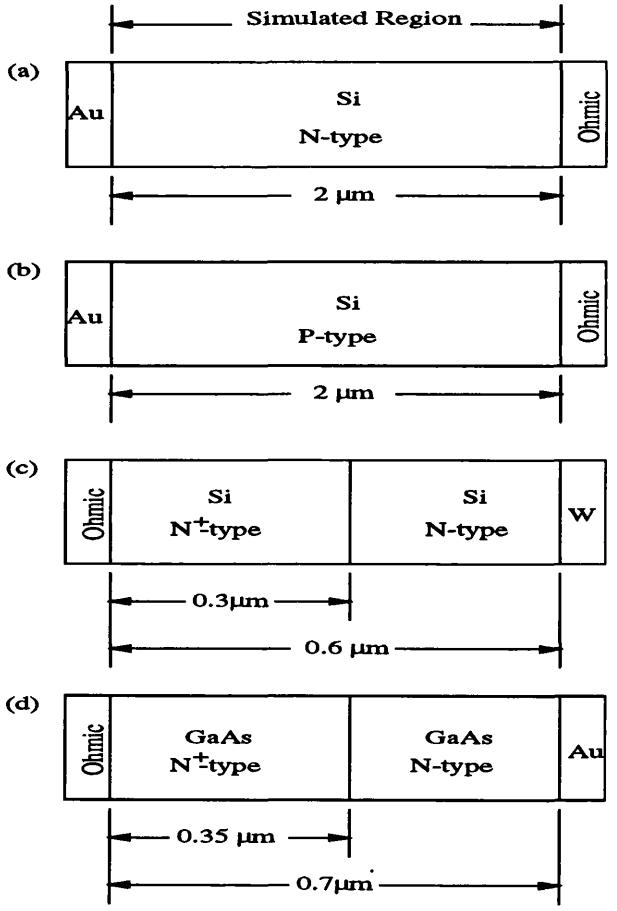

Figure 3.8: Schottky device structures.

Figures 3.9a and 3.9b show the band profiles and quasi-Fermi levels for the device depicted in 3.8a. The effect of the metal contact on the semiconductor can be seen in the bending of the conduction and valence bands, with the built in potential being $V_{bi} = |\psi_{Bn} - \psi_{rhs}| = 0.48V$. These results show agreement between the drift diffusion model and the analytical model of Crowell[31] for both forward bias and reverse bias. Figure 3.10a and 3.10b again compare the numerical model with the analytical model of Crowell, but for a p doped Si device, see geometry (b) in

DDF Variables	Au-Si Device (a)	Au-Si Device (b)	Si-W Device (c)	GaAs-Au Device (d)	Units
N_a	N/A	$1x10^{22}$	N/A	N/A	m^-3
N_d	$1x10^{22}$	N/A	$N_d = 1x10^{22}$ $N_d^+ = 1x10^{23}$	$N_d = 1x10^{22}$ $N_d^+ = 1x10^{23}$	m^-3
$q\phi_{Bn}$	0.79	0.49	0.67	0.73	eV

Table 3.5: Schottky device parameters.

figure 3.8.

The JV curves for device (a) are compared in figure 3.11. The 3 methods shown are: the drift diffusion model; analytical method 1 of Crowell[31] and analytical method 2 of Sze[10]. The results for all 3 solution are in agreement for almost the entire applied bias range. The deviation of analytical method 1 from the numerical solution for $V_{app} > 0.45V$ is due to the applied bias approaching the built in potential. Both analytical models are only valid up to the built in potential, whereas the drift diffusion solver can form a solution. This is important for OLEDs as light emission occurs at applied biases above the built in potential.

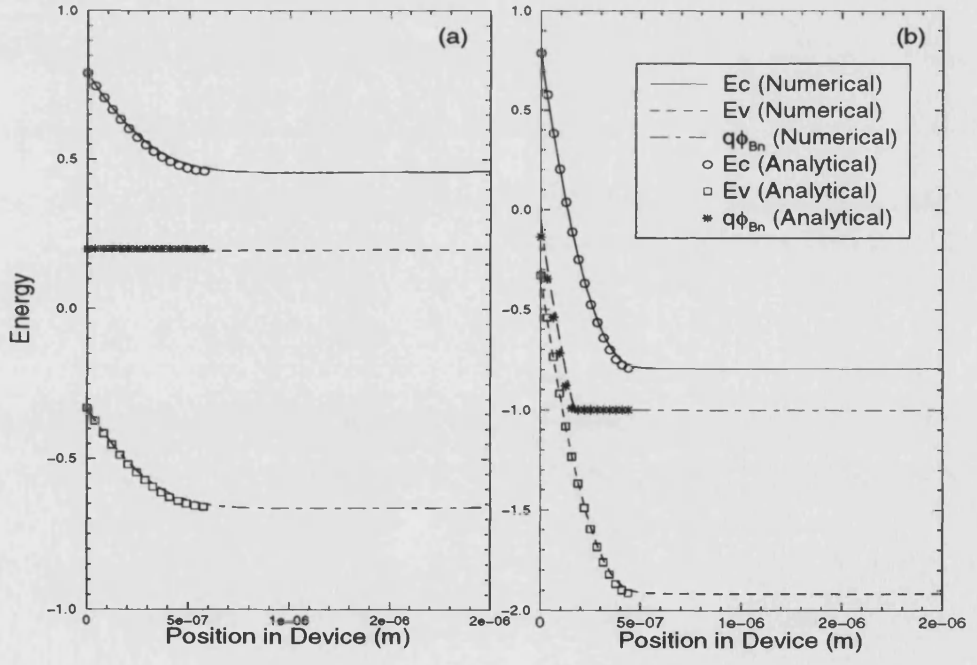

Figure 3.9: Comparison of band profiles and quasi-Fermi levels for numerical and analytical solutions to a unipolar (n-type) Au-Si Schottky diode. Panels (a) and (b) show the band profiles for $V_{app} = 0.2V$ forward bias and $V_{app} = -1.0V$ reverse bias respectively.

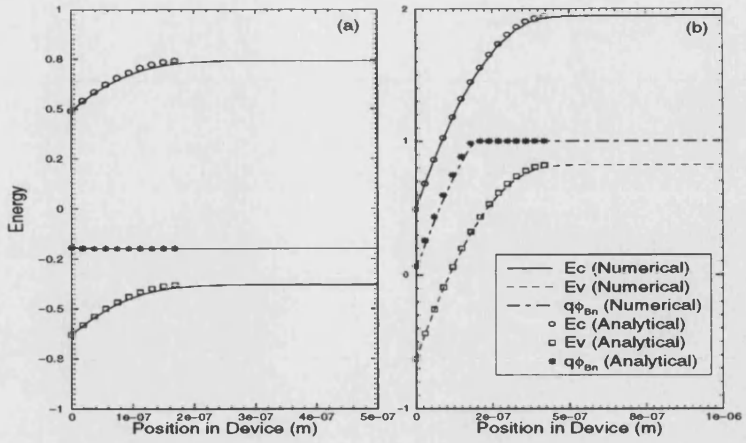

Figure 3.10: Comparison of band profiles and quasi-Fermi levels for numerical and analytical solutions to a unipolar (p-type) Au-Si Schottky diode. Panels (a) and (b) show the band profiles for $V_{app} = 0.2V$ forward bias and $V_{app} = -1.0V$ reverse bias respectively.

Figures 3.12 and 3.13 compare the drift diffusion model with results from a Electron Monte Carlo (EMC) model, see Ravaioli [43] . Both structures consist of an LHS ohmic contact, a heavily n-type doped contact layer, a n-type layer and a RHS Schottky metal contact. Figure 3.12a and 3.12b show the conduction bands for zero bias and $V_{app} = 0.44V$ forward biased respectively. The results are in good agreement for zero bias but differ under forward bias close to the Schottky contact ($x > 4\mu m$). This difference may be due to the E.M.C. model including the effect of tunnelling through the potential barrier at the RHS Schottky contact.

The zero bias results for the GaAs material, structure (d) are also presented. Figures 3.13a and 3.13b compare the conduction bands and electron densities for the drift diffusion model and the E.M.C. model previously mentioned. It can be seen that these 2 independent methods are again in good agreement.

3.5 Conclusions

The unipolar Schottky contact drift diffusion model (DDM) and the bipolar ohmic contact DDM have been shown to be in good agreement with independent numerical and analytical solutions. Although the bipolar ohmic code is stable it is not appropriate for OLEDs, as the injecting contacts on the organic devices are

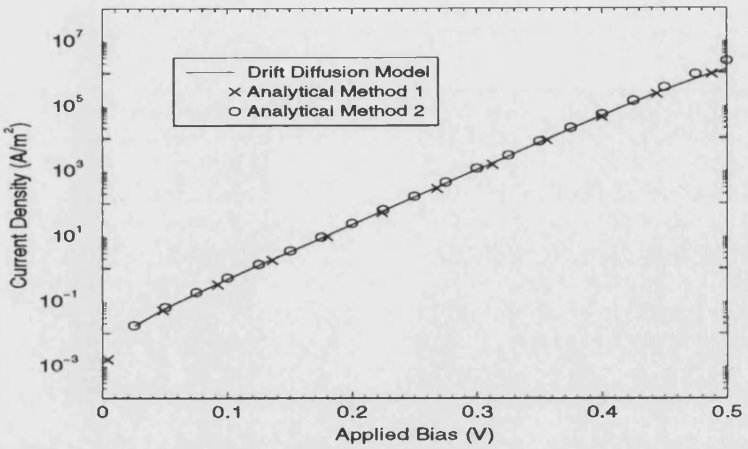

Figure 3.11: Comparison of current density curves for numerical and analytical solutions to a unipolar (n-type) Au-Si Schottky diode.

suspected to be Schottky in nature [9].

The unipolar Schottky DDM, whilst being stable for the devices shown, had several serious flaws. The convergence rate for both devices (a) and (b) is slow, typically > 50000 iteration for each voltage step, which results in simulation times in excess of 30 minutes for moderate applied bias ranges. Additionally solution for $V_{app} > V_{bi}$ were unstable and convergence was more difficult to achieve. This has important implications for simulating OLEDs as the bias range of interest is typically several volts in excess of the built in potential.

Several attempts to convert the unipolar Schottky model to a fully bipolar version were tried, but these proved unstable. The instability in the model appeared to be the bipolar Schottky boundary conditions. Upon further investigation it was found that the quasi-Fermi levels oscillated. Convergence tolerances of $\sigma = 1\text{x}10^{-2}$ were achieved but this was far from satisfactory. It was clear that a more stable method was required for simulating Schottky device structures.

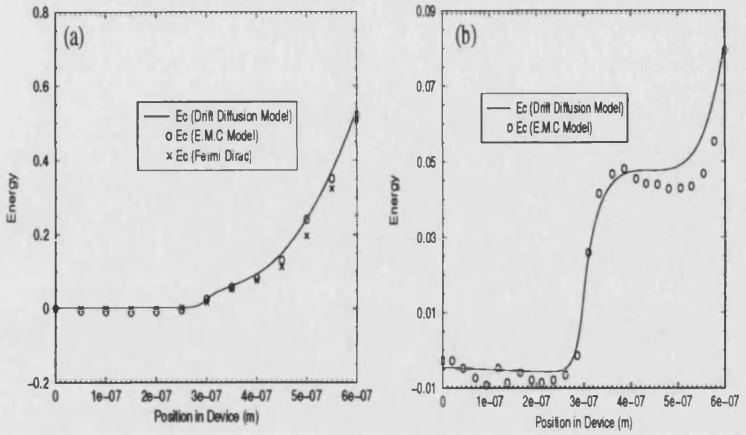

Figure 3.12: Comparison of two numerical solutions to a n-type Si-W Schottky diode; Drift Diffusion model (solid) and EMC model (o). Panels (a) and (b) show the conduction band profiles for $V_{app} = 0V$ and $V_{app} = 0.44V$ respectively.

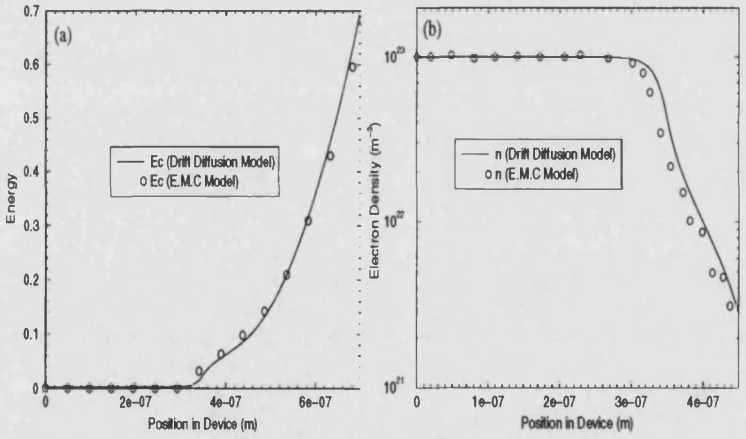

Figure 3.13: Comparison of two numerical solutions to a n-type GaAs-Au Schottky diode; Drift Diffusion model (solid) and E.M.C model (o). Panels (a) and (b) show the conduction band profiles and electron carrier densities, for $V_{app} = 0V$, respectively.

References

[1] P. S. Davids, S. M. Kogan, I. D. Parker and D. L. Smith, *Applied Physics Letters*, **69**, 2270-2272, 1996.

[2] I. H. Campbell, P. S. Davids and D. L. Smith, *Applied Physics Letters*, **72**, 1863-1865, 1998.

[3] U. Wolf, V. I. Arkhipov and H. Bässler, *Physical Review B*, **59**, 7507-7513, 1998.

[4] M. M. D. Ramos, A. M. Stoneham and A. P. Sutton, *Synthetic Metal*, **67**, 137-140, 1994.

[5] M. A. Lampert and P. Marks, *Current injection in Solids*, Academic Press, New York and London, (1970).

[6] P. W. M. Blom, M. J. M. de Jong and M. G. van Munster, *Physical Review B*, **55**, R656-R659, 1997.

[7] J. M. Lupton and I. D. S. Samuel, *J. Phys. D: Applied Physics*, **32**, 2973-2984, 1999.

[8] A. M. Stoneham, *Private Communication*, 1999.

[9] I. D. Parker, *Journal of Applied Physics*, **75**, 1656-1666, 1993.

[10] S. Sze, *Physics of Semiconductors*, John Wiley and Sons, New York (1981).

[11] K. F. Brennan, *The Physics of Semiconductors with Application to Optoelectronic Devices*, Cambridge University Press, Cambridge (1999).

[12] S. Tiwari, *Compound Semiconductor Device Physics*, Academic Press, London (1992).

[13] J. C. Scott, L.T. Pautmeier and L.B. Schein, *Physical Review B*, **46**, 8603-8606, 1992.

[14] M. Abkowitz and D. M. Pai, *Philosophical Magazine B*, **53**, 217-231, 1985.

[15] K. Mamoru, *Numerical Analysis for Semiconductor Devices*, D.C. Heath and Company, Toronto (1982).

[16] W. Shockley and W. T. Read, *Physical Review*, **87**, 835-841, 1952.

[17] C. Snowden, *Semiconductor Device Physics*, Springer-Verlag, London (1989).

[18] W. H. Press, B P Flannery, S. A. Teulolsky and W. T. Vertterling, *Numerical Recipes in Fortran*, Cambridge University Press, Cambridge (1989).

[19] S. J. Woods, *Ph.D. Thesis*, University of East Anglia School of Physics, (1998).

[20] Q. Lin, N. Goldsman and G. Tai, *Solid State Electronics*, **37**, 359-371, 1994.

[21] P.A. Markowich, *The Stationary Semiconductor Device Equations*, Springer-Verlag, London (1986).

[22] D. Schroeder, *Modelling of Carrier Transport for Device Simulation*, Springer-Verlag, New York (1994).

[23] M. S. Tyagi, *Introduction to Semiconductor Materials and Devices*, John Wiley and Sons, New York (1991).

[24] -DDF E. H. Rhoderick, *Metal-Semiconductor Contacts*, Oxford University Press, Oxford (1978).

[25] J. R. MacDonald, *Solid State Electronics*, **5**, 11-37, 1962.

[26] C. R. Crowell, *Solid State Electronics*, **8**, 395-399, 1965.

[27] C. R. Crowell and S. M. Sze, *Solid State Electronics*, **9**, 1035-1048, 1966.

[28] C. A. Mead, *Solid Sate Electronics*, **9**, 1023-1033, 1966.

[29] C. Y. Chang and S. M. Sze, *Solid State Electronics*, **13**, 727-740, 1970.

[30] S. M. Sze, D. J. Coleman (JR) and A. Loya, *Solid State Electronics*, **14**, 1209-1218, 1971.

[31] C. R. Crowell and M. Beguwala, *Solid State Electronics*, **14**, 1149-1157, 1971.

[32] S. C. Choo, L. S. Tan and K. B. Quek, *Solid State Electronics*, **35**, 269-283, 1992.

[33] P. V. Mieghem, *IEEE Transactions on Electron Devices*, **41**, 2440-2447, 1994.

[34] D. S. Watanbe and S. Slamet, *IEEE Transactions on Electron Devices*, **30**, 1042-1049, 1983.

[35] S. C. Choo, *Solid State Electronics*, **38**, 2085-2093, 1994.

[36] C. M. Hurd and W. R. Mckinnon, *Journal of Applied Physics*, **75**, 596-603, 1994.

[37] H. K. Gummel, *IEEE Transactions on Electron Devices*, 455-465, 1964.

[38] F. Stern, *Journal of Computer Physics*, **6**, 56-67, 9170.

[39] R. L. Burden and J. D. Faires, *Numerical Analysis Sixth Edition*, Brooks/Cole, London (1997).

[40] W. H. Press, B. P. Flannery, S. A. Teukolsky and W. T. Vetterling, *Numerical Recipes in Fortran*, Cambridge University Press, Cambridge (1989).

[41] S. Stern, *Journal of Computational Physics*, **6**, 56-57, 1970

[42] S. P. Wilson and A. B. Walker, *Drift Diffusion Code Developed at the UEA*, 1995.

[43] U. Ravaioli, O. Lugli and M.A. Osman, *IEEE Transactions on Electron Devices*, **32**, 2097-2101, 1985..

[44] C. R. Crowell and V.L. Rideout, *Solid State Electronics*, **12**, 89-105, 1969.

Chapter 4

First Order Newton Method (SOLVDE)

In chapter 3 the derivation and solution of the drift diffusion equations were investigated. Two second order approaches to solving these equations were implemented, the SOR method and the Direct method. Both approaches were shown to work for a variety of device structures and contact types. However, they could not be generalised to form a stable solution for bipolar Schottky contact devices. A bipolar model is essential in order to simulate recombination, carrier transport and injection mechanisms of OLEDs. Therefore a more stable and flexible method of solving the drift diffusion equations had to be found. An alternative to the SOR and Direct methods, is the first order Newton approach of SOLVDE. This method had been successfully used in our device modelling group [1] and had the additional advantage of solving the hole and electron current densities directly, thus allowing a direct implementation of the Schottky boundary conditions.

In section 4.1 the first order Newton method and the SOLVDE algorithm will be introduced. In section 4.3 the boundary conditions and the internal variables for an inorganic bipolar device will be described. Sample results for the device structures shown in chapter 3 will be presented and compared against the SOR and Direct Methods. Finally, in section 4.5, the numerical method will be generalised to a fully organic model capable of simulating OLEDs.

4.1 SOLVDE Method

This approach represents the 3 coupled second order drift diffusion equations as 6 coupled first order ordinary differential equations (ODEs) of the following form

$$\frac{\mathrm{d}y}{\mathrm{d}x} = g(x, y), \tag{4.1}$$

which can be discretised about two adjacent mesh points, k and $k-1$, by

$$E_k = y_k - y_{k-1} = (x_k - x_{k-1})g\left(\frac{1}{2}(x_k + x_{k-1}), \frac{1}{2}(y_k + y_{k-1})\right). \tag{4.2}$$

The 6 ODEs are as follows:

$$\begin{aligned}
\frac{\mathrm{d}J_n}{\mathrm{d}x} &= -q\Delta G && (4.3)\\
\frac{\mathrm{d}J_p}{\mathrm{d}x} &= q\Delta G && (4.4)\\
\frac{\mathrm{d}D}{\mathrm{d}x} &= q\left(p - n + N_D^+ - N_A^-\right) && (4.5)\\
D &= -\epsilon_0\epsilon_s\frac{\mathrm{d}\psi}{\mathrm{d}x} && (4.6)\\
J_n &= -q\mu_n n\frac{\mathrm{d}\phi_n}{\mathrm{d}x} && (4.7)\\
J_p &= -q\mu_p p\frac{\mathrm{d}\phi_p}{\mathrm{d}x}, && (4.8)
\end{aligned}$$

where $\Delta G = G(x) - R(x)$. On a mesh of M points we will have MxN variables, where the number of state variables we are solving is $N = 6$. The approach to solving these equations is a multidimensional Newton method which relaxes the state variables to a converged solution using the SOLVDE subroutine in Numerical Recipes[2]. $M-1$ difference equations of the form of equation (4.2) can be formed, where M is the mesh of size $M(k = 2, 3, 4, \cdots, M)$. There are a total of $(M-1)$x6 equations for Mx6 unknowns. The final N equations are determined by the boundary conditions at each contact

$$E_1 = B(x_1, y_1) = 0 \tag{4.9}$$

$$E_{M+1} = C(x_M, y_M) = 0. \tag{4.10}$$

Therefore 6 boundary conditions are required for a particular solution. Defining n_1 and n_2 to be the number of boundary conditions at x_1 and x_M, the left and right hand contacts respectively. The number of boundary conditions at each contact is flexible but for our particular case a symmetric form $n_1 = n_2 = 3$ is chosen. The ordering of the state variables is important and will be discussed at length later.

The order of the boundary conditions in accordance with the SOLVDE documentation is as follows

$$E_{j,1} \neq 0 \quad , \quad j = 4, 5, 6 \tag{4.11}$$

$$E_{j,M+1} \neq 0 \quad , \quad j = 1, 2, 3, \tag{4.12}$$

where j denotes the state variable. The ODEs can be expanded using a two variable Taylor expansion

$$\begin{aligned} E_k(y_k + \Delta y_k, y_{k-1} + \Delta y_{k-1}) &\approx E_k(y_k, y_{k-1}) + \\ \sum_{n=1}^{N} \frac{\partial E_k}{\partial y_{n,k-1}} \Delta y_{n,k-1} &+ \sum_{n=1}^{N} \frac{\partial E_k}{\partial y_{n,k}} \Delta y_{n,k}. \end{aligned} \tag{4.13}$$

For a converged solution $E_k(y_k + \Delta y_k, y_{k-1}) = 0$, it is therefore possible to rearrange the above equation to form the following derivatives (S_j's) for the internal points

$$\sum_{n=1}^{N} S_{j,n} \Delta y_{n,k-1} + \sum_{n=N+1}^{2N} S_{j,n} \Delta y_{n-N,k} = -E_{j,k}, \tag{4.14}$$

where

$$S_{j,n} = \frac{\partial E_{j,k}}{\partial y_{n,k-1}} \ , \ S_{j,n+N} = \frac{\partial E_{j,k}}{\partial y_{n,k}}. \tag{4.15}$$

A similar argument can be used for the boundary conditions (single variable Taylor expansion)

$$-E_{j,1} = \sum_{n=1}^{N} S_{j,n} \Delta y_{n,1}, \tag{4.16}$$

where

$$S_{j,n} = \frac{\partial E_{j,1}}{\partial y_{n,1}} \tag{4.17}$$

and

$$-E_{j,M+1} = \sum_{n=1}^{N} S_{j,n} \Delta y_{n,M}, \tag{4.18}$$

where

$$S_{j,n} = \frac{\partial E_{j,M+1}}{\partial y_{n,M}}. \tag{4.19}$$

For the internal points, k, the $S_{j,n}$ matrices are of size 6x12 and supply a block of 6 equations each coupling 12 corrections to the solution at the points k and $k-1$. As noted above the S matrix elements will depend upon the ordering of the state variables y_j's and this will dictate the boundary conditions. For these reasons the calculation of the E's, and their derivatives S_j's, is a complex process and will change relative to the type of contact simulated. For example the ordering of these equations will change for a left hand side (LHS) and right hand side (RHS) ohmic contact compared with that of a LHS Schottky contact and a RHS ohmic

contact. Appendix B shows the y_j's, E_j's and S_j's for the two Schottky contact case.

4.2 Internal Mesh Points

The values of the state variable at each mesh point are denoted by $y_{j,k}$, where j refers to the variable and k to the mesh point. The ordering of these equations for Schottky contacts and ohmic contacts is as follows:

Schottky Ordering

$$\begin{array}{lll} y_{1,k} = \psi(x_k) & y_{2,k} = J_n(x_k) & y_{3,k} = J_p(x_k) \\ y_{4,k} = D(x_k) & y_{5,k} = \phi_n(x_k) & y_{6,k} = \phi_p(x_k) \end{array} \tag{4.20}$$

Ohmic Ordering

$$\begin{array}{lll} y_{1,k} = \psi(x_k) & y_{2,k} = \phi_n(x_k) & y_{3,k} = \phi_p(x_k) \\ y_{4,k} = D(x_k) & y_{5,k} = J_n(x_k) & y_{6,k} = J_p(x_k). \end{array} \tag{4.21}$$

For brevity only the Schottky ordering case will be considered, which can be generalised to a two sided Schottky model. The difference equations, $E_{j,k}$, on a variable mesh can be described by the following equations:

$$E_{1,k} = y_{2,k} - y_{2,k-1} + q\Delta G(\bar{x})\Delta x_k \tag{4.22}$$

$$E_{2,k} = y_{3,k} - y_{3,k-1} - q\Delta G(\bar{x})\Delta x_k \tag{4.23}$$

$$E_{3,k} = y_{4,k} - y_{4,k-1} - q\Delta x_k(\bar{p} - \bar{n} + N_D^+(\bar{x}) - N_A^-(\bar{x})) \tag{4.24}$$

$$E_{4,k} = (y_{2,k} + y_{2,k-1})\frac{\Delta x_k}{2} + q\mu_n(\bar{x})\bar{n}(y_{5,k} - y_{5,k-1}) \tag{4.25}$$

$$E_{5,k} = (y_{3,k} + y_{3,k-1})\frac{\Delta x_k}{2} + q\mu_p(\bar{x})\bar{p}(y_{5,k} - y_{5,k-1}) \tag{4.26}$$

$$E_{6,k} = (y_{4,k} + y_{4,k-1})\frac{\Delta x_k}{2} + \epsilon_0\epsilon_s(\bar{x})(y_{1,k} - y_{1,k-1}), \tag{4.27}$$

where

$$\Delta x_k = (x_k - x_{k-1}) \tag{4.28}$$

$$\bar{x} = \left(\frac{x_k + x_{k+1}}{2}\right) \tag{4.29}$$

$$\bar{y}_{j,k} = \left(\frac{y_{j,k} + y_{j,k-1}}{2}\right) \tag{4.30}$$

$$\bar{n} = n(\bar{x}, \bar{y}_1, \bar{y}_5) \tag{4.31}$$

$$\bar{p} = p(\bar{x}, \bar{y}_1, \bar{y}_6). \tag{4.32}$$

4.3 Boundary Conditions

The boundary conditions used will depend upon the required contacts for the device simulation. In chapter 3 ohmic and Schottky boundary conditions were discussed and will be covered again here. The boundary conditions are listed below for the two possible cases. The bias voltage V_{app} can be applied at either the ohmic or the Schottky contact. For the boundary conditions shown, the bias voltage will be applied to the RHS, although the simulation software allows the user to select either side regardless of the contact type. If one of the contacts is ohmic, then it is normal for the bias voltage to be applied at that contact, as this method is covered in standard texts. The boundary conditions for a LHS or RHS Schottky contact are:

LHS Schottky Contact

$$\psi(x_1) = -\phi_{BN}(x_1) \tag{4.33}$$

$$J_n(x_1) = qV_{rn}(x_1)n_{eq}(x_1)\left[\exp\left(-\beta\phi_n(x_1)\right) - 1\right] \tag{4.34}$$

$$J_p(x_1) = -qV_{rp}(x_1)p_{eq}(x_1)\left[\exp\left(\beta\phi_p(x_1)\right) - 1\right] \tag{4.35}$$

$$n_{eq}(x_1) = N_C(x_1)\exp\left(-\beta\phi_{BN}(x_1)\right) \tag{4.36}$$

$$p_{eq}(x_1) = N_V(x_1)\exp\left[-\beta\left(\frac{E_g(x_1)}{q} - \phi_{BN}(x_1)\right)\right] \tag{4.37}$$

RHS Schottky Contact

$$\psi(x_M) = -\phi_{BN} + V_{app} \tag{4.38}$$

$$J_n(x_M) = qV_{rn}(x_M)n_{eq}(x_M)\left\{\exp\left[-\beta\left(\phi_n(x_M) + V_{app}\right)\right] - 1\right\} \tag{4.39}$$

$$J_p(x_M) = -qV_{rp}(x_M)p_{eq}(x_M)\left\{\exp\left[\beta\left(\phi_p(x_M) + V_{app}\right)\right] - 1\right\} \tag{4.40}$$

$$n_{eq}(x_M) = N_C(x_M)\exp\left(-\beta\phi_{BN}(x_M)\right) \tag{4.41}$$

$$p_{eq}(x_M) = N_V(x_M)\exp\left[-\beta\left(\frac{E_g(x_M)}{q} - \phi_{BN}(x_M)\right)\right], \tag{4.42}$$

and for a LHS or RHS ohmic contact on n-type material:

LHS ($x = x_1$) or RHS ($x = x_M$) Ohmic Contact

$$\psi(x) = \frac{1}{\beta}\log_e\left(\frac{n(x)}{N_C(x)}\right) + \phi_n(x) - \frac{\chi_c(x)}{q} \tag{4.43}$$

$$\phi_n(x) = V_{app} \tag{4.44}$$

$$\phi_p(x) = V_{app} \tag{4.45}$$

$$n(x) = N_D(x) \tag{4.46}$$

$$p(x) = \frac{n_i^2}{N_D(x)}, \tag{4.47}$$

where $\beta = q/k_BT$. These boundary conditions can then be mixed to form the required device structure for the simulation. For our one dimensional simulation there are 4 possible permutations:

1. LHS Schottky contact and a RHS ohmic contact (Schottky ordering);
2. LHS Schottky contact and a RHS Schottky contact (Schottky ordering);
3. LHS ohmic contact and a RHS Schottky contact (ohmic ordering);
4. LHS ohmic contact and a RHS ohmic contact (ohmic ordering).

These possibilities require 2 ordering schemes for the variables $y_{j,k}$. Only the Schottky ordering case as outlined in equations (4.20) for examples (1) and (2) above will be covered. The ohmic ordering case can be generated in a similar manner.

On a mesh 1 to M the boundary points are $k = 1$ and $k = M + 1$, where the state variables for the LHS boundary conditions are $\psi(x_1)$, $J_n(x_1)$ and $J_p(x_1)$. The y_j's are defined as:

$$y_{1,1} = \psi(x_1) = -\phi_{BN} + V_{app} \tag{4.48}$$
$$y_{2,1} = J_n(x_1) \tag{4.49}$$
$$y_{3,1} = J_p(x_1), \tag{4.50}$$

where $\phi_n(x_1)$ and $\phi_p(x_1)$ are free to float from their initial conditions. The E_j's are defined as:

$$E_{4,1} = y_{1,1} - \psi(x_1) \tag{4.51}$$
$$E_{5,1} = y_{2,1} - qV_{rn}(x_1)n_{eq}(x_1)\left[\exp\left(-\beta\phi_n(x_1)\right) - 1\right] \tag{4.52}$$
$$E_{6,1} = y_{3,1} + qV_{rp}(x_1)p_{eq}(x_1)\left[\exp\left(\beta\phi_p(x_1)\right) - 1\right]. \tag{4.53}$$

At the right hand side contact there are two possible boundary conditions, Schottky or ohmic. The y_j's and E_j's for a Schottky contact on n-type material are defined as:

$$y_{1,M} = \psi(x_M) \tag{4.54}$$
$$y_{2,M} = J_n(x_M) \tag{4.55}$$
$$y_{3,M} = J_p(x_M) \tag{4.56}$$
$$E_{1,M+1} = y_{1,M} - \psi(x_M) \tag{4.57}$$
$$E_{2,M+1} = y_{2,M} - qV_{rn}(x_M)n_{eq}(x_M)\left[\exp\left(-\beta\phi_n(x_M)\right) - 1\right] \tag{4.58}$$

$$E_{3,M+1} = y_{3,M} + qV_{rp}(x_M)p_{eq}(x_M)\left[\exp\left(\beta\phi_p(x_M)\right) - 1\right], \tag{4.59}$$

and for a equivalent ohmic contact are

$$y_{1,M} = \psi(x_M) = \frac{1}{\beta}\log_e\left(\frac{n(x_M)}{N_c(x_M)}\right) + V_{app} - \frac{\chi_c(x_M)}{q} \tag{4.60}$$

$$y_{5,M} = \phi_n(x_M) = V_{app} \tag{4.61}$$

$$y_{6,M} = \phi_p(x_M) = V_{app} \tag{4.62}$$

$$E_{1,M+1} = y_{1,M} - \psi(x_M) \tag{4.63}$$

$$E_{2,M+1} = y_{5,M} - \phi_n(x_M) \tag{4.64}$$

$$E_{3,M+1} = y_{6,M} - \phi_p(x_M). \tag{4.65}$$

where the bias voltage V_{app} is applied at either the LHS or the RHS.

4.4 Results

To test this fully bipolar method a comparison of the results for the unipolar Schottky devices of chapter 3 section 3.4.2 will be made. The device geometries are shown in figures 4.1a - 4.1c. Geometry (a) consists of an LHS gold contact, an n-type Si layer and an RHS ohmic contact. Geometries (b) and (c) consist of an LHS ohmic contact, a n-type layer, an n^+ doped contact layer and a RHS metal contact, where the semiconductor and metal contacts are Si and tungsten for geometry (b) and GaAs and gold for geometry (c).

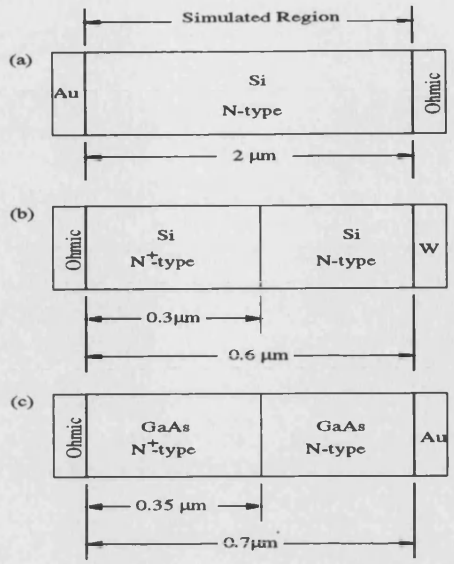

Figure 4.1: Devices simulated.

Figures 4.2, 4.3 and 4.4 show the same results as per chapter 3 with the additional numerical results provided by the bipolar simulation method of SOLVDE (filled diamonds). For all 3 device geometries the new bipolar method is in agreement with the analytical and numerical approaches previously discussed and is stable for applied biases in excess of the built in potential.

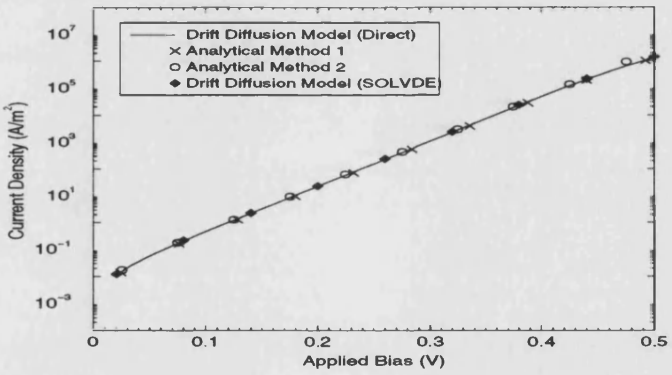

Figure 4.2: Comparison of current density curves for numerical and analytical solutions to a unipolar (n-type) Au-Si Schottky diode.

The SOLVDE approach has several advantages over the Direct and SOR numerical models previously discussed:

- Significantly faster convergence (see simulation bench marks in Appendix A) for equivalent device structures and number of mesh points;

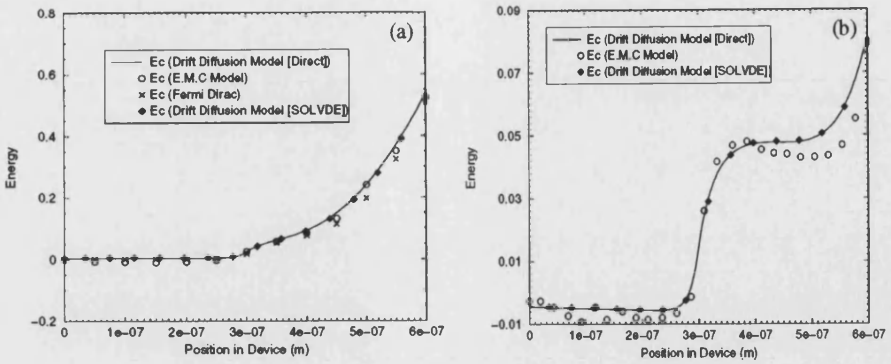

Figure 4.3: Comparison of two numerical solutions to a n-type Si-W Schottky diode; Drift Diffusion model (solid) and EMC model (∘). Panels (a) and (b) show the conduction band profiles for $V_{app} = 0V$ and $V_{app} = 0.44V$ respectively.

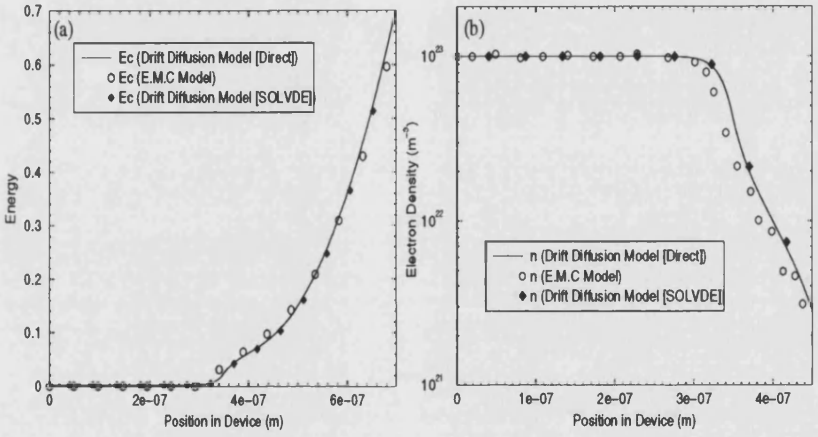

Figure 4.4: Comparison of two numerical solutions to a n-type GaAs-Au Schottky diode; Drift Diffusion model (solid) and EMC model (∘). Panels (a) and (b) show the conduction band profiles and electron carrier densities, for $V_{app} = 0V$, respectively.

- Stable for bipolar Schottky contact;
- Can be generalised for dual Schottky contacts;
- Solves directly for the electron and hole current densities, whereas, the SOR and Direct methods require post processing to generate the current densities;
- The boundary conditions can be easily generalised to include tunnelling and barrier height lowering.

However, there are disadvantages to the SOLVDE approach:

- The considerable time taken to manually generate the derivatives (S_j's) for different state variable ordering schemes;
- The initial guesses, for the 6 state variable, have to be reasonably accurate for SOLVDE to form a converged solution. This restriction requires the bias voltage to be gradually ramped up to the required applied potential. The Direct and SOR approaches can be solved, without restriction, for applied biases in the range $0 < V_{app} < V_{bi}$, from the initial linear rising guesses.

The incremental applied bias approach implies that it will be slower than for the Direct or SOR method. Fortunately this is not necessarily the case. An iterative method has been implemented that uses the previous solutions, to the 6 state variables, with the newly calculated boundary conditions to the next solution. (For the Schottky contact case the current densities for the previously converged solution are used). This results in an accurate guess for the next solution provided the applied voltage increment is small ($\Delta V_{app} < 0.1V$) thus rapidly forming the new solution. This approach generates, as a bi-product, the current density-voltage characteristic automatically, and for equivalent device structures and number of mesh points is faster than the Direct and SOR methods.

4.4.1 Fully Bipolar Schottky Device

Figure 4.5 shows the geometry of a bipolar Schottky barrier device (BSBD) [3]. The device consists of a LHS Schottky contact, a Si Gaussian doped n-type epitaxial region, a Si n^+ doped substrate layer and a RHS ohmic contact.

A depiction of the forward bias current density-voltage characteristic for a Schottky barrier device (SBD) and a BSBD are shown in figure 4.6. Referring to figure 4.6, as the forward bias voltage increases the device obeys an exponential law due to thermionic emission (part A). As the current density increases further it deviates from this exponential law due to the high epitaxial resistance (part B). In a conventional SBD the voltage drop rapidly increases and the current density profiles flatten out (part C). In a BSBD the minority carrier current, injected from the bipolar Schottky contact, lowers the resistances of the epitaxial layer, thus allowing a higher current density to be extracted from the device (part D).

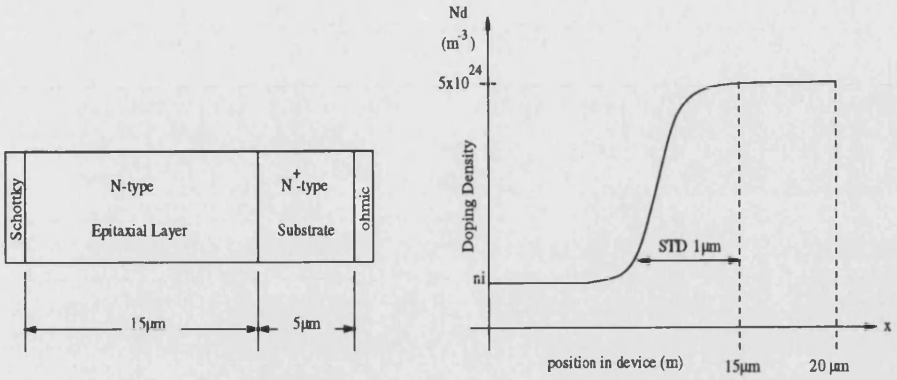

Figure 4.5: BSBD geometry and doping profile.

Eventually hole injection limiting occurs and the current density-voltage curve tails off (part E).

The low field operation is controlled by the barrier to electron injection (ϕ_{Bn}) at the Schottky contact, whereas the high field operation is governed by the barrier to hole injection (ϕ_{Bp}). This device therefore forms an ideal test of the bipolar Schottky contact simulation model.

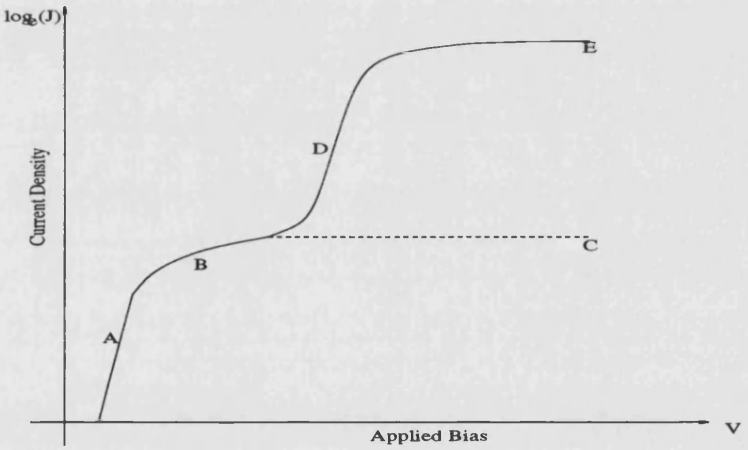

Figure 4.6: Representation of current density-voltage regions for a SBD and a BSBD. The labels represent (A) thermionic emission, (B) majority electron saturation, (C) SBD current density limit, (D) minority hole injection for BSBD and (E) minority hole injection limiting for BSBD.

Figures 4.7 compare the current density-voltage characteristics for the bipolar drift diffusion model (SOLVDE) and those of Amemiya et al (1984), for hole barriers heights in the range ($0.15\text{eV} < \phi_{Bp} < 0.55\text{eV}$). Both models are in good agreement with the transition from unipolar to bipolar transport clearly visible

for forward biases $V_{app} > 0.5V$ and hole barrier heights $\phi_{Bp} < 0.45\text{eV}$.

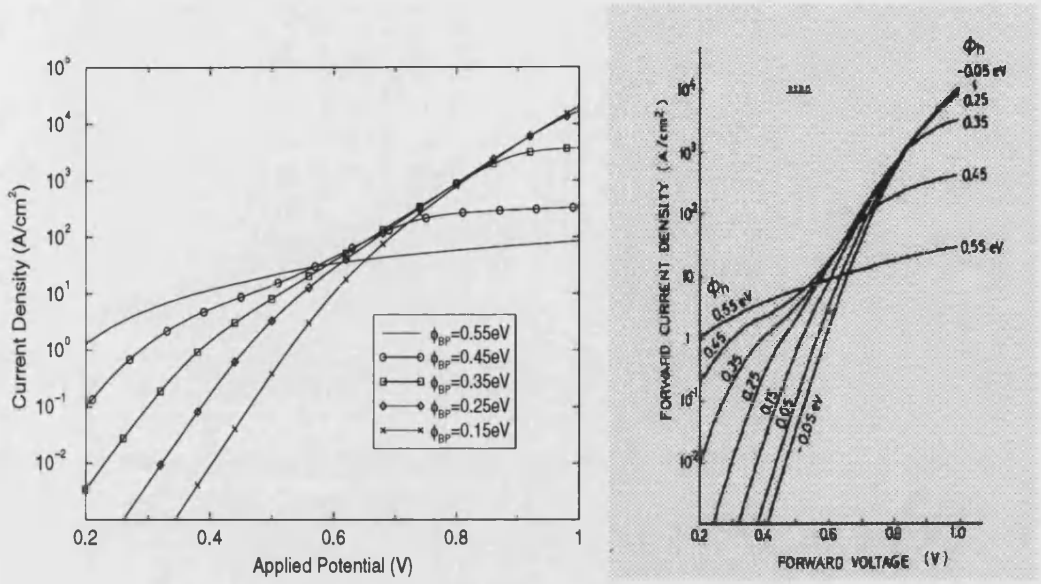

Figure 4.7: The left hand figure shows current density-voltage curves, for the BSBD shown in figure 4.5, using the SOLVDE numerical DDM. The right hand figure shows the current density-voltage curve for the same device, and are taken from the following reference: Y Amemiya and Y Mizushima, (1984).

4.5 Organic Modifications

To successfully model OLEDs a variety of changes to the inorganic model have to be made. These changes can be separated into two groups: boundary conditions and bulk transport properties. These are summarised below:

Boundary Conditions:

1. Barrier height lowering due to the small static dielectric constant ($\epsilon_s \approx 3$) in OLEDs;
2. An organic hopping based recombination velocity at the Schottky contact potential energy maximum;
3. Fowler-Nordhiem tunnelling in the high field regime;

Bulk Properties:

1. Electron and hole trapping;
2. Field dependent mobilities;
3. Bimolecular recombination.

4.5.1 Barrier Height Lowering

The barrier heights to carrier injection have so far been assumed to be independent of the applied bias. However, in reality these barriers to injection will be reduced by an effect known as the image force. The image force results from considering the electrostatics of a electron at a distance x from the metal-semiconductor interface. The electron induces an opposite charge at the distance $-x$ behind the metal. Therefore, the attractive image force is

$$F = \frac{-q^2}{16\pi\epsilon_s\epsilon_0 x^2}. \tag{4.66}$$

By considering the work done by the electron from infinity to the position x it is possible to determine potential energy

$$PE(x) = \frac{q^2}{16\pi\epsilon_0\epsilon_s x} + qEx \tag{4.67}$$

therefore, the Schottky barrier lowering at x_m (the metal-semiconductor interface) is given by the condition $\mathrm{d}[PE(x)]/\mathrm{d}x = 0$

$$\Delta\phi = \sqrt{\frac{qD}{4\pi\left(\epsilon_0\epsilon_s\right)^2}}. \tag{4.68}$$

Barrier height lowering can therefore be implemented by the following equations, where the fixed barrier to electron injection ϕ_{Bn0} is reduced by the quantity $\Delta\phi$

$$\phi_{Bn} = \phi_{Bn0} - \Delta\phi, \tag{4.69}$$

and for the barrier to hole injection

$$\phi_{Bp} = E_g - (q\phi_{Bn0} - \Delta\phi)\,. \tag{4.70}$$

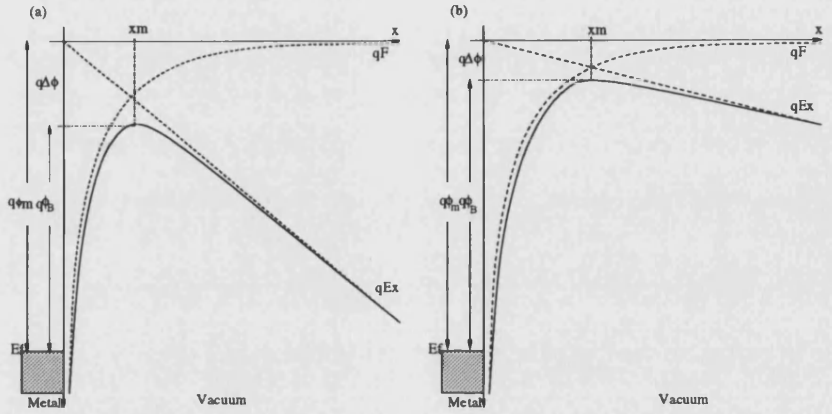

Figure 4.8: Energy band diagram between a metal surface and a vacuum. Panels (a) and (b) show the image force (F), the band profile (solid line) and the potential profile (qEx) for two cases of the electric field profile at the metal vacuum interface. The magnitude of the barrier lowering ($\Delta\phi$) is due the combined effect of the field and the image force.

Figures 4.8a and 4.8b show the combined effect of the electric field and the image force in determining the magnitude of the barrier height lowering at x_m within the device. The introduction of barrier height lowering into the boundary conditions is straight forward, with the fixed barrier heights being replaced by equations (4.69) and (4.70). The electric field sign at the Schottky contact must be monitored in order to ascertain whether barrier height lowering is applicable.

Figures 4.9(a) and (b) show the effect of barrier height lowering on device geometry (a) figure 4.1. Panel (b) shows the conduction and valence bands with and without barrier height lowering for zero bias. It can be seen that the barrier to electron injection is reduced, whilst the hole barrier is increased. The effect on the current voltage curve (panel (a)) shows that the current density is slightly increased due to the lowering of the majority carrier barrier to thermionic emission. The barrier lowering effect occurs for $V_{app} < V_{bi}$ as the sign of the electric field at the LHS contact is negative. For applied biases greater than the built in

potential the field sign is positive and therefore barrier height lowering is turned off. The current voltage characteristic for the barrier height lowering case will therefore converge onto the barrier independent case for $V_{app} > V_{bi}$ $(\approx 0.68V)$.

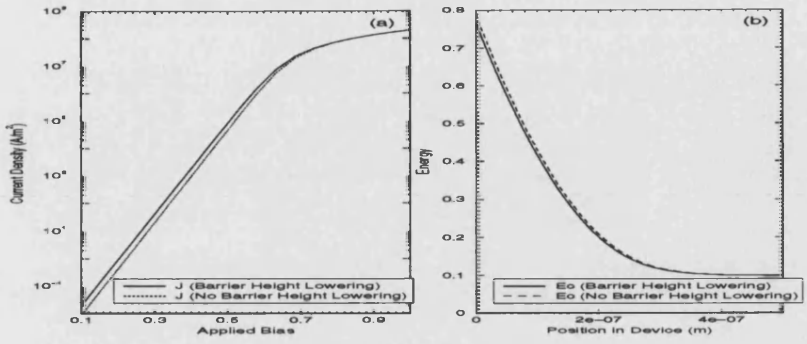

Figure 4.9: Panel (a) shows the current density-voltage characteristics for device (a) with and without barrier height lowering and panel (b) shows E_c for with and without barrier height lowering.

For inorganic devices the reduction in barrier height is small but for a PPV OLED the static dielectric constant is approximately 3. From equation (4.68) it can been seen that barrier height lowering will increase for organic devices. Figures 4.10a and 4.10b show analytical solutions to the barrier height lowering equations above. The magnitude of the barrier lowering can be seen to increase substantially for a dielectric constant that is typical of PPV OLEDs.

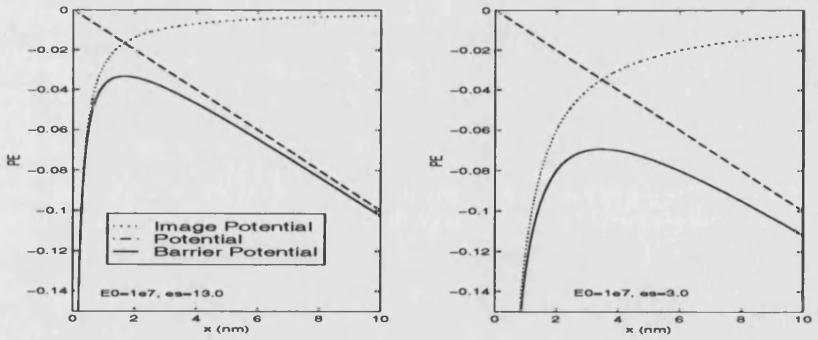

Figure 4.10: Plot of the effect of the dielectric constant on the magnitude of the barrier height lowering. Panel (a) shows the image potential (dotted), the potential profile (dashed) and the resultant image force lowered potential profile (solid) for $\epsilon_s = 13$. Panel (b) as per Panel (a) with $\epsilon_s = 3.0$

4.5.2 Tunnelling

Fowler Nordheim tunnelling has been proposed as the dominant injection mechanism in OLEDs [4] [5] [6] [7] [8]. This can be seen by considering the conduction band of an OLED under forward bias ($V_{app} \gg V_{bi}$).

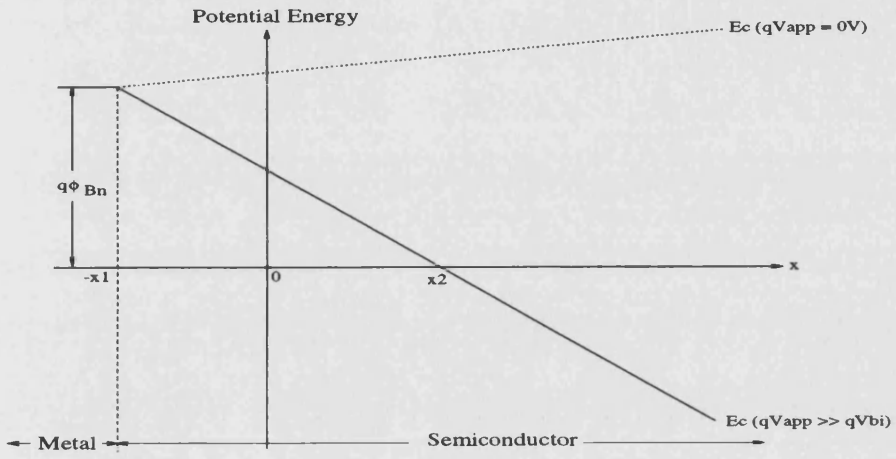

Figure 4.11: OLED conduction band representation for zero and forward bias.

The transmission probability T_{FN} can be given by the WKB approximation (Wentzel-Kramers-Brillouin method)[9]

$$T_{FN} = \exp\left[-2\int_{-x1}^{x2} |k(x)|\mathrm{d}x\right], \tag{4.71}$$

where $|k(x)|$ is the absolute value of the wave vector and $-x1$ and $x2$ are the classical turning points. For the triangular barrier shown in figure 4.11 the wave vector is given by

$$k(x) = \sqrt{\frac{2m^*}{\hbar^2}\left(\frac{q\phi_{Bn}}{2} - qEx\right)}. \tag{4.72}$$

Therefore the tunnelling probability, of an electron, through the potential energy barrier is given by

$$T_{FN} = \exp\left(-\frac{4\sqrt{2m^*}(q\phi_{Bn})^{3/2}}{3q\hbar E}\right). \tag{4.73}$$

The injected electron current density through the potential barrier is given by the following expressions for zero bias (J^e_{FN0}) and foward bias (J^e_{FN}) respectively [10]:

$$J^e_{FN} = \alpha_1\left(\frac{C}{q\phi_{Bn}}\right)E^2\exp\left[-\alpha_2 B\left(\frac{(q\phi_{Bn})^{3/2}}{E}\right)\right] \tag{4.74}$$

$$J^e_{FN0} = \alpha_1\left(\frac{C}{q\phi_{Bn0}}\right)E_0^2\exp\left[-\alpha_2 B\left(\frac{(q\phi_{Bn0})^{3/2}}{E_0}\right)\right], \tag{4.75}$$

where E_0 and ϕ_{Bn0} are the zero bias electric field and the barrier to electron injection respectively, α_1 and α_2 are fitting parameters and constants C and B are given by the following expressions

$$C = \frac{8\pi\sqrt{2m^*}}{3hq} \tag{4.76}$$

$$B = \frac{2.2q^3}{8\pi h}. \tag{4.77}$$

The above expressions for tunnelling can be formed into a more compact form using equation (4.78) below

$$J_{te} = J^e_{FN0}\left[\frac{J^e_{FN}}{J^e_{FN0}} - 1\right]. \tag{4.78}$$

Introducing the tunnelling current into the boundary conditions is not straight forward. The LHS and RHS Schottky barriers to electron and hole injection have to be checked for the correct barrier shape. The shape of the barriers to injection change with increasing applied bias and so have to be continually monitored to ascertain whether tunnelling should be used.

4.5.3 Electron and Hole Trapping

Electron and hole trapping in OLEDs has been widely suggested [11]. Traps can be considered as existing at discrete energy levels (E_{tj}) within the bandgap or alternatively as a distribution of energy levels with a characteristic energy and temperature [12]. OLED materials such as PPV are highly disordered and are therefore usually modelled as either exponential or Gaussian distribution of traps in energy. For our numerical model we implemented hole and electron traps existing at discrete energy levels. The number of trap energy levels, the density of traps and the degeneracy of the traps are controlled by the user through the input files.

The number of trapped electrons or holes, at the j^{th} discrete trap energy level, can be calculated using Fermi-Dirac statistics

$$n_{tj} = \frac{N_{tj}}{1 + (1/g)\exp\left(\frac{E_{tj} - E_{fn}}{k_B T}\right)} \tag{4.79}$$

$$p_{tj} = \frac{P_{tj}}{1 + (1/g)\exp\left(\frac{E_{fp} - E_{tj}}{k_B T}\right)}. \tag{4.80}$$

For the j^{th} trap energy level n_{tj} and p_{tj} are the electron and hole total trap densities, E_{tj} is the trap energy level below the conduction band edge E_C, g is the degeneracy (statistical weight) of the trap and E_{fn} and E_{fp} are the electron and hole Fermi energy levels within the semiconductor. N_{tj} and P_{tj} are the maximum trap occupation densities for electrons and holes respectively. To implement trapping Poisson's equation has to be modified to include the presence of trapped charge

$$\frac{\partial(E\epsilon_s)}{\partial x} = \frac{\partial D}{\partial x} = \frac{q}{\epsilon_0}\left[p - n + N_D^+ - N_A^- + \left(\sum_{j=1}^{N} p_{tj} - p_{tj0}\right) - \left(\sum_{j=1}^{N} n_{tj} - n_{tj0}\right)\right], \tag{4.81}$$

where n_{tj0} and p_{tj0} are the equilibrium electron and hole trap densities.

4.5.4 Field Dependent Mobilities

Both field and temperature dependent mobilities have been proposed for PPV based OLEDs [13]. A common field dependent form[14], that we have implemented, is shown below

$$\mu = \mu_0 \exp\left(\sqrt{\frac{E}{E_0}}\right), \tag{4.82}$$

where E_0 is a material dependent parameter determined by experiment. This form was chosen due to its ease of implementation and field independent mobilites could be implemented by choosing $E_0 \gg E$. This allows materials with fixed and field dependent mobilities to be simulated in different layers within the same device structure.

4.5.5 Langevin Bimolecular Recombination

The two recombination mechanisms we have discussed are trap assisted SRH and optical. For OLEDs the optical recombination process has been proposed to be of a Langevin bimolecular form [14] [15] and this form was implemented within the organic simulation model. Langevin recombination is shown below in equation (4.83)

$$R_{opt} = \lambda\left(np - ni^2\right) \tag{4.83}$$

$$\lambda = \frac{4\pi q \mu_{n,p}}{\epsilon_s \epsilon_0}, \tag{4.84}$$

where $\mu_{n,p}$ is an effective recombination mobility which is taken to be the larger of the electron and hole mobilities.

4.5.6 Organic Recombination Velocity

In crystalline inorganic devices carriers are free to propagate into the conduction band with a thermal distribution of kinetic energies. There are two contributions to the current, $J_{m\to s}$ and $J_{s\to m}$, which are balanced at thermal equilibrium (zero bias). For organic structures the material is amorphous not crystalline and charge transport is no longer free propagation in excited states but rather hopping between localised states. The organic recombination velocity is based on the premise that it is analogous to Langevin bimolecular recombination and can be considered to be a field enhanced diffusion process [15]. The zero field form for V_r is given below and was implemented in the organic simulation software

$$V_r = \frac{16\pi\epsilon_s\epsilon_0(k_BT)^2\mu(E)}{q^3}, \tag{4.85}$$

This results in a substantially reduced recombination velocity compared with that of crystalline inorganic materials.

4.6 Single Layer Organic Device

A simple single layer OLED, will now be considered, with a hole injecting LHS Schottky contact, a PPV emission layer and a electron injecting RHS Schottky contact, see figure 4.12 with the material parameters given in table 4.1. This device is only a test example, but the device geometry and material parameters used are typical of OLEDs [11] [14].

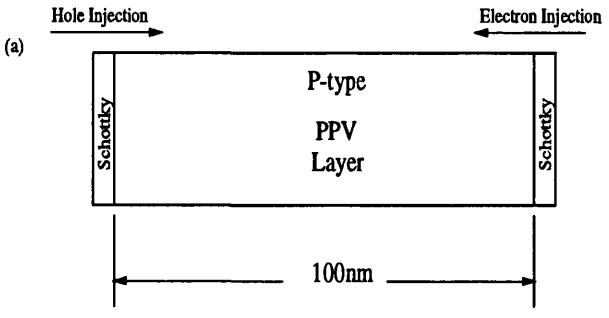

Figure 4.12: Organic device geometry.

Material Parameters	PPV Layer	Units
T	290	K
ϵ_s	3.0	-
E_g	2.4	eV
χ_c	2.05	eV
N_A	$1x10^{22}$	m^{-3}
N_C	$2.5x10^{26}$	m^{-3}
N_V	$2.5x10^{26}$	m^{-3}
μ_{n0}	$5x10^{-12}$	$m^2/(Vs)$
μ_{p0}	$1x10^{-10}$	$m^2/(Vs)$
E_0	$1x10^{7}$	V/m
m^*	1.0	-
$\phi_{Bn}(rhs)$	0.8	eV
$\phi_{Bp}(lhs)$	0.3	eV
α_1	1.0	-

Table 4.1: . Organic material parameters.

Figures 4.13a and 4.13b show the current density-voltage curves for field dependent and independent mobilities respectively. For both panels we compare the effect of barrier height lowering and tunnelling. For the field dependent mobility case (panel (a)) the effect of barrier height lowering can be seen to increase the current density, over the barrier independent case. Barrier height lowering initially occurs at the RHS Schottky contact (thermionic emission region of the JV characteristic). As the applied potential increases, past the built-in potential ($V_{bi} \approx 1.3V$), the sign of the electric field switches at the LHS and RHS Schottky contacts. Therefore, barrier height lowering turns off at the RHS and turns on at the LHS. The barrier height lowering effect at the LHS causes the second increase on the JV curve for $V_{app} > V_{bi}$ over the barrier independent case. The gradients of the barrier independent and barrier height lowering cases are $J \propto V^2$ and $J \propto V^4$ respectively. For the tunnelling case, the JV curve follows the barrier independent case before the effect of tunnelling dominates at $V_{app} \approx 5.0V$ and saturates onto a similar gradient to the barrier height lowering case. This is in good agreement with analytical solutions to the Fowler Nordheim tunnelling equations assuming a uniform electric field profile V_{app}/L and a barrier to hole injection of 0.3eV. This shows that tunnelling dominates at the LHS hole injecting contact as expected.

For the field independent mobilities cases (panel (b)) the effects of barrier height

lowering and tunnelling are the same as for the field dependent cases. However, the current density-voltage characteristics do not saturate onto the same gradients as the field dependent cases. For the barrier height lowering and tunnelling cases the gradients for $V_{app} > V_{bi}$ are $J \propto V^3$ and for the barrier height independent case $J \propto V$. This is due entirely to the the field dependence of the mobilities.

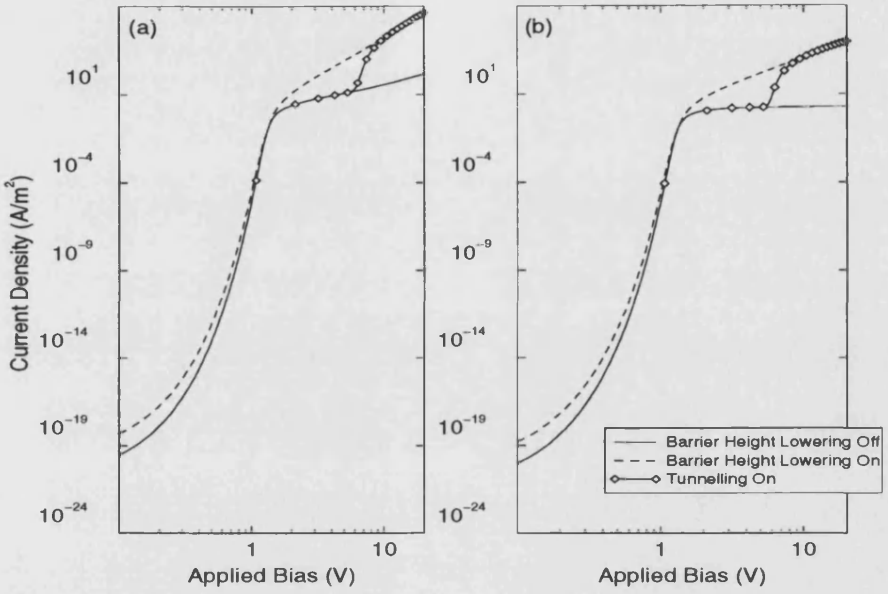

Figure 4.13: Example current-density voltage characteristics showing thermionic emission diffusion (TED) (-), TED with barrier height lowering (–) and TED with Fowler Nordheim field emission (o). Panel (a) shows the effect of a field dependent mobilities and panel (b) with field independent mobilities.

4.7 Conclusions

The first order Newton approach of SOLVDE has been shown to be stable for both inorganic and organic devices. This method is in agreement with the analytical and numerical results of chapter 3 for unipolar Schottky diodes and agreement has been achieved with published results for a bipolar Schottky diode simulation. The organic modification to the simulation model have been detailed and results presented for a single layer organic device. The simulation model is stable for organic device structures and parameters sets that are characteristic of OLEDs. This model is now suitable to investigate the major aims of this thesis. These are the injection mechanisms, carrier transport and bulk properties of OLEDs.

The model is capable of simulating a variety of inorganic and organic device structures, with a flexible choice of boundary conditions and bulk material properties. Figure 4.14 shows a schematic representation of the user options in modelling a device.

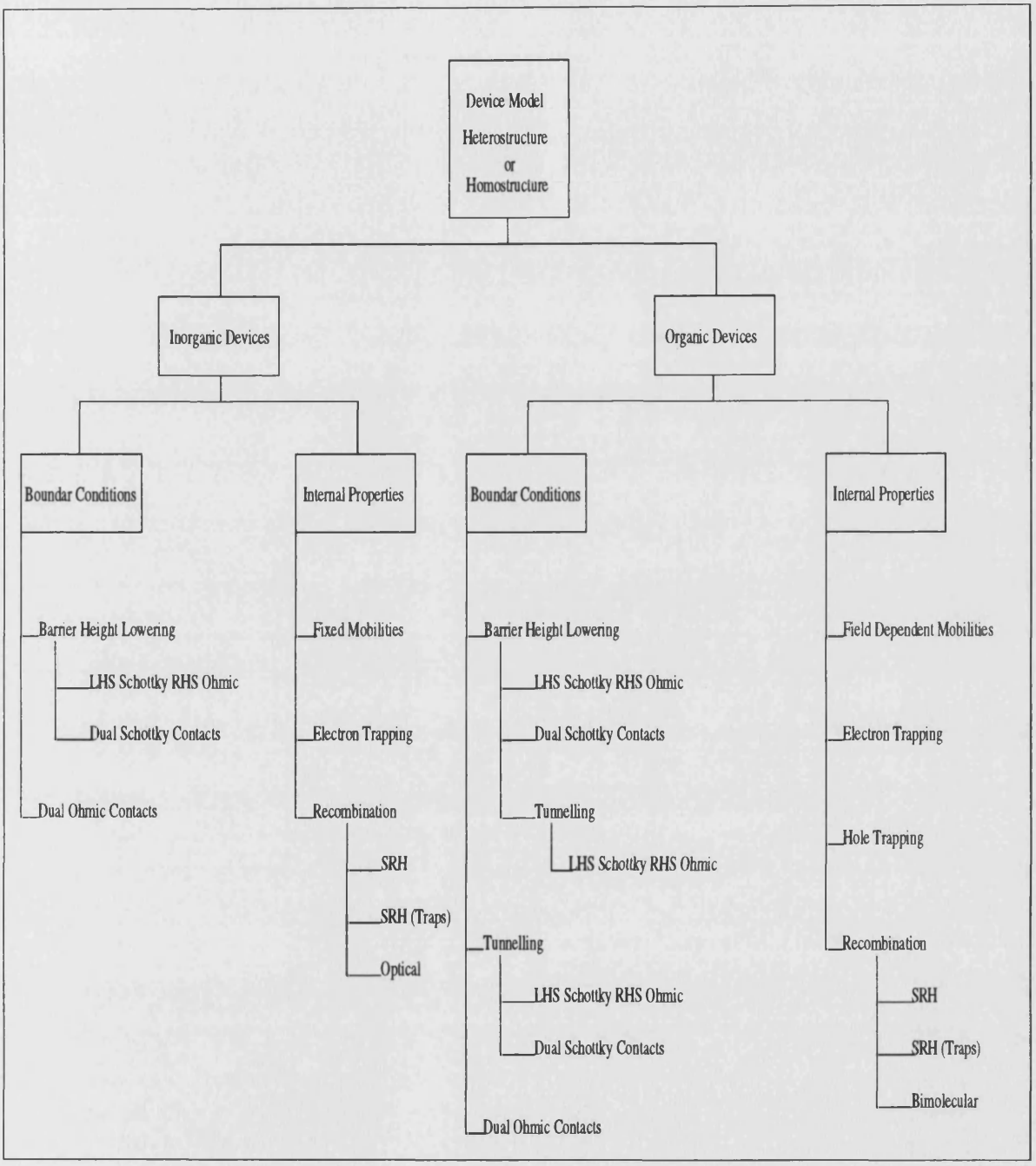

Figure 4.14: Simulation Program: schematic representation of possible options.

References

[1] S. J. Woods, *Ph.D. Thesis*, University of East Anglia School of Physics, (1998).

[2] W. H. Press, B P Flannery, S. A. Teulolsky and W. T. Vertterling, *Numerical Recipes in Fortran*, Cambridge University Press, Cambridge (1989).

[3] Y. Amemiya and Y. Mizushima, *I.E.E.E. Transactions on Electron Devices*, **ED-31**, 35-42, 1984.

[4] I. D. Parker, *Journal of Applied Physics*, **75**, 1656-1666, 1993.

[5] P. S. Davids, S. M. Kogan, I. D. Parker and D. L. Smith, *Applied Physics Letters*, **69**, 2270-2272, 1996.

[6] G. G. Malliaras and J. C. Scott, *Journal of Applied Physics*, **83**, 5399-5403, 1997.

[7] Y. Kawabe, M. M. Morrell, G. E. Jabbour, S. E. Shaheen, B. Kippelen and N. Peyghambarian, *Journal of Applied Physics*, **84**, 5306-5314, 1998.

[8] J. M. Lupton and I. D. S. Samuel, *J. Phys. D: Applied Physics*, **32**, 2973-2984, 1999.

[9] See for example: K. F. Brennan, *The physics of Semiconductors with Applications to Optoelectronic Devices*, Cambridge University Press, Cambridge, (1999); S. Sze, *Physics of Semiconductor Devices*, John Wiley and Sons, (1981).

[10] R. H. Fowler and L. Nordheim, *Proceedings of the Royal Society*, **119**, 173-181, 1928.

[11] See for example: A. J. Campbell, D. D. C. Bradley and D. G. Lidzey, *Journal of Applied Physics*, **82**, 6326-6342, 1997; P. W. M. Blom, M. J. M. de Jong, C. T. H. F. Liedenbaum and J. J. M. Vleggaar, *Synthetic Metals*, **85**, 1997.

[12] M. A. Lampert and P. Marks, *Current injection in Solids*, Academic Press, New York and London, (1970)

[13] P. W. M. Blom, M. J. M. de Jong and M. G. van Munster, *Physical Review B*, **55**, R656-R659, 1997.

[14] B. K. Crone, P. S. Davids, I. H. Campbell and D. L. Smith, *Journal of Applied Physics*, **84**, 833-842, 1998.

[15] J. C. Scott and G. G. Malliaras, *Chemical Physics Letters*, **299**, 115-119, 1998.

Chapter 5

Poly(phenylene Vinylene) (PPV) Device Simulation

A	:	Device Area
ϵ_s	:	Static Dielectric Constant
μ_{n0}	:	Zero Field Electron Mobility
μ_{p0}	:	Zero Field Hole Mobility
E_0	:	Field Dependence Factor
N_c	:	Density of states in the conduction band
N_v	:	Density of states in the valence band
N_A	:	Acceptor doping density
E_g	:	Energy gap
α_1	:	Pre-factor for tunnelling
$q\phi_{Bn}(lhs)$	:	Barrier to electron injection (LHS)
$q\phi_{Bp}(rhs)$	:	Barrier to hole injection (RHS)

Table 5.1: Description of the material parameters used.

In this chapter results will be presented for a simple single layer, organic device structure based on the organic polymer material poly(phenylene vinylene) (PPV). The numerical model used in these simulations is the previously described drift diffusion model (DDM), see chapters 3 and 4. Both the effects of device length and the temperature dependence on the current voltage characteristic, will be considered and comparison made with published experimental data. The experimental data were provided by A. Campbell and D. D. C. Bradley, University of Sheffield[1].

The DDM model can simulate a variety of transport mechanisms, such as injection dominated processes and bulk limited processes, which are outlined in chapters 2 and 3. Therefore, it is necessary to determine the required transport mechanisms appropriate for the simulated device structures. In addition, the parameter space for the numerical model is large; therefore, only published material parameters will be used in order to reduce the number of variables required in the fitting process.

This chapter will be organised as follows. Section 5.1 introduces the material parameters and device geometries considered. Section 5.2 examines the published experimental data and suggested transport mechanisms. Section 5.3 discusses the fitting method used and the numerical simulations for both device geometries. Section 5.4 summarises the chapter and discusses problems with the numerical results.

5.1 Material Parameters

Figure 5.1 shows both device geometries simulated. Both devices structures are fully bipolar (majority hole) and consist of a left hand side (LHS) aluminium (Al) electron injecting Schottky contact, a p-doped PPV emission layer and an indium-tin-oxide (ITO) hole injecting Schottky contact. The two device lengths considered are (a) 94nm and (b) 125nm.

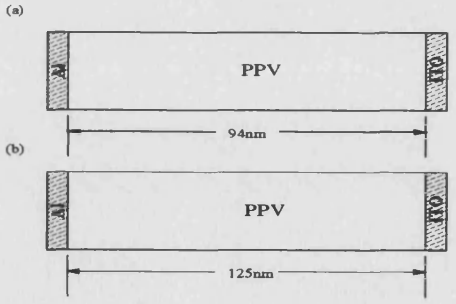

Figure 5.1: Geometry of the simulated OLEDs; (a) 94nm and (b) 125nm.

Table 5.2 lists the material parameter used in the device model, with a description of each term given in table 5.1. Where possible published PPV material parameters have been used[1] [3].

Material Parameter	Value	Units
A	$\approx 4\text{x}10^{-6}$	m^2
ϵ_s	≈ 3.0	-
N_c	$\approx 2\text{x}10^{26}$	m^{-3}
N_v	$\approx 2\text{x}10^{26}$	m^{-3}
N_A	$\approx 1\text{x}10^{22}$	m^{-3}
E_g	≈ 2.4	eV
$\phi_{Bn}(lhs)$	≈ 1.6	eV
$\phi_{Bp}(rhs)$	≈ 0.3	eV
χ_c	≈ 2.6	eV

Table 5.2: PPV material parameters.

5.2 Experimental Data and Transport Mechanisms

Assuming an ITO work function $\phi_{ITO} \approx 4.8$eV and a PPV ionisation potential of $I_P \approx 5.1$eV[1], then the barrier to hole injection at the ITO/PPV interface will be $\phi_{Bp} \approx 0.3$eV. Similarly, given an aluminium work function of $\phi_m \approx 4.2$eV and a PPV electron affinity of $\chi_c \approx 2.6$eV[1], the barrier to electron injection at the PPV/Al interface can be estimated to be $\phi_{Bn} \approx 1.6$eV. Estimates of the PPV/Al barrier height, using internal photoemission measurements, indicate that the barrier to electron injection is substantially lower and of the order $\phi_{Bn} \approx 0.7$eV[1]. The discrepancy in the barrier to electron injection may be attributed to interface layers and surface states [1]. Although the barrier to electron injection is much lower than the theoretical value of $\phi_{Bn} \approx 1.6$eV, it is still substantially higher than that of the barrier to hole injection at the ITO/PPV interface. In PPV materials the hole mobility is at least one order of magnitude greater than the electron mobility[2]. Therefore, hole carrier transport is expected to dominate in these devices.

Using these estimated barrier heights it is reasonable to expect that the device geometries shown in figure 5.1 will be dominated by injection limited transport. Numerical studies have indicated that space charge limited current (SCLC) will dominate where the barrier to injection is $\phi_B \ll 0.2$eV [3] [4]. Conversely contact limited injection, at low fields, is expected for $\phi_B \gg 0.3$eV and at high fields tunnelling[5] and SCLC is expected [6]. Results presented in chapter 4 indicated the importance of barrier height lowering and tunnelling transport mechanisms.

For small barriers to injection, both transport mechanisms tend to the SCLC limit in agreement with other numerical studies[3] [4].

Capacitance-voltage experiments, for the 125nm device, have shown no indication of the expected relationship in reverse bias between $1/C^2$ and V to indicate the presences of a depletion width. Studies of a 500nm ITO/PPV/Al structure have shown a depletion width of $W > 120$nm, which suggests that the acceptor dopant concentration will be $N_A < 10^{22}$ m^{-3}. Therefore, for both the 125nm and 94nm devices the depletion width will be greater than the device length at zero bias. This depleted rigid band approximation was used by I.D. Parker[5] to explain the current density-voltage dependence for various contact materials.

Figures 5.2 and 5.3 show the temperature dependence, of the experimental current-voltage (IV) characteristics, for the two device lengths considered. In both cases the IV curves can be seen to have four distinct regions of operation show schematically, in figure 5.4 together with depictions of the band structure in regions (a), (b) and (c).

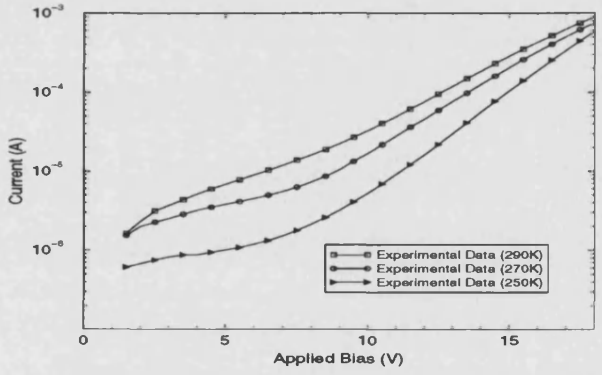

Figure 5.2: Experimental current voltage characteristic for the 125nm device for temperatures of 290K (□), 270K (∘) and 250K (▷) respectively

Referring to figure 5.4 and considering electrons only; then for an applied bias in the range $V_{app} < V'$, in region (a) electrons injected from the LHS contact see a potential barrier ψ_B, which corresponds to the built-in potential. Therefore, the IV curve corresponds to thermionic emission. As V_{app} tends to the built-in potential the barrier to thermionic emission decreases and the IV curve tends to a new gradient. In region (b) the current flow is dominated by the bulk material properties, where the gradient of the IV curve is due to the field dependence of the mobilities. The abrupt change in gradient at $V_{app} = V''$, corresponding to

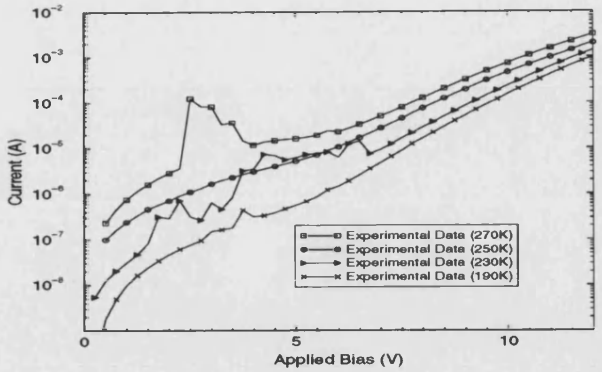

Figure 5.3: Experimental current voltage characteristic for the 94nm device for temperatures of 270K (□), 250K (○), 230K (▷) and 190K (×) respectively.

region (c), is due to the onset of tunnelling. In region (d), the injected carrier concentration approaches the space charge limit of the device at $V_{app} > V'''$.

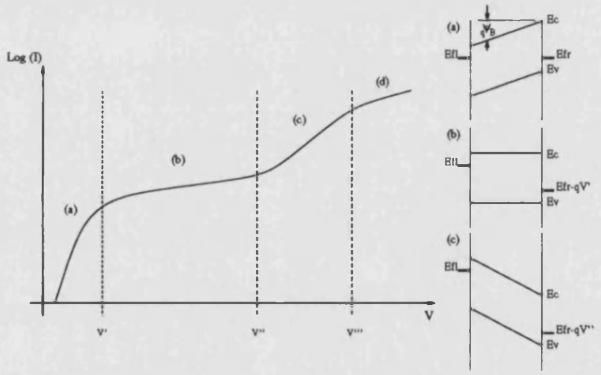

Figure 5.4: Schematic representation of the current-voltage curve, showing the four characteristic regions (a), (b), (c) and (d) together with a representation of the band diagram for regions (a), (b) and (c).

In chapter 4 results were presented for a dual Schottky contact, single layer device, based on the PPV organic material. These IV characteristics demonstrated several transport mechanisms; including thermionic emission diffusion, barrier height lowering and field emission. These results will be presented again here with a view to determining the appropriate transport mechanisms for the device geometries shown in figures 5.1a and 5.1b. Figures 5.5a 5.5b shows these current-density voltage characteristics.

Comparing the above curves with the experimental current voltage characteristics indicates that the most appropriate numerical model is thermionic emission

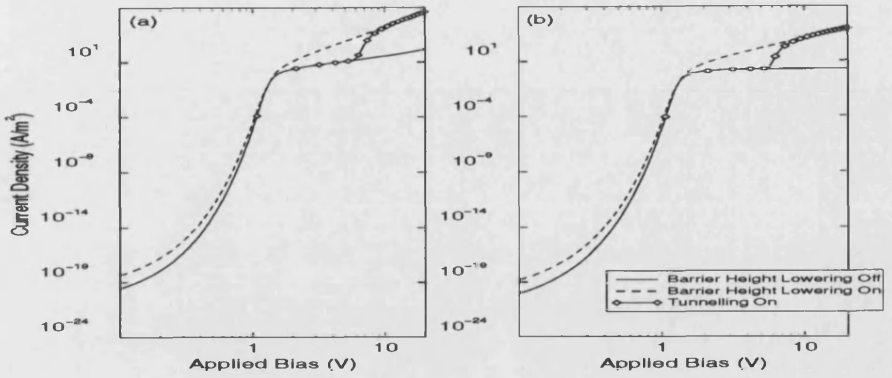

Figure 5.5: Predicted current-density voltage characteristics showing: thermionic emission diffusion (TED) (-), TED with barrier height lowering (–) and TED with Fowler Nordheim field emission (∘). Panel (a) shows the effect of field dependent mobilities and for panel (b) with fixed mobilities.

diffusion with Fowler Nordheim field emission. The experimental IV characteristics show a field dependence, region (b), for both the 94nm and 125nm device structures. This field dependence is clearly varying with device temperature. In the 94nm device case the gradient in region (b) is seen to increase with decreasing temperature, conversely the 125nm device shows a decreasing gradient with decreasing temperature.

5.3 Device Simulations

In this section a variety of numerical simulation results will be presented for the 125nm and 94nm experimental data. The experimental data is shown in figures 5.2 and 5.3 with the possible transports mechanisms, for these data, discussed in section 5.2. The fixed material parameters, used for both device lengths, are tabulated in table 5.2.

From the suggested transport mechanisms, thermionic emission and tunnelling, there are several material parameters that have to be determined. These are:

1. The left hand side (LHS) barrier to electron injection (ϕ_{Bn});
2. The right hand side (RHS) barrier to hole injection (ϕ_{Bp});

3. The field dependence parameter (E_0);
4. The zero field electron mobility (μ_{n0});
5. The zero field hole mobility (μ_{p0});
6. The tunnelling pre-factor (α_1).

These parameters introduce a considerable degree of freedom in the modelling and fitting process and in principle are dependent upon the simulation temperature[7] [8]. To simplify the parameter space two assumptions were made; ϕ_{Bn} remains fixed for all simulation temperatures, and $\mu_{n0} = 0.1\mu_{p0}$. These assumptions can be justified by the fact that the barrier to hole injection will dominate the current-voltage characteristic. Therefore, injected electrons are not expected to substantially affect the device operation.

5.3.1 Fitting Method

Several different approaches were used in modelling the two device lengths. Initially the 125nm device was considered and values of E_0, μ_{p0}, ϕ_{Bn} and ϕ_{Bp} used to fit the low voltage experimental data at T=290K ($V_{app} < 6V$). The high voltage ($V_{app} > 9V$) IV data was then fitted using the tunnelling pre-factor α_1. This parameter set was then used as a fixed reference for fitting attempts at lower temperatures. The approaches used to fit the remaining device temperatures were:

Approach 1. All material parameters held constant for remaining simulation temperatures;

Approach 2. Tunnelling pre-factor adjusted for optimum fit for the high voltage experimental data;

Approach 3. E_0, μ_{p0}, ϕ_{Bp} and α_1 adjusted for best fit to IV curve for all simulated temperatures.

For the 94nm device length the 270K experimental data were fitted using the same method as for the 125nm case. Then approaches 1-3 were used to fit the remaining temperatures.

5.3.2 125nm Device Results

Figure 5.6 shows the simulated IV curves at temperatures of 290K and 270K against the experimental data, using approach 1. The fit at 290K is in excellent agreement across the entire IV characteristic. The numerical fit to 270K is however poor in the high voltage ($V_{app} > 9V$), tunnelling dominated region. The low voltage fit is also poor with the gradient in the thermionic emission region ($0.1V < V_{app} < 10V$) greater than the experimental data. The second approach to fitting the data involved the adjustment of the tunnelling pre-factor to improve the fit to the high voltage data. Simulation results for this approach are shown in figure 5.7. With this method the agreement at low voltages will be identical to approach 1, but the adjustment to α_1 achieves good agreement with the experiment data. At temperatures below 270K, the simulation results deviated substantially from the experimental data.

The parameters used to fit the experimental data for approach 1 are shown in table 5.3. For approach 2 the tunnelling pre-factor used was $\alpha_1 = 1.35\text{x}10^{-7}$.

Parameter	Simulation Temperature	Units
T	290 and 270	K
μ_{n0}	$1.1\text{x}10^{-12}$	$m^2/(Vs)$
μ_{p0}	$1.1\text{x}10^{-11}$	$m^2/(Vs)$
α_1	$1.7\text{x}10^{-7}$	-
ϕ_{Bn}	1.6	eV
ϕ_{Bp}	0.227	eV
E_0	$7\text{x}10^6$	V/m

Table 5.3: 125nm Device: parameter set used for fitting approach 1. For approach 2 the tunnelling pre-factor used was $\alpha_1 = 1.35\text{x}10^{-7}$.

Several papers have suggested a thermally activated hole mobility [7] [8] [9]. This is shown in equations (5.1) - (5.4), where Δ is the activation energy, E is the electric field, $\mu_{p0(E=0)}$ and B are weighting factors, and T_0 is a material dependent constant.

$$\mu_p = \mu_{p0} \exp\left(\lambda\sqrt{E}\right) \tag{5.1}$$

$$\mu_{p0} = \mu_{p0(E=0)} \exp\left(\frac{-\Delta}{k_B T}\right) \tag{5.2}$$

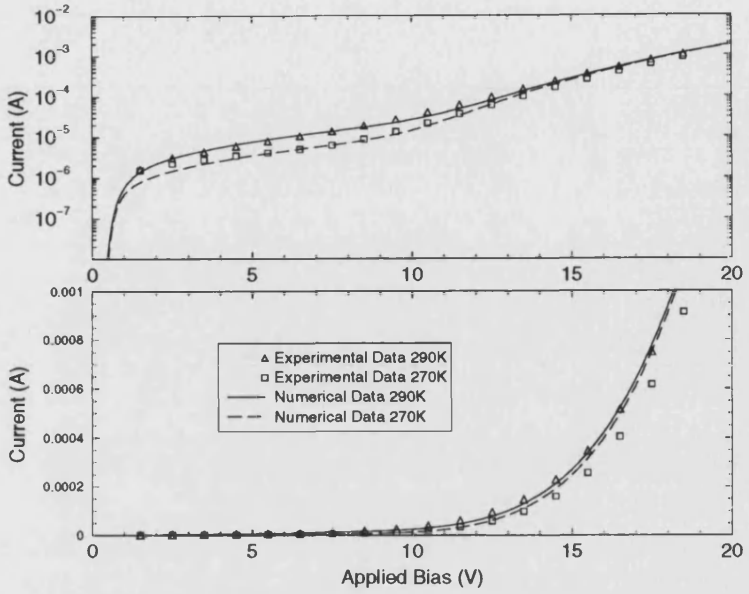

Figure 5.6: Comparison of the experimental data with the numerical simulation results for the 125nm device structures. Top panel plots data linear-log and bottom panel linear-linear. Simulation results for fitting approach 1 are shown for temperatures of 290K and 270K.

$$\lambda = B\left(\frac{1}{k_B T} - \frac{1}{k_B T_0}\right) \tag{5.3}$$

$$E_0 = \frac{1}{\lambda^2} \tag{5.4}$$

These equations affect the IV characteristic in two ways. As the simulation temperature decreases, μ_{p0} decreases, which results in a reduced current. In addition, the field dependence term E_0 affects the magnitude and gradient of the IV curve. Therefore, approach 3 allowed μ_{p0} and E_0 to decrease with temperature. As the current is decreased by the hole mobility, the barrier to hole injection has to be reduced in order to compensate. This decrease in barrier height has been observed experimentally; as the device temperature is lowered the emission spectrum is slightly red shifted corresponding to a decrease in the energy gap [7].

Figure 5.8 compares numerical approach 3 with the experimental data. The agreement at 270K in the high voltage, tunnelling regime, is again in good agreement. For the low voltage data the gradient of the IV characteristic is incorrect and slightly worse than the results obtain by fitting approach 2. Table 5.4 shows

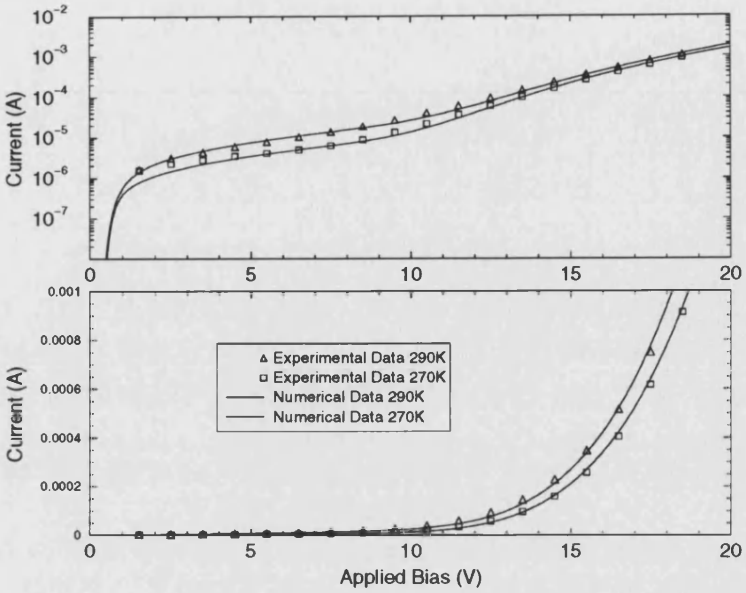

Figure 5.7: Comparison of the experimental data with the numerical simulation results for the 125nm device structures. Top panel plots data linear-log and bottom panel linear-linear. Simulation results for fitting approach 2 are shown for temperatures of 290K and 270K.

the material parameters used to fit the experimental data at temperatures of 290K and 270K.

Parameter	Simulation Temperature		Units
T	290	270	K
μ_{n0}	$1.1\text{x}10^{-12}$	$6\text{x}10^{-13}$	$m^2/(Vs)$
μ_{p0}	$1.1\text{x}10^{-11}$	$6\text{x}10^{-12}$	$m^2/(Vs)$
α_1	$1.7\text{x}10^{-7}$	$1\text{x}10^{-7}$	-
ϕ_{Bn}	1.6	1.6	eV
ϕ_{Bp}	0.227	0.221	eV
E_0	$7\text{x}10^6$	$5\text{x}10^6$	V/m

Table 5.4: 125nm Device: field and temperature dependent mobilities used for fitting approach 3.

It was observed in section 5.2 that the 125nm experimental data had a decreasing gradient with temperature for low voltages and an increasing gradient for high voltages. This behaviour is at odds with the previously described thermally activated hole mobility model. Therefore, in an attempt to improve the fit to the low voltage experimental data, it was assumed that as the temperature decreased E_0 increased; additionally the hole mobility was increased to compensate for the reduced current flow caused by the decrease in field dependence.

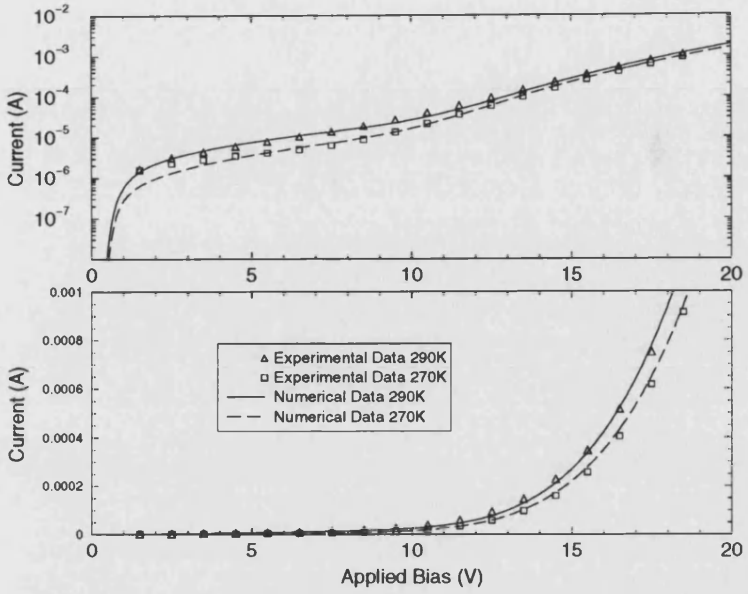

Figure 5.8: Comparison of the experimental data with the numerical simulation results for the 125nm device structures. Top panel plots data linear-log and bottom panel linear-linear. Simulation results for fitting approach 3 are shown for temperatures of 290K and 270K.

Table 5.5 lists the parameters used to fit the experimental data at temperatures of 290K, 270K and 250K. Figure 5.9 shows the fit to the experimental data. It can be seen that the fit, at low fields, to 290K, 270K and 250K is substantially improved when compared with the previous approaches. However, at the onset of tunnelling the fit to the data at 270K and 250K is poor. Additionally the gradient of the IV curve is too low in the space charge limit for 250K.

Parameter	Simulation Temperature			Units
T	290	270	250	K
μ_{n0}	$1.1\text{x}10^{-12}$	$1.9\text{x}10^{-12}$	$3.5\text{x}10^{-12}$	$m^2/(Vs)$
μ_{p0}	$1.1\text{x}10^{-11}$	$1.9\text{x}10^{-11}$	$3.5\text{x}10^{-11}$	$m^2/(Vs)$
α_1	$1.7\text{x}10^{-7}$	$1.3\text{x}10^{-7}$	$1.3\text{x}10^{-7}$	-
ϕ_{Bn}	1.6	1.6	1.6	eV
ϕ_{Bp}	0.227	0.221	0.221	eV
E_0	$7\text{x}10^6$	$1.4\text{x}10^7$	$4\text{x}10^7$	V/m

Table 5.5: 125nm Device: inverse relationship.

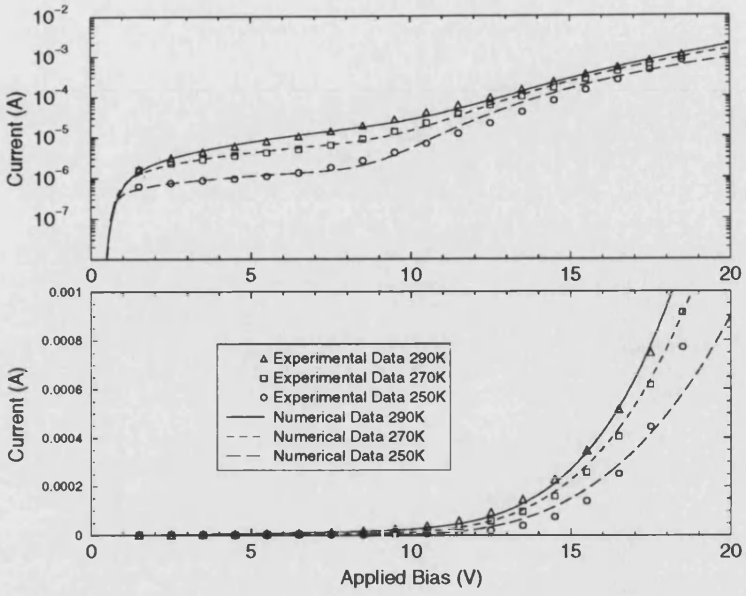

Figure 5.9: Comparison of the experimental data with the numerical simulation results for the 125nm device structures. Top panel plots data linear-log and bottom panel linear-linear. Simulation results for fitting approach 4 are shown for temperatures of 290K, 270K and 250K.

5.3.3 94nm Device Results

For the 94nm device length, the simulation method was identical to approaches 1-3 used to model the 125nm device length. The 94nm experimental data showed a clear field dependence in accordance with equations (5.1) - (5.4).

Table 5.6 shows the material parameters used in approach 1, with figure 5.10 showing the simulation results for temperatures of 270K and 250K. These results show a similar behaviour to the 125nm device structure, with good agreement at 270K for the entire IV characteristic. The 250K results are in poor agreement at high voltages ($V_{app} > 7V$) and the IV gradient, at low voltages ($V_{app} < 7V$), is lower than that of experimental data.

Figure 5.11 shows the effect of adjusting the tunnelling pre-factor to improve the fit to the high voltage data at 250K, 230K and 190K, where $\alpha_1 = 0.8\text{x}10^{-6}$, $\alpha_1 = 0.5\text{x}10^{-6}$, $\alpha_1 = 0.3\text{x}10^{-6}$ respectively. This achieved good agreement at high voltages for simulation temperatures of 250K and 230K. The result at 190K showed a significant deviation from the experimental data across the entire IV characteristic. For low voltages, the gradient of the experimental IV characteristic

increased with decreasing temperature which resulted in a poor numerical fit due to the fixed field dependence.

Parameter	Simulation Temperature	Units
T	270 and 250	K
μ_{n0}	$6x10^{-12}$	$m^2/(Vs)$
μ_{p0}	$6x10^{-11}$	$m^2/(Vs)$
α_1	$1.2x10^{-6}$	-
ϕ_{Bn}	1.8	eV
ϕ_{Bp}	0.224	eV
E_0	$3x10^6$	V/m

Table 5.6: 94nm Device: parameter set used for fitting approach 1.

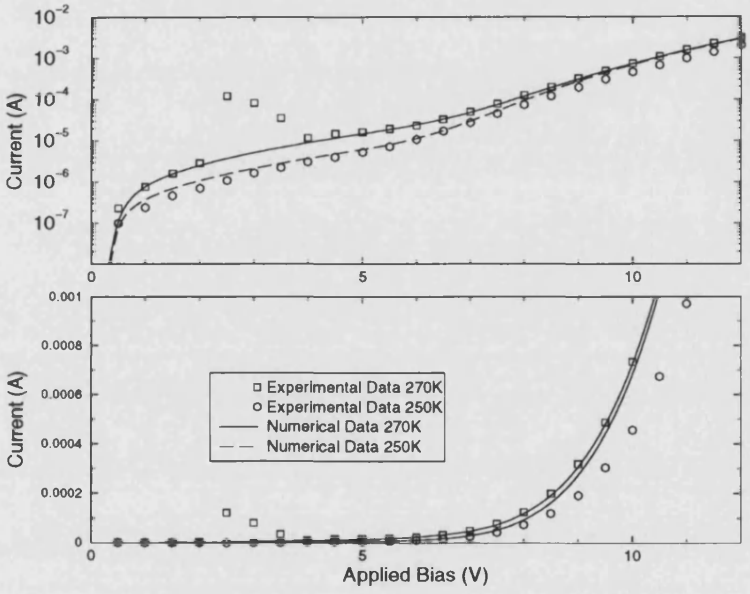

Figure 5.10: Comparison of the experimental data with the numerical simulation results for the 94nm device structures. Top panel plots data linear-log and bottom panel linear-linear. Simulation results for fitting approach 1 are shown for temperatures of 270K and 250K.

Figure 5.12 shows the simulation results for the thermally activated hole mobility model, with the parameters given in table 5.7. These results show good agreement for all simulation temperatures at low voltages. The high voltage data is also in good agreement for simulation temperatures of 270K, 250K and 230K. However, the 190K results deviated from the experimental data for $V_{app} > 11V$. At temperatures below 230K, the thermally activated hole mobility model appeared to break down with the hole mobility pinned at $\mu_{p0} \approx 8x10^{-13}m^2/(Vs)$. This behaviour has been reported in poly[methoxy (ethyl-hexyloxy) phenylene vinylene] MEHPPV [7].

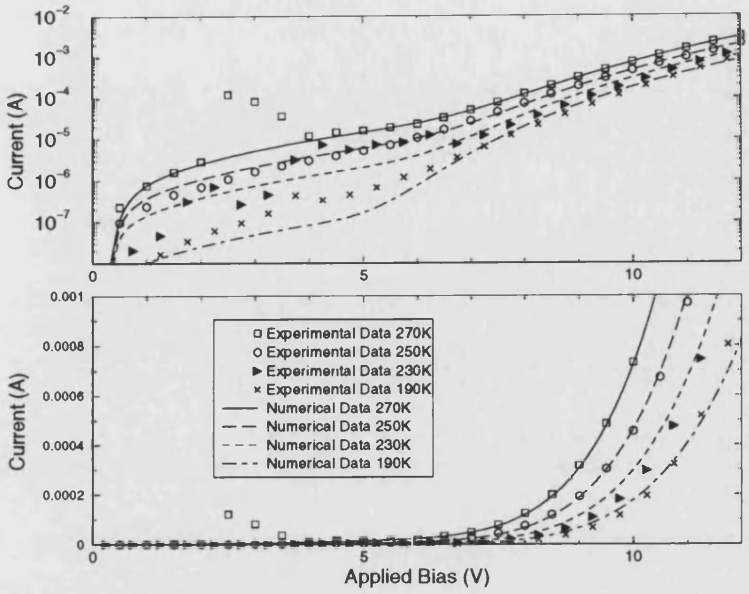

Figure 5.11: Comparison of the experimental data with the numerical simulation results for the 94nm device structures. Top panel plots data linear-log and bottom panel linear-linear. Simulation results for fitting approach 2 are shown for temperatures of 270K, 250K, 230K and 190K.

Parameter	Simulation Temperature				Units
T	270	250	230	190	K
μ_{n0}	$6x10^{-12}$	$2.8x10^{-13}$	$9x10^{-14}$	$8x10^{-14}$	$m^2/(Vs)$
μ_{p0}	$6x10^{-11}$	$2.8x10^{-12}$	$9x10^{-13}$	$8x10^{-13}$	$m^2/(Vs)$
α_1	$1.2x10^{-6}$	$6.5x10^{-7}$	$3.1x10^{-7}$	$1.8x10^{-7}$	-
ϕ_{Bn}	1.8	1.8	1.8	1.8	eV
ϕ_{Bp}	0.224	0.221	0.218	0.214	eV
E_0	$3x10^6$	$2.4x10^6$	$1.7x10^6$	$1x10^6$	V/m

Table 5.7: 94nm Device: field and temperature dependent mobilitiesusing fitting approach 3.

Figure 5.13 upper panel, plots the temperature dependence of the zero field hole mobility parameter μ_{p0} for the simulated temperatures. The lower panel shows the temperature dependence of the E_0 parameter for the simulated temperatures. Although there are only 4 numerical data points for the 94nm device length and 2 for the 125nm device structure. It is possible to fit equations (5.1) and (5.4) to these data points. The parameter values for these fits are shown in table 5.8.

The fitted values for Δ and $\mu_{p0(E=0)}$ differ from published experimental values for PPV and MEHPPV [7] [8] [9]. These parameters are reproduced in table 5.9. The fitted activation energy (Δ) is smaller than published parameters for PPV. As

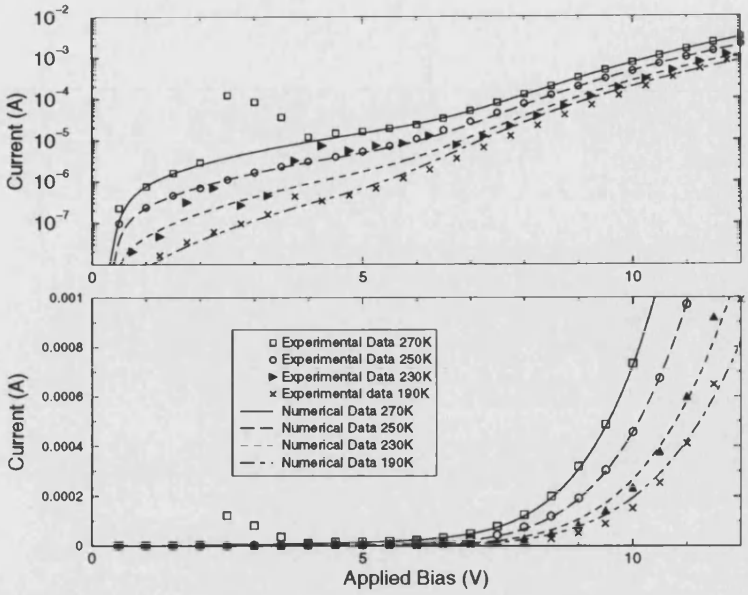

Figure 5.12: Comparison of the experimental data with the numerical simulation results for the 94nm device structures. Top panel plots data linear-log and bottom panel linear-linear. Simulation results for fitting approach 3 are shown for temperatures of 270K, 250K, 230K and 190K.

Parameter	125nm Device	94nm Device	Units
$\mu_{p0(E=0)}$	$7\text{x}10^{-7}$	$7\text{x}10^{-7}$	$m^2/(Vs)$
B	$2.9\text{x}10^{-5}$	$2.9\text{x}10^{-5}$	$eV(m/V)^{\frac{1}{2}}$
T_0	490K	430K	K
Δ	0.22	0.22	eV

Table 5.8: Hole mobility and field dependence for the 125nm and 94nm device structures for fitting approach 3.

Δ is associated with the structural disorder in the device, it would suggest that the simulated device structures are more ordered. Comparison of my simulated data, with published parameters, is complicated by the amorphous nature of the material and the synthesis and purity of the manufactured devices. The limited number of numerical points used in the fits together with the variability of the device structures make any comparisons with published data difficult. However, the 94nm device results indicated that the thermally activated hole mobility model is plausible.

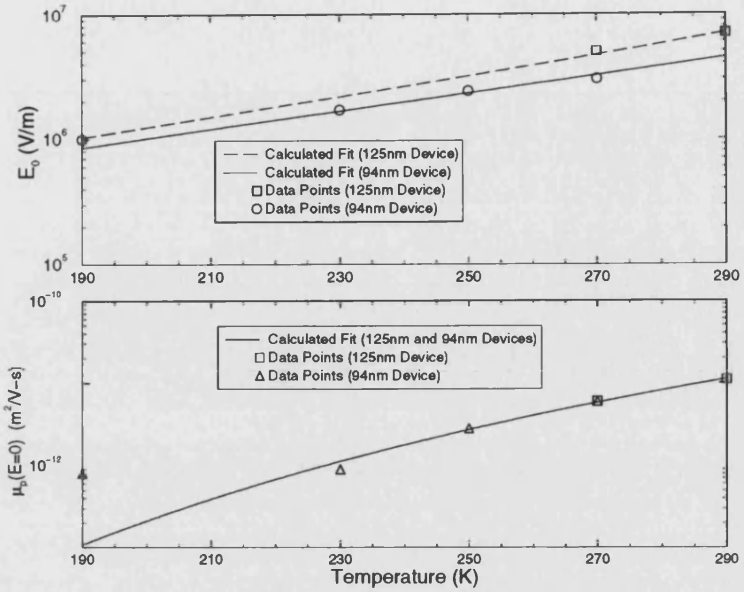

Figure 5.13: Top panel: Shows the dependence of E_0 on temperature for both the 94nm (○) and 125nm (□) device lengths. The dashed line and solid line show the fits to the numerical parameters using equation (5.4) for the 125nm and 94nm device lengths. Bottom Panel: Shows the dependence of μ_{p0} for the 125nm (□) and 94nm (△) device lengths. The solid line show the fit to the numerical parameters using equation (5.1) for both device lengths.

Parameter	PPV (SCLC)	MEHPPV from p-xylene (SCLC)	MEHPPV from chlorobenzene, (ILC)	Units
$\mu_{p0(E=0)}$	0.17, 3.5x10^{-3}	1.5x10^{-5}	15x10^{3}	$m^2/(Vs)$
B	3.1x10^{-5}, 2.9x10^{-5}	2.3 ± 0.2x10^{-5}	5.5x10^{-5}	$eV(m/V)^{\frac{1}{2}}$
T_0	540, 520-600	600 $\pm$90	300	K
Δ	0.59, 0.48	0.38 $\pm$0.02	0.75	eV

Table 5.9: Published thermally activated hole mobility parameter[7].

5.4 Conclusions

In this chapter two PPV device structures have been modelled. The main emphasis of this chapter was to achieve agreement with experimental data over a wide range of operating temperatures. The transport mechanisms for the experimental data were suggested and implemented in the numerical model. Several different approaches were used to fit this data with the best results obtained for the 94nm device using a thermally activated hole mobility.

The 125nm device structure proved more difficult to model. The experimental

data indicated that the hole mobility had two distinct regions of operation. At low fields, the field dependence reduced with decreased simulation temperatures, and for high fields increased with decreasing temperature. This behaviour is not predicted by the thermally activated hole mobility model, which proved successful for the 94nm device structure.

The deviation of the 125nm device structure from the activated hole mobility model is difficult to understand as this method proved successful for the 94nm device. Monte Carlo simulations have shown that off-diagonal disorder causes the mobility to decrease at low fields before becoming subject to a $\log(\mu) \propto E^{\frac{1}{2}}$ at high fields [10]. Therefore, an explanation for the length dependence of these devices may be due to the field strength, as the 125nm device will be subject to a lower field than the 94nm device ($E \approx V_{app}/L$).

It was possible to fit the numerical mobility and field dependence parameters to the thermally activated hole mobility equations. A comparison was made to published parameters, but due to the amorphous nature of the PPV material and possibility of differing synthesis routes used in manufacturing device structures, made comparison difficult. The devices studied in this chapter had an activation energy of $\Delta \approx 0.22$eV which suggests a high degree of order.

There are, however a number of physical problems with the results presented in this chapter, concerning the tunnelling pre-factor α_1. The value of α_1 varied by one order of magnitude as L varies from 94nm to 125nm, while it should be independent of device thickness. It also α_1 varies with device temperature, whilst the Fowler Nordheim equation predicts only a small temperature dependence of the form[1],

$$J_{FN}(T)/(J_{FN}(0) \approx 1 + 1/6\,(\pi c_1 k_B T)^2\,. \tag{5.5}$$

Another possible explanation for the high voltage behaviour has been proposed. This theory suggests the presence of an exponential or Gaussian distribution of hole traps [1], although the experimental evidence for trapping indicates a single trap energy level 0.8eV above the valence band edge[11]. The presence of electron traps has also been suggested, in electron only devices [2] but as the transport in these devices is hole dominated, electron trapping has no effect upon the IV

characteristic.

The most significant problem encountered in modelling these device structures is the number of ill-defined parameters that can significantly affect the device behaviour. Additionally, the material properties appear to be dependent upon the purity and synthesis route used in manufacturing the experimental devices. These problems make device performance and transport prediction very difficult without first studying experimental device data.

References

[1] A. J. Campbell, D. D. C. Bradley and D. G. Lidzey, *Journal of Applied Physics*, **82**, 6326-6342, 1997.

[2] P. W. M. Blom, M. J. M. Vleggaar, *Applied Physics Letters*, **68**, 3308-3310, 1996.

[3] P. S. Davids, I. H. Campbell and D. L. Smith, *Journal of Applied Physics*, **82**, 6319-6325, 1997.

[4] I. H. Campbell, P. S. Davids and D. L. Smith, *Applied Physics Letters*, **72**, 1863-1865, 1998.

[5] I. D. Parker, *Journal of Applied Physics*, **75**, 1656-1666, 1993.

[6] Y. Kawabe, M. M. Morrell, G. E. Jabbour, S. E. Shaheen, B. Kippelen and N. Peyghambarian, *Journal of Applied Physics*, **84**, 5306-5314, 1998.

[7] J. M. Lupton and I. D. W. Samuel, *Journal of Physics D: Applied Physics*, **32**, 2973-2984, 1999.

[8] P. W. M. Blom, M. J. M. de Jong and S. Breedijk, *Applied Physics Letters*, **71**, 930-932, 1997.

[9] P. W. M. Blom, M. J. M. de Jong and M. G. van Munster, *Physical Review B*, **55**, R656-R659, 1997.

[10] P. M. Borsenberger, L. Pautmeier and H. Bässler, *Journal of Chemical Physics*, **94**, 5447-5454, 1990.

[11] A. Campbell and D. D. C. Bradley, University of Sheffield, *private communication*, 1999.

Chapter 6

OLED Performance Optimisation

In chapter 5 simulation results were presented for single layer OLEDs based on the organic material PPV. Comparisons were made to the experimental current-voltage (IV) characteristics, and good agreement achieved over a wide temperature and voltage range, using thermionic emission and Fowler Nordheim tunnelling. These simulation showed that the device geometries were dominated by positive carriers. Subsequently the optical recombination magnitude was low, as was device efficency. Several problems were encounted when fitting the tunnelling portion of the current-voltage characteristic to the experimental data. The tunnelling pre-factor (α_1) changed with both the device length and the simulation temperature. This made device prediction difficult, as experimental data were required to determine the position of the tunnelling dominated region of the IV characteristic. Therefore, in this chapter systems will be considered where tunnelling is not important.

In this chapter several device geometries will be investigated, in order to determine the best device structure regarding optical recombination position and strength versus the current density. Device length, carrier mobilities, barriers to injection and carrier trapping have been suggested as important in governing OLED performance [1][2][3][4]. Therefore, carrier mobilities and barriers to injection will be investigated in order to achieve balanced injection so as to maximise carrier recombination. Carrier trapping will also be investigated to determine its effect on the device performance.

This chapter will be organised as follows. In section 6.1 the organic material and device geometries to be studied will be detailed. In section 6.2 simulation results will be presented for single layer OLEDs, and in section 6.3 a heterostructure device will be used to optimise the optical recombination strength.

6.1 Device Information

The device geometries considered in this chapter are shown in figures 6.1a and 6.1b. Device (a) consists of a left hand side (LHS) electron injecting Schottky contact, a polymer emission layer based on poly(methoxy (ethyl-hexyloxy) phenylene vinylene) (MEHPPV) and a right hand side (RHS) hole injecting Schottky contact. Three device length will be considered L=100nm, L=150nm and L=200nm.

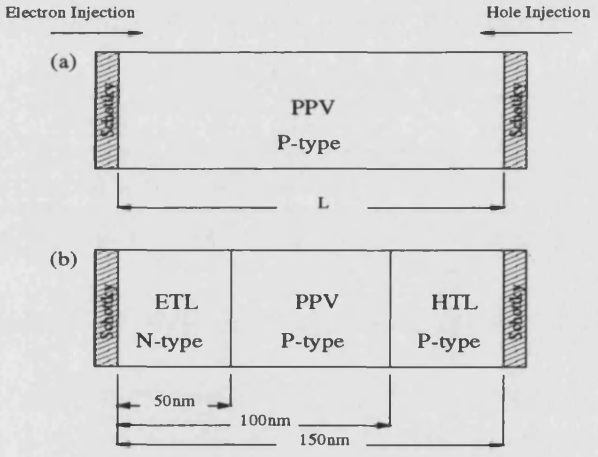

Figure 6.1: Simulated device geometries. For device (a) the lengths studies are L=100nm, L=150nm and L=200nm.

For the single layer structure, two contact types will be considered. Type (a) consists of a symmetric system where both barriers to injection are ohmic ($q\phi_{Bn} = q\phi_{Bp} = 0.2$eV). Type (b) consist of a contact limited barrier to electron injection at the LHS ($q\phi_{Bn} = 0.6$eV) and a ohmic hole injecting RHS contact ($q\phi_{Bp} = 0.2$eV). Two sets of zero field mobilities will be considered, low and high μ_{n0} and low and high μ_{p0}. These parameters are listed in table 6.1 with the material parameters used for device (a) given in table 6.2.

Device (b) consists of a LHS electron injecting Schottky contact, a electron transport layer (ETL), a MEHPPV based emission layer, a hole transport layer (HTL)

Mobility	Value	Units
μ_0	$1x10^{-10}$	$m^2/(Vs)$
low $\mu_n 0$	$0.01\mu_0$	$m^2/(Vs)$
high $\mu_n 0$	μ_0	$m^2/(Vs)$
low $\mu_p 0$	$0.01\mu_0$	$m^2/(Vs)$
high $\mu_p 0$	μ_0	$m^2/(Vs)$

Table 6.1: Zero field hole and electron mobilities used in the numerical model.

Parameters	Value	Units
ϵ_0	3.0	-
E_g	2.4	eV
χ_c	2.0	eV
N_c	$1x10^{24}$	m^{-3}
N_c	$1x10^{24}$	m^{-3}
N_d	0	m^{-3}
E_0	$1x10^7$	V/m
E_{t1}	1.7	eV
P_{t1}	$1x10^{22}$	m^{-3}
g	1.0	-

Table 6.2: MEHPPV material parameters for the emission layer in devices (a) and (b).

and a RHS Schottky contact. The material parameters used in emission layer are shown in table 6.2. The parameters used for the ETL and HTL layers are given in table 6.3.

Parameters	ETL	HTL	Units
ϵ_0	3.0	3.0	-
E_g	3.1	2.0	eV
χ_c	1.6	1.5	eV
N_c	$1x10^{24}$	$1x10^{24}$	m^{-3}
N_c	$1x10^{24}$	$1x10^{24}$	m^{-3}
N_{DOP}	$N_d = 5x10^{23}$	$N_a = 5x10^{23}$	m^{-3}
E_0	$1x10^7$	$1x10^7$	V/m
E_{t1}	1.7	1.7	eV
P_{t1}	1.0	1.0	m^{-3}
g	1.0	1.0	-

Table 6.3: MEHPPV material parameters for the electron and hole transport layers used in devices (b).

6.1.1 Transport Mechanisms

The transport mechanisms considered in this chapter will be thermionic emission diffusion with barrier height lowering. Hole trapping will also be considered to investigate its effect upon device efficency. Fowler Nordheim tunnelling will be neglected for these devices, due to the previously outlined problems associated with the tunnelling pre-factor α_1.

The justification for ignoring tunnelling can, to some extent, be found by observing the behaviour of the IV characteristic as the barrier to hole injection is reduced. This is shown in figure 6.2 for a 100nm single layer device. The barrier to electron injection at the LHS is fixed at 0.6eV. The barrier to hole injection at the RHS is varied from 0.6eV down to 0.1eV.

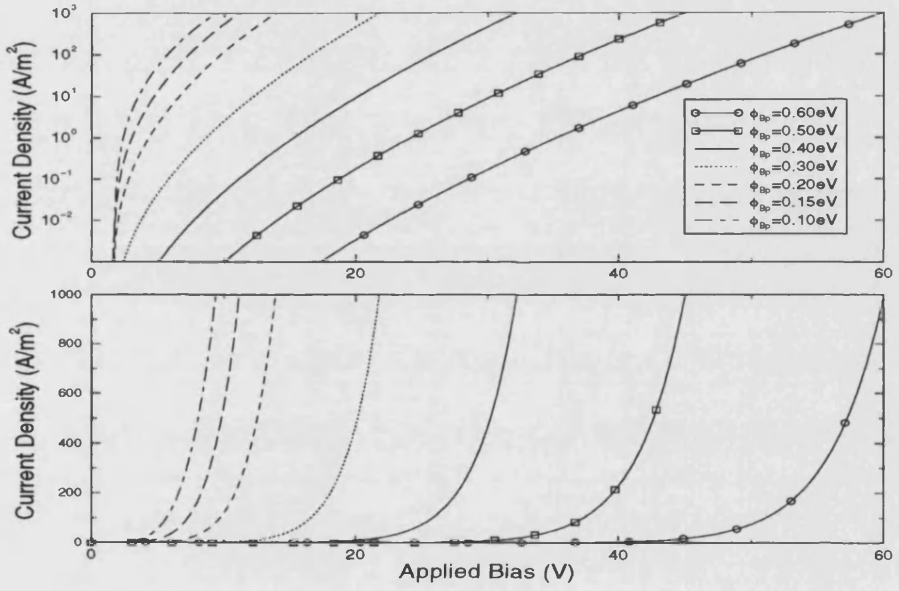

Figure 6.2: Current-density voltage (JV) characteristics for a single layer MEHPPV based organic device, for various barriers to hole injection. The figure shows the transition of the JV characteristic from a contact limited (0.3eV $< \phi_{Bp} <$ 0.6eV) to a space charge limited (0.1eV $< \phi_{Bp} <$ 0.3eV) current. Top panel shows the JV characteristics log -linear and the bottom panel shows the JV characteristics linear-linear.

Referring to figure 6.2, as the barrier to hole injection reduces the dominant transport mechanism switches from a contact limited current (0.3eV $< \phi_{Bp} <$ 0.6eV) to a space charge limited current (0.1eV $< \phi_{Bp} <$ 0.2eV). In chapter 4 it was shown for a similar device structure that for sufficiently high biases the IV characteristics saturated to the space charge limit. For the case where only

barrier height lowering was considered, the IV curve tended to the space charge limited in agreement with Fowler Nordheim tunnelling for high biases. These results are presented again here for completeness, see figure 6.3.

Results published by Crone *et al* [1] and Lupton *et al* [5] showed a similar behaviour for a single layer hole only device. The onset of space charge limited behaviour, in both cases, occurred at 0.3eV and showed a more pronounced transition, from a contact limited to a space charge limited current, due to the inclusion of tunnelling.

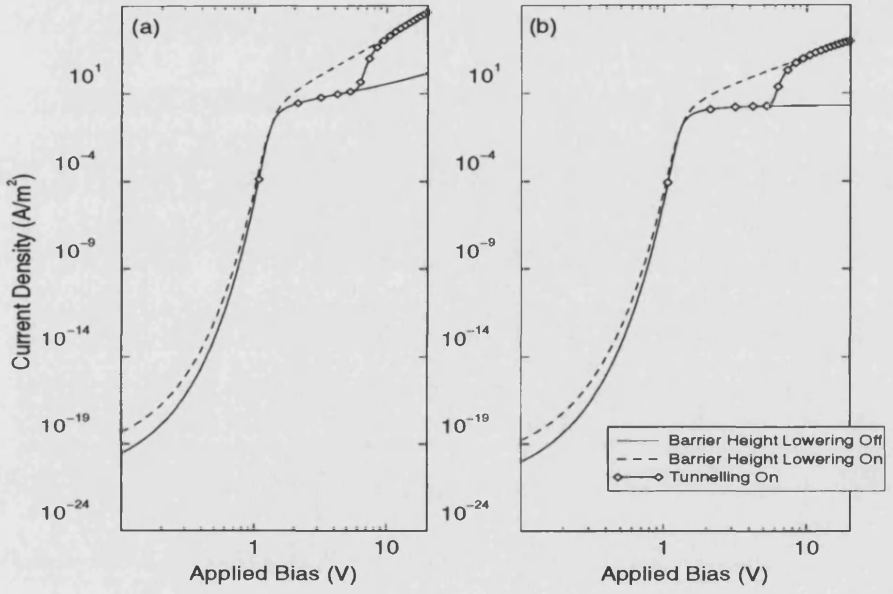

Figure 6.3: Example current-density voltage characteristics showing thermionic emission diffusion (TED) (-), TED with barrier height lowering (–) and TED with Fowler Nordheim field emission (o). Panel (a) shows the effect of a field dependent mobilities and panel (b) with field independent mobilities.

6.2 Single Layer Devices

In this section results will be presented showing the behaviour of geometry (a) for 3 device lengths: L=100nm, L=150nm and L=200nm. The zero field mobilities are shown in table 6.1. The barriers to carrier injection will also be considered. These are, balanced injection (type (a)) using ohmic contacts for both electron and hole injection. Contact limited injection (type (b)) using a ohmic contact for hole injection and a Schottky contact for electron injection. Hole trapping will

also be studied to determine its effect upon recombination strength and position in the device.

6.2.1 Trap Free Case

Figures 6.4 and 6.5 show the current-density voltage (JV) characteristics and recombination profiles for the 3 device lengths: panel (a) 100nm, panel (b) 150nm and panel(c) 200nm. Referring to figure 6.4 it can be seen that all the JV characteristics behave in a similar manner regardless of the device length. The effect of increasing the device length is to reduce the electric field strength, which in turn reduces the carrier mobilities and the magnitude of the current density. The primary effect, of the barrier to electron injection, is to determine the turn on position of the organic diode. This can be understood by considering the built-in potential; $V_{bi} \approx 2.0V$ for ohmic contacts and $V_{bi} \approx 1.6V$ for contact limited electron injection. However, the barriers to injection do not determine the high field ($V_{app} > 2V$) device behaviour. For all device lengths, the JV characteristics saturate to a space charge limited current that is dominated by the higher mobility carrier species.

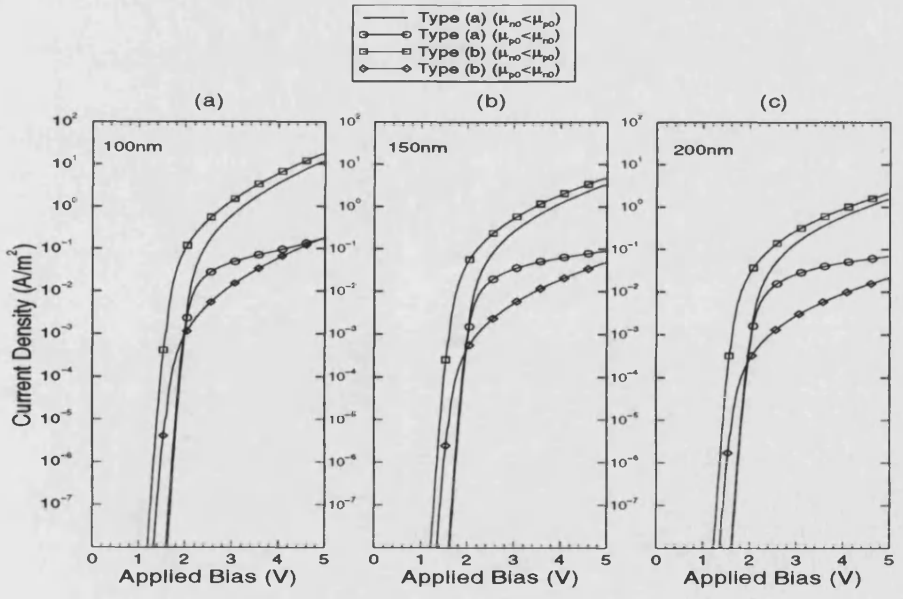

Figure 6.4: JV characteristics for (a) 100nm, (b) 150nm and (c) 200nm device lengths. Figure shows the effect of barriers to electron injection (ohmic or Schottky) and the effect of the electron (low μ_{n0} and high μ_{n0}) and hole (low μ_{p0} and high μ_{p0}) mobilities.

Although the barrier to electron injection plays a limited role in determining the JV characteristic, it does influence the recombination rate. Figure 6.5 shows the bimolecular recombination rate within device (a) for the 3 device lengths ($V_{app} = 5.0V$). As per figure 6.4 the device length seems only to effect the magnitude of the recombination rate. In the case of a contact limited barrier to electron injection fewer electrons are injected into the device when compared with the ohmic contact. Therefore, the magnitude of the optical recombination, is limited by the imbalance between the injected electron and hole densities.

The carrier mobilities affect the shape of the recombination profile. For $\mu_{n0} < \mu_{p0}$, the recombination profile is centred at the electron injecting LHS contact. Therefore the low electron mobility causes a buildup of carriers at the LHS contact. However, the hole density is spread more evenly through the device structure due to the higher hole mobility. This results in a recombination peak close to the electron injecting contact. Conversely for $\mu_{p0} < \mu_{n0}$, the recombination rate is flatter and distributed more evenly through the device structure. The low hole mobility should in principle have resulted in a recombination peak close to the hole injecting contact in an identical fashion to the low electron mobility case. This discrepancy can be understood by considering the effect of barrier height lowering, which only occurs at the RHS for high fields ($V_{app} > V_{bi}$). This results in a lower barrier to hole injection and increases the hole density. The higher electron mobility achieves an even distribution of electrons through the device structure, which when coupled with a larger hole injection rate, gives rise to a more balanced charge density profile and a flat recombination rate. As the device length is increased the effect of the low hole mobility causes a contact limited recombination rate at the RHS contact. This is seen clearly in panel (c) and to a lesser extent in panel (b) of figure 6.5.

6.2.2 Hole Trapping Case

The 100nm device length gave the best device performance, regarding recombination strength and position through the device. The 2 carrier mobility cases, for $\mu_{n0} < \mu_{p0}$ and $\mu_{p0} < \mu_{n0}$, together with ohmic contacts will now be investigated to determine the effect of a single energy level of hole traps. The trap energy level, density of traps and trap degeneracy are given in table 6.2.

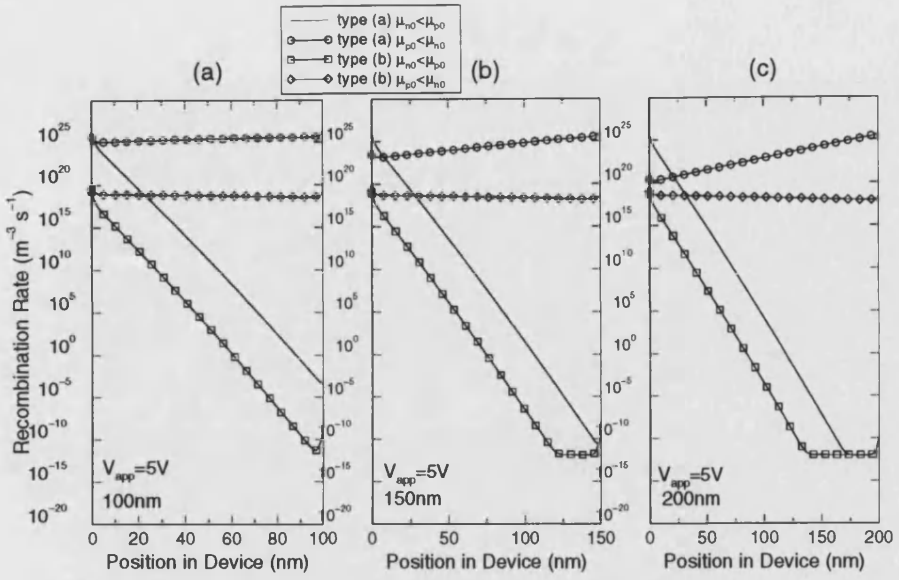

Figure 6.5: Recombination profiles through the device structure for (a) 100nm, (b) 150nm and (c) 200nm. Although the recombination profile appears constant for several of the plots, there is however a slight gradient present in all cases. Additionally the recombination rate varies rapidly at the contacts therefore the approximation $J = -qR_{OPT}L$ is not valid.

The recombination rate and JV characteristics for these two mobility cases are shown in figure 6.6 (top panel) and figure 6.6 (bottom panel) respectively. The band structure and carrier densities, for $V_{app} = 5$ and $V_{app} = 0V$, are shown in figures 6.7 (a)-(d) for $\mu_{n0} < \mu_{p0}$ and figures 6.8 (a)-(d) for $\mu_{p0} < \mu_{n0}$ respectively.

Referring to figure 6.6 (bottom panel) for the $\mu_{n0} < \mu_{p0}$ mobility case. The initial effect of the traps is to reduce the number of thermally free hole carriers which therefore reduces the current density. Under a high forward bias ($V_{app} > V_{bi}$) the current density saturates to a near ohmic gradient. As ϕ_{Bp} impinges on the hole trap energy level, the traps fill and the current-density switches to a new gradient the field dependent trap square law ($V_{app} \approx 3V$). Increasing the applied biases further causes the remaining traps to be filled and the gradient of the current-density changes to the field dependent trap free square law, as all injected carriers, now contribute to the current-density.

Figures 6.7(a)-(d), show the band structure and carrier densities for $V_{app} = 5V$ and $V_{app} = 0V$ respectively. At zero bias, the hole traps at the RHS are filled (80nm$< x <$100nm), which results in a slight band bending adjacent to the RHS

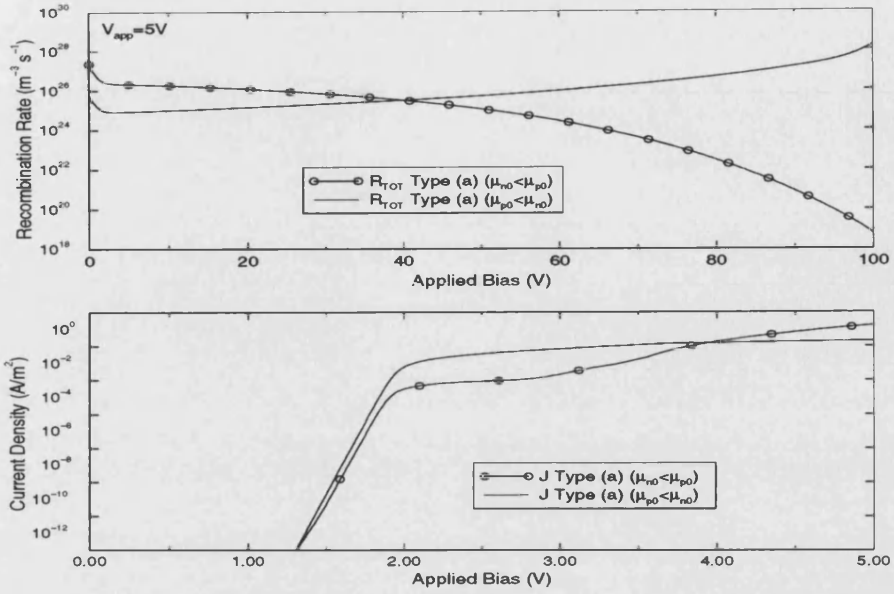

Figure 6.6: Recombination profiles (top panel) and JV characteristics (bottom panel) for the 100nm device structure showing the effect of hole trapping. Barriers to injection are ohmic and the 2 mobility cases considered are $\mu_{n0} < \mu_{p0}$ and $\mu_{p0} < \mu_{n0}$.

contact. The valence band bends upwards due to the positive space charge at the interface a per a n-type Schottky juction diode. This is shown clearly in figures 2.1a and 2.1b in chapter 2 section 2.1. For $V_{app} = 5V$, $q\phi_{Bp} < E_{t1}$ therefore all the hole traps are filled which causes the band bending across the entire structure. The electron density is still depleted at the RHS contact (see figure 6.7(b)), due to the low electron mobility. This gives rise to a recombination profile that is biased towards the electron injecting contact due to the low electron mobility. However, the introduction of hole traps has greatly improved the recombination profile, when compared with the trap free case, as it is no longer solely confined to the LHS contact. This can be attributed to a more even distribution of the electron density coupled with the reduced hole density due to trapping.

For the $\mu_{p0} < \mu_{n0}$ mobility case, the effect of hole traps on the JV characteristic is negligible, although the hole trapping process is virtually identical to the previously discussed $\mu_{n0} < \mu_{p0}$ mobility case. In this case, the device is dominated by the electron density, as hole trapping results in a hole density that is lower than the electron density. This is shown clearly in figure 6.8 (b). The recombination profile is virtually identical to the previously discussed trap free case, although it does shows a slight trend towards the RHS contact. This can be attributed to the low hole mobility.

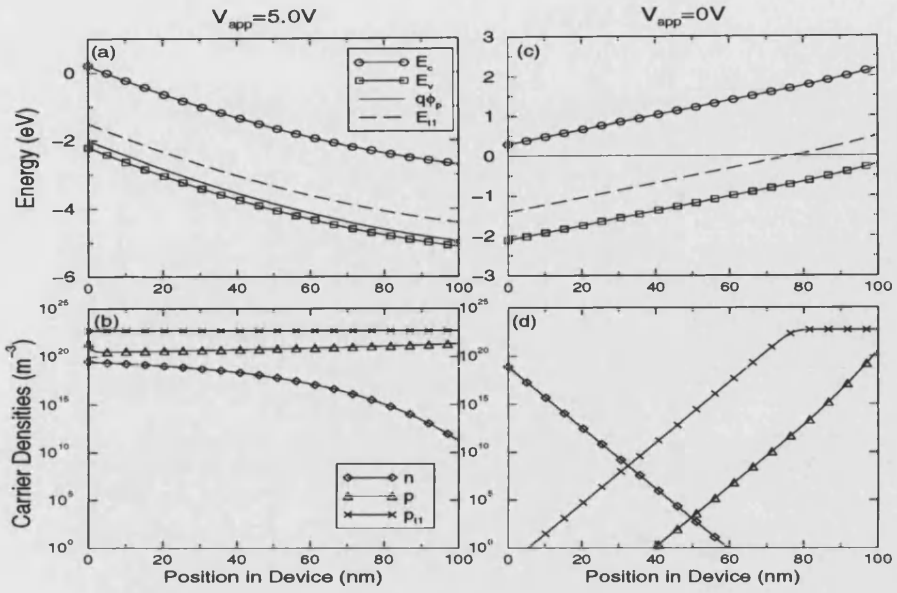

Figure 6.7: Corresponding graph to figure 6.6, showing the band structure and carrier densities at $V = 5V$ (panels (a) and (b)) and $V = 0V$ (panels (c) and (d)). The mobility model considered is $\mu_{n0} < \mu_{p0}$.

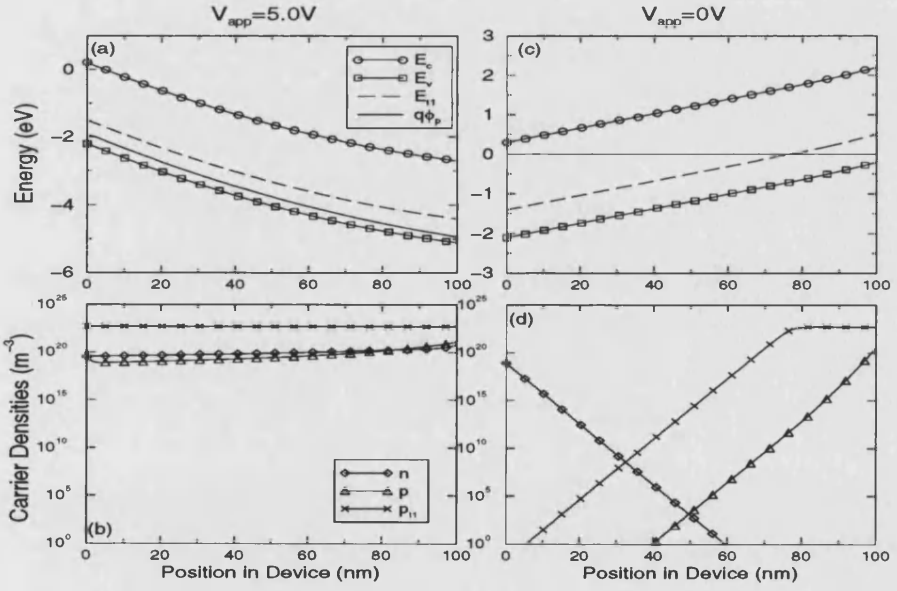

Figure 6.8: Corresponding graph to figure 6.6, showing the band structure and carrier densities at $V = 5V$ (panels (a) and (b)) and $V = 0V$ (panels (c) and (d)). The mobility model considered is $\mu_{p0} < \mu_{n0}$.

6.2.3 Optimised Single Layer Structure

The result presented so far have been aimed at understanding the effects of the carrier mobilities, barriers to injection and hole trapping on device behaviour.

However, the hole mobility is known to be at least 2 orders of magnitude greater than the electron mobility which limits the scope for improving single layer device performance. For the trap free case the recombination profile for $\mu_{n0} < \mu_{p0}$ peaked at the LHS electron injecting contact. This form of recombination is suspected as a cause of poor device efficiency due to dipole quenching of excitons at the metal cathode[1][6].

The best single layer device behaviour was found for $\mu_{p0} < \mu_{n0}$ as the high electron mobility produced an even recombination profile through the entire device. However, this case is not physically appropriate for organic materials based on PPV. A possible solution to the positional dependence of the recombination profile towards the LHS contact for low μ_{n0}, would be to increase the barrier to hole injection. As barrier height lowering only operates at the RHS for $V_{app} > V_{bi}$, it is reasonable to suspect that increasing the barrier to hole injection would act to reduce the injected hole density and thereby correct the imbalance in the carrier densities. Therefore, device simulation will be shown for the physically realistic mobility parameters $\mu_{n0} < \mu_{p0}$. In addition the barrier to hole injection will be increased to $q\phi_{Bp} = 0.3$eV in an attempt to balance the electron and hole densities.

Figure 6.9 shows the recombination profiles (top panel) and JV characteristics (bottom panel) for the realistic mobility case of ($\mu_{n0} < \mu_{p0}$). Both the trap free and the hole trapping cases are presented. Figures 6.10 show the band structure and carrier densities for the trap free case (panels (a) and (b)); the hole trapping case is shown in figure 6.10 (panels (c) and (d)). The effect of increasing the barrier to hole injection acts to balance the electron and hole densities improving the recombination profile through the device structure. For both the trap free and hole trapping case, the recombination rate is substantially improved over that of the ohmic hole injecting contact.

6.3 Heterostructure Device

The single layer structures discussed previously all had large recombination rates at one or both injecting contacts. Even the optimised device structure, whilst having an even recombination profile through the device, had large recombination

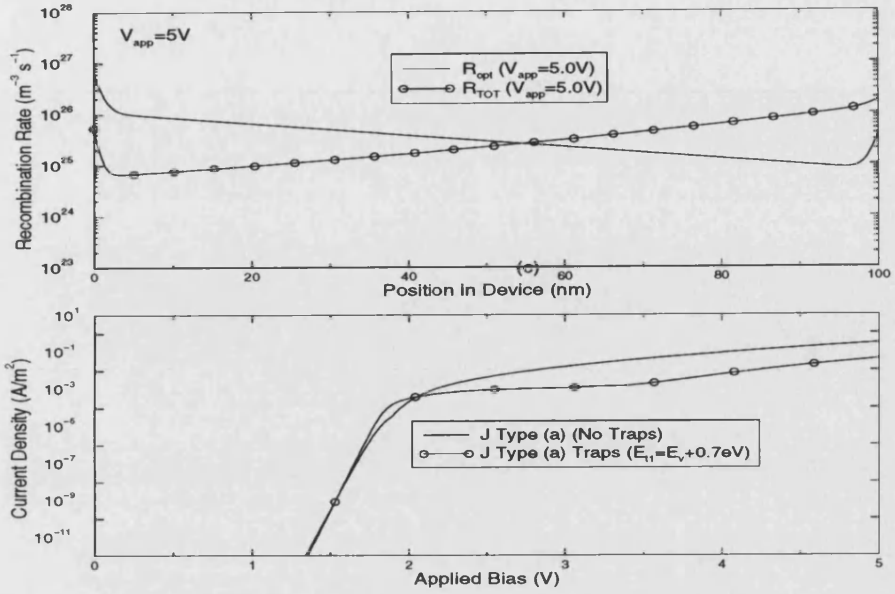

Figure 6.9: Optimised device structure ($\phi_{Bn} = 0.2$eV and $\phi_{Bp} = 0.3$eV) for realistic mobility model $\mu_{n0} < \mu_{p0}$. Top panel shows recombination profiles through device structure for trap free case (-) and hole trapping case (∘). Bottom panel shows JV characteristics for trap free case (-) and hole trapping case (∘).

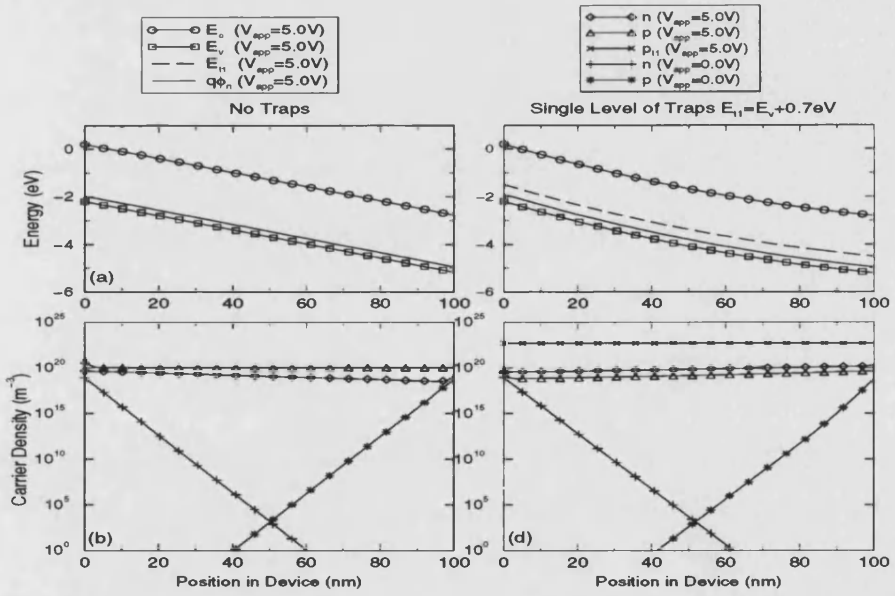

Figure 6.10: Corresponding graph to figure 6.9 showing band structure and carrier densities at $V_{app} = 5V$ for trap free case (panels (a) and (b)) and hole trapping case (panels (c) and (d)).

rates at the injecting contacts. In single layer structures there is no means of eliminating recombination at the metallic contacts. Therefore, it is impossible to

reduce dipole quenching effects that impair device efficiency.

In this section, a hypothetical 3 layer heterostructure will be used to achieve confinement of carriers in the MEHPPV emission layer. The device geometry is shown in figure 6.1b and consists of a LHS Schottky contact, an electron transport layer, a MEHPPV emission layer, a hole transport layer and a hole injecting Schottky contact. The basic device geometry is designed to transport injected carriers, via the appropriate transport layer, to the MEHPPV emission layer where they are confined. The ETL is therefore designed to transport electrons and block holes whereas, the HTL is designed to transport holes and block electrons. A possible candidate for the HTL is PPV. A possible ETL material could be (biphenylyl (tert-butylphenyl) oxadiazole) PBD[7].

The following assumptions have been made: $\mu_{n0} > \mu_{p0}$ for the ETL, and $\mu_{p0} > \mu_{n0}$ for the HTL, high doping in the ETL and HTL is appropriate, and carrier trapping is confined to the emission layer. Finally it is assumed that the conduction and valence band offsets can be chosen to maximise carrier confinement to the MEHPPV emission layer. The simulation model used is the same as for the single layer devices. The material parameters for the 3 layer heterostructure device are shown in tables 6.2 and 6.3.

Figure 6.11 shows the JV characteristics and recombination profiles for the trap free and hole trapping cases. The corresponding band structures and carrier densities are shown in figures 6.12 (a)-(d) and figures 6.13 (a)-(d) for the trap free case and hole trapping case respectively. From the recombination rate profiles it can be seen that carrier confinement has been achieved and recombination at the contacts eliminated. This is shown clearly in figure 6.12(d), for the trap free case and figure 6.13(d) for the hole trapping case. The magnitude of the recombination has been substantially increased over that of the optimised single layer device. In addition, the effect of hole trapping, in the MEHPPV emission layer, is minimal and only effects the distribution of the hole density through the emission layer.

This device structure is extreamly sensitive to the doping density of the two transport layers. If $N_{DOP} < 1\text{x}10^{23}$ (m^{-3}) then the device no longer acts to confine carriers in the emission layer and the recombination rate reduces substantially.

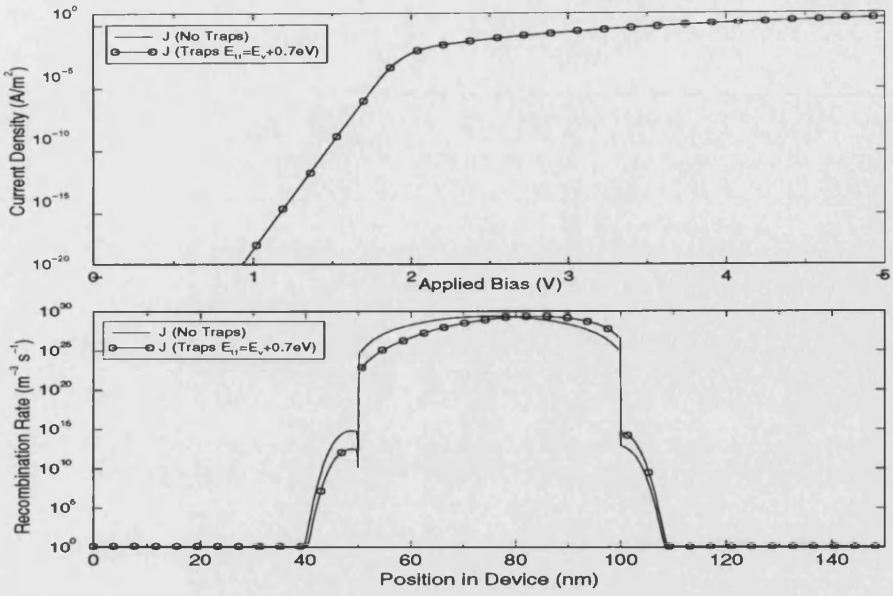

Figure 6.11: JV characteristics (top panel) and recombination profile (bottom panel) for the 3 layer heterostructure device. Material parameters are given in tables 6.2 and 6.3.

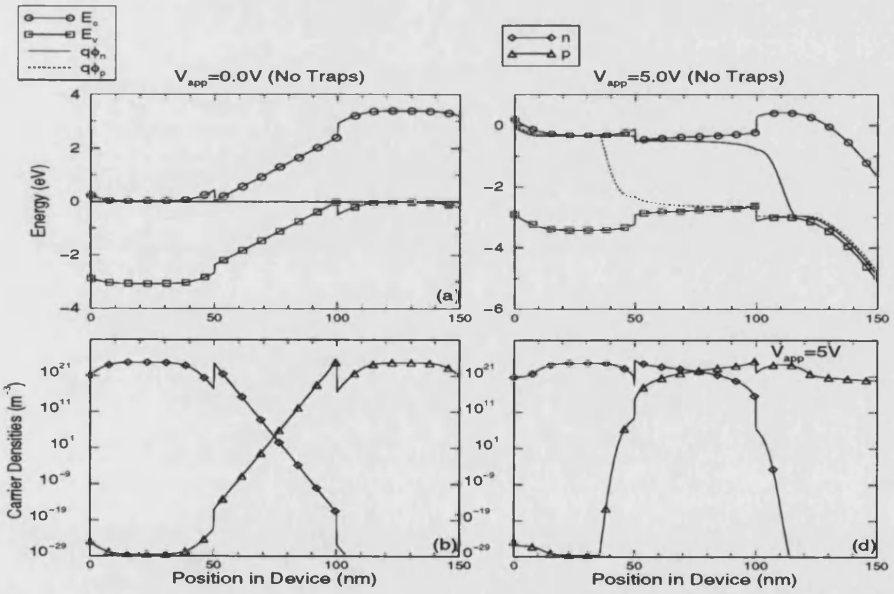

Figure 6.12: Corresponding graph to figure 6.11 showing band structure and recombination profiles for $V_{app} = 0V$ (a) and (b) and $V_{app} = 0V$ (c) and (d) for the trap free case.

6.4 Conclusions

In this chapter the effects of device length, barriers to injection, carrier mobilities and hole trapping in single layer devices have been investigated with a view to de-

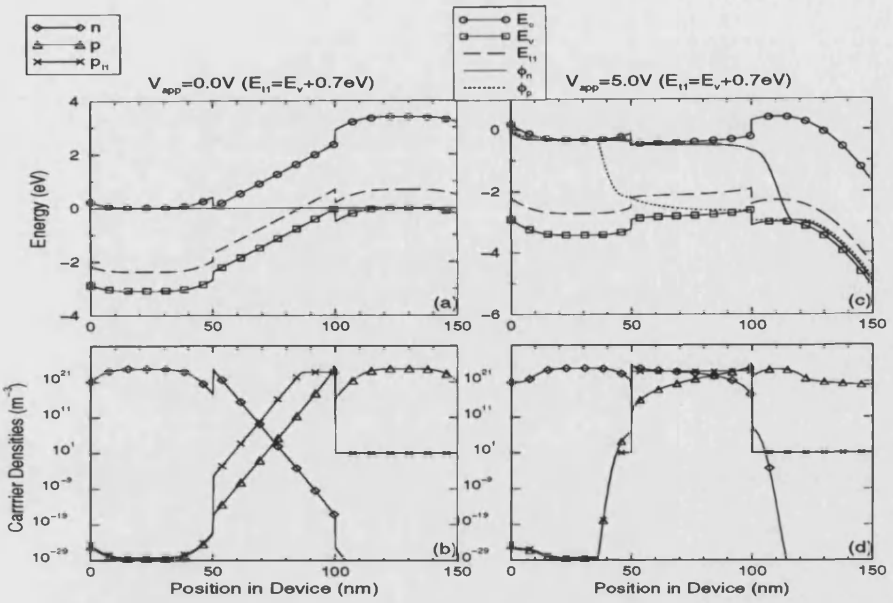

Figure 6.13: Corresponding graph to figure 6.11 showing band structure and recombination profiles for $V_{app} = 0V$ (a) and (b) and $V_{app} = 0V$ (c) and (d) for the hole trapping case.

termining which parameters limit the performance of MEHPPV based OLEDs. It was shown that for realistic mobilities, $\mu_{n0} < \mu_{p0}$, the recombination profile peaks at the LHS electron injection contact due to the low electron mobility. Improved device performance was found for the $\mu_{p0} < \mu_{n0}$ mobility case, although this mobility arrangement is physically unobtainable for current PPV and MEHPPV materials. The effect of increasing the device length reduced both the current density and the recombination rate but had little effect upon the shape of the recombination profiles. The barrier to electron injection controlled the magnitude of the minority carrier density which effectively governs the magnitude of the recombination rate. Like device length, the barrier to electron injection had little effect upon the shape of the recombination profiles.

The effect of hole trapping was investigated for both the realistic mobility case $\mu_{n0} < \mu_{p0}$ and unrealistic mobility case $\mu_{p0} < \mu_{n0}$, using ohmic contacts. These results showed that hole trapping reduced both the magnitude of the current density and the recombination rate. This was due to a lowering of the hole density due to trapping. For the realistic mobility case the JV characteristic showed clear indications of a transition from an ohmic to a trap free square law current in accordance with the single level trap theory outlined in section 2. For the unrealistic mobility case no evidence of trapping was observed in the

JV characteristic, except for a decrease in the current-density when compared with the trap free case. The explanation for this apparent change in device behaviour, between the realistic and unrealistic mobility models, was determined by investigating the carrier densities. For the unrealistic mobility case, hole trapping had reduced the hole density to the extent of making it the minority carrier. Therefore, the device behaviour was governed by the higher mobility electrons.

Results for an optimised device structure were presented for the realistic mobility case. These results showed that increasing the barrier to hole injection ($q\phi_{Bp} =$ 0.3eV) resulted in an improved balance, between the electron and hole densities. This resulted in a recombination profile that was spread evenly through the device structure. The inclusion of hole trapping made little difference to the optimised device performance. Although, the barrier to electron injection was increased to achieved balanced injection, an alternative method could have been to reduce the barrier to electron injection. This approach, should in principle, increase the recombination rate as the electron density will be greatly increased.

The single layer device structures all suffered recombination at one or both injecting contacts, as there is no means of confining the carrier recombination to the centre of the device and away from the contacts. Therefore, a heterostructure device was investigated to achieve carrier confinement. This device consisted of a hypothetical 3 layer heterostructure employing an electron transport layer, a MEHPPV emission layer and a hole transport layer. These results showed that the majority of injected carriers were confined to the emission layer, eliminating the recombination that has been associated with reduced device efficiency. Hole trapping effected the distribution of the hole density in the emission layer but made little difference to the recombination profile. The 3 layer device structure showed a significant improvement in device performance over the single layer devices, although this performance was critically dependent upon the doping concentrations in the transport layers.

References

[1] B. K. Crone, P. S. Davids, I. H. Campbell and D. L. Smith, *Journal of Applied Physics*, **84**, 833-842, 1998.

[2] I. D. Parker, *Journal of Applied Physics*, **75**, 1656-1666, 1993.

[3] A. J. Campbell, D. D. C. Bradley and D. G. Lidzey, *Journal of Applied Physics*, **82**, 6326-6342, 1997.

[4] P. W. M. Blom, M. J. M. Vleggaar, *Applied Physics Letters*, **68**, 3308-3310, 1996.

[5] J. M. Lupton and I. D. W. Samuel, *Journal of Physics D: Applied Physics*, **32**, 2973-2984, 1999.

[6] L. J. Rothberg and A. J. Lovinger, *Journal of Materials Research*, **11**, 3174-3187, 1996.

[7] M. Strukelj, F. Papadimitrakopoulos, T. M. Millar and L. J. Rothberg, *Science*, **267**, 1969-1972, 1995.

Chapter 7

Summary and Future Work

In this chapter we present the results from the work in all previous chapters, and make comments on the usefulness of the research in this thesis. Finally we give ideas of where this work may lead in future.

7.1 Summary of Results

The common theme throughout this thesis has been the numerical modelling of organic electroluminescent devices (OLEDs). Several OLED device structures have been investigated, ranging from single layer majority hole devices to bipolar devices with both homo and heterostructures. Three drift diffusion modelling techniques have been used in this thesis. Two successive over relaxation methods (SOR and Direct) were used, initially to develop a unipolar inorganic model for Schottky contact based structures. However, these two methods were unstable when modelling bipolar devices. The third technique used, based on a first order Newton approach (SOLVDE), proved successful for both inorganic and organic device structures. This method was shown to be both stable and flexible enough to incorporate the organic transport mechanisms, that were outlined in chapter 2. Therefore, the SOLVDE method formed the basis for the work in later chapters.

In chapter 2 several different carrier transport mechanisms were discussed. These can be characterised as either contact limited or bulk limited processes. Possi-

ble contact limited mechanisms include current injection via thermionic emission and, for high fields, Fowler Nordheim tunnelling. Proposed bulk dominated effects are space charge limited current and traps. To date, no single transport mechanism adequately describes the current-voltage characteristic. The most successful methods currently used in modelling OLEDs, use a combination of transport mechanisms including: thermionic emission and field emission, or space charge limited current with carrier trapping.

In chapter 3 a unipolar Schottky contact drift diffusion model (DDM) and a bipolar ohmic contact DDM were shown to be in good agreement with independent numerical and analytical solutions. Although the bipolar ohmic code is stable it is not appropriate for OLEDs, as the injecting contacts on the organic devices have been widely reported to be Schottky in nature. The unipolar Schottky DDM, whilst being stable for these devices structures, proved unstable for bipolar Schottky diode systems

In chapter 4 the first order Newton approach of SOLVDE was shown to be stable for both inorganic and organic devices. This method was in agreement with the analytical and numerical results of chapter 3 for unipolar Schottky diodes and agreement was achieved with published results for a bipolar Schottky diode simulation. The organic modification to the simulation model were detailed and results presented for a single layer organic device.

In chapter 5 two PPV device structures were modelled. The main emphasis of this chapter was to achieve agreement with experimental data over a wide range of operating temperatures. The transport mechanisms for the experimental data were investigated and implemented in the numerical model. Several different approaches were used to fit the experimental data with the best results obtained for the 94nm device using the thermally activated hole mobility model.

However, the 125nm device structure proved more difficult to model. The experimental data indicated that the hole mobility had two distinct regions of operation. At low fields, the field dependence reduced with decreased simulation temperatures, and for high fields increased with decreasing temperature. This behaviour is not predicted by the thermally activated hole mobility model.

The most significant problem encountered when modelling these device structures

was the number of ill-defined parameters that could significantly affect the device behaviour. Additionally, the material properties appear to be dependent upon the purity and synthesis route in manufacturing the experimental devices. These problems make device performance and transport prediction very difficult without first studying the experimental data for the structure.

In chapter 6 the effects of device length, barriers to injection, carrier mobilities and hole trapping in single layer devices were investigated with a view to determining which parameters limit the performance of MEHPPV based OLEDs. It was shown that the more realistic case $\mu_{n0} < \mu_{p0}$, the recombination profile peaked at the LHS electron injection contact due to the low electron mobility. Improved device performance was found for $\mu_{p0} < \mu_{n0}$, although this mobility arrangement is physically unobtainable for current PPV and MEHPPV materials. The effect of increasing the device length reduced both the current density and the recombination rate but had little effect upon the shape of the recombination profiles.

The effect of hole trapping was investigated for both the realistic mobility case, $\mu_{n0} < \mu_{p0}$, and unrealistic mobility case, $\mu_{p0} < \mu_{n0}$, using ohmic contacts. These results showed that hole trapping reduced both the magnitude of the current density and the recombination rate. This was due to a lowering of the hole density due to trapping. For the realistic mobility case the JV characteristic showed clear indications of a transition from an ohmic to a trap free square law current in accordance with the single level trap theory outlined in section 2. For the unrealistic mobility case no evidence of trapping was observed in the JV characteristic, except for a decrease in the current-density when compared with the trap free case.

Results for an optimised device structure were presented for the realistic mobility case. These results showed that increasing the barrier to hole injection ($q\phi_{Bp} = 0.3$eV) resulted in an improved balance, between the electron and hole densities. This resulted in a recombination profile that was spread evenly through the device structure. The inclusion of hole trapping made little difference to the optimised device performance. Although, the barrier to hole injection was increased to achieved balanced injection, an alternative method could have been to reduce the barrier to electron injection. This approach, should in principle, increase the recombination rate as the electron density will be greatly increased.

The single layer device structures all suffered recombination at one or both injecting contacts, as there is no means of confining the carrier recombination to the centre of the device and away from the contacts. Therefore, a heterostructure device was investigated to achieve carrier confinement. This device consisted of a hypothetical 3 layer heterostructure employing a LHS electron transport layer, a MEHPPV emission layer and a hole transport layer. These results showed that the majority of injected carriers were confined to the emission layer, eliminating the recombination that has been associated with reduced device efficiency. Hole trapping effected the distribution of the hole density in the emission layer but made little difference to the recombination profile. The 3 layer device structure showed a significant improvement in device performance over the single layer devices, although this performance was critically dependent upon the doping concentrations in the transport layers.

7.2 Future Work

Although the device model is largely complete, several key areas could be improved upon:

1. Incorporate continuous trap distribution in energy for both holes and electrons;
2. Fully incorporate the tunnelling transport mechanisms with image force effects into the dual Schottky model;
3. Incorporate quantum efficiency and power efficiency into the model;
4. Improve the stability of the solver for small barriers to injection ($\phi_{Bn} <$ 0.1eV);
5. Incorporate tunnelling into the inorganic model.

The OLED device model is currently being used to model various polymer and low molecular weight organic material devices, and several of the points raised above have already been addressed. Although the main emphasis of this thesis has been the modelling of OLEDs, the code was written to be as general as possible.

The inorganic device model has, to date, been used only for comparison with published analytical and numerical models, although it contains virtually all the transport mechanisms of the organic model. Therefore, the inorganic numerical model may prove useful for investigating inorganic device structures based on Schottky contacts or ohmic contacts.

Appendix A

Performance Benchmarks

In this appendix, simulation times for both inorganic and organic single layer device structures, will be presented. The SOLVDE and Direct simulations methods will be benchmarked for various transport mechanisms: including thermionic emission diffusion, barrier lowering, carrier trapping and field emission.

A.1 Reference Machine and Operating System

The computer hardware configuration is detailed below in table A.1 with the operating system and compiler options shown in table A.2

Hardware Component	Information
Supplier	Gateway G6-266
Processor	PII 266MHz
Memory	128Mb (DIMM 66MHz)
Graphics Card	STB NVIDIA (4Mb)
Hard Drive	Western Digital UATA 8Gb
Mother Board	Pentium II LX

Table A.1: Benchmark machine: Hardware configuration.

Software Component	Supplier	Information
Operating System	SuSE	Linux 6.3 (Custom installation)
Fortran Complier	GNU	g77 (v0.5.24)
C Compiler	GNU	gcc & g++ (egcs-1.1.2)
Compiler Flags	N/A	-03
X windows	XFREE86	v3.3.5 (Resolution 1152x664)

Table A.2: Benchmark machine: Operating system and compiler configuration.

A.2 Inorganic Device Structures

For the Direct numerical method, only thermionic emission diffusion is possible. This method can be used in two ways, either to iteratively generate the current-voltage characteristic or alternatively to step abruptly to the desired applied bias. However, the SOLVDE method can only be used in an iterative method. Therefore, for the Direct method both the iterative and abrupt simulation times will be included.

The material parameters and device used in these benchmarks are shown in table A.3 with the benchmark times given in table A.4. The device structure consists of a left hand side Schottky contact, a GaAs material layer and a right hand side ohmic contact.

A.3 Organic Device Structures

For the organic device benchmarks only the SOLVDE numerical method is possible. These results indicate the average simulation times for a single layer device, based on the MEHPPV organic material, for a variety of transport mechanisms. The material and simulation parameters are shown in table A.5 with the benchmark results in A.6. The device structure consists of a left hand side Schottky contact, a PPV material layer and a right hand side Schottky contact.

Parameter	Value	Units
N° Mesh Points	101	-
N° Voltage Steps	50	-
E_{t1}	1.1	eV
P_{t1}	1x10^{21}	m^{-3}
g	1.0	-
T	300	K
L	1.0	μm
ϵ	13.1	-
N_d	1x10^{22}	m^{-3}
N_c	4.7x10^{23}	m^{-3}
N_v	7.0x10^{24}	m^{-3}
μ_n	0.85	m^2/(Vs)
μ_p	0.04	m^2/(Vs)
E_g	1.424	eV
χ_c	4.07	eV
m_e^*	0.067	-
m_h^*	0.47	-
$q\phi_{Bn}$	0.73	eV

Table A.3: Material and simulation parameters.

Simulation Options	SOLVDE Times	Direct Times
Abrupt IV Curve	N/A	0:4.76
Barrier Lowering off	0:5.06	1:15.25
Barrier Lowering on	0:5.11	N/A
Barrier Lowering off Traps on	0:5.87	N/A
Barrier Lowering on Traps on	0:5.89	N/A

Table A.4: Benchmark results.

Parameter	Value	Units
N° Mesh Points	1001	-
N° Voltage Steps	801	-
E_{t1}	1.7	eV
P_{t1}	$1x10^{21}$	m^{-3}
g	1.0	-
T	290	K
L	1.0	nm
ϵ	3.0	-
N_d	0	m^{-3}
N_c	$1x10^{24}$	m^{-3}
N_v	$1x10^{24}$	m^{-3}
μ_n	$1x10^{-10}$	$m^2/(Vs)$
μ_p	$1x10^{-10}$	$m^2/(Vs)$
E_g	2.4	eV
χ_c	2.05	eV
m_e^*	1.0	-
m_h^*	1.0	-
$q\phi_{Bn}$	1.6	eV
$q\phi_{Bn}$	0.2	eV

Table A.5: Material and simulation parameters.

Simulation Options	SOLVDE Times
Barrier Lowering off Tunnelling off	5:38.38
Barrier Lowering on Tunnelling off	5:36.44
Barrier Lowering off Tunnelling on	5:33.77
Barrier Lowering off Tunnelling off Traps on	6:10.34
Barrier Lowering on Tunnelling off Traps on	6:56.80
Barrier Lowering off Tunnelling on Traps on	6:09.75

Table A.6: Benchmark results.

Appendix B

SOLVDE: Double Schottky Equations

In this appendix the E's, S's and y's will be defined for a double Schottky contact organic device. These can then be generalised for ohmic contacts and other transport mechanisms by reording the y's and E's in accordance with chapter 4. The equations presented are for n-type material with field dependent mobilities, bimolecular and SRH recombination and barrier height lowering.

B.1 Equations to be Solved

$$\begin{aligned}
\frac{\mathrm{d}J_n}{\mathrm{d}x} &= -q\Delta G \\
\frac{\mathrm{d}J_p}{\mathrm{d}x} &= q\Delta G \\
\frac{\mathrm{d}D}{\mathrm{d}x} &= q\left[\bar{p} - \bar{n} + N_D^+ - N_A^-\right] \\
J_n &= -q\mu_n \bar{n}\frac{\mathrm{d}\phi_n}{\mathrm{d}x} \\
J_p &= -q\mu_p \bar{p}\frac{\mathrm{d}\phi_p}{\mathrm{d}x} \\
D &= -\epsilon_s\epsilon_0\frac{\mathrm{d}\psi}{\mathrm{d}x}
\end{aligned}$$

B.1.1 Discretised Equations and y's

$$
\begin{aligned}
E_{1,k} &= y_{2,k} - y_{2,k-1} + q\Delta x \Delta G \\
E_{2,k} &= y_{2,k} - y_{2,k-1} - q\Delta x \Delta G \\
E_{3,k} &= y_{4,k} - y_{4,k-1} - q\Delta x \left(\bar{p} - \bar{n} + \mathcal{N}\right) \\
E_{4,k} &= \left(y_{2,k} + y_{2,k-1}\right)\frac{\Delta x}{2} + q\mu_n \bar{n}\left(y_{5,k} - y_{5,k-1}\right) \\
E_{5,k} &= \left(y_{3,k} + y_{3,k-1}\right)\frac{\Delta x}{2} + q\mu_p \bar{p}\left(y_{6,k} - y_{6,k-1}\right) \\
E_{6,k} &= \left(y_{4,k} + y_{4,k-1}\right)\frac{\Delta x}{2} + \epsilon_0 \epsilon_s \left(y_{1,k} - y_{1,k-1}\right)
\end{aligned}
$$

$$
\begin{aligned}
y_{1,k} &= \psi(x_k) \\
y_{2,k} &= J_n(x_k) \\
y_{3,k} &= J_p(x_k) \\
y_{4,k} &= D(x_k) \\
y_{5,k} &= \phi_n(x_k) \\
y_{6,k} &= \phi_p(x_k)
\end{aligned}
$$

B.2 S Matrices at Internal Mesh Points

j=1

$$
\begin{aligned}
S_{1,1} &= \frac{\partial E_{1,k}}{\partial y_{1,k-1}} = q\Delta x \left(\frac{\partial \Delta G}{\partial \bar{n}}\frac{\partial \bar{n}}{\partial \bar{\psi}} + \frac{\partial \Delta G}{\partial \bar{p}}\frac{\partial \bar{p}}{\partial \bar{\psi}}\right) \\
S_{1,2} &= \frac{\partial E_{1,k}}{\partial y_{2,k-1}} = -1 \\
S_{1,3} &= \frac{\partial E_{1,k}}{\partial y_{3,k-1}} = 0 \\
S_{1,4} &= \frac{\partial E_{1,k}}{\partial y_{4,k-1}} = q\Delta x \frac{\partial \Delta G}{\partial |D|} = -q\Delta x \frac{\partial R_{opt}}{\partial |D|}
\end{aligned}
$$

$$
\begin{aligned}
S_{1,5} &= \frac{\partial E_{1,k}}{\partial y_{5,k-1}} = q\Delta x \frac{\partial \Delta G}{\partial \bar{n}} \frac{\partial \bar{n}}{\partial \bar{\phi}_n} \\
S_{1,6} &= \frac{\partial E_{1,k}}{\partial y_{6,k-1}} = q\Delta x \frac{\partial \Delta G}{\partial \bar{p}} \frac{\partial \bar{p}}{\partial \bar{\phi}_p} \\
S_{1,7} &= \frac{\partial E_{1,k}}{\partial y_{1,k}} = S_{1,1} \\
S_{1,8} &= \frac{\partial E_{1,k}}{\partial y_{2,k}} = -S_{1,2} \\
S_{1,9} &= \frac{\partial E_{1,k}}{\partial y_{3,k}} = 0 \\
S_{1,10} &= \frac{\partial E_{1,k}}{\partial y_{4,k}} = S_{1,4} \\
S_{1,11} &= \frac{\partial E_{1,k}}{\partial y_{5,k}} = S_{1,5} \\
S_{1,12} &= \frac{\partial E_{1,k}}{\partial y_{6,k}} = S_{1,6}
\end{aligned}
$$

j=2

$$
\begin{aligned}
S_{2,1} &= \frac{\partial E_{2,k}}{\partial y_{1,k-1}} = -q\Delta x \left(\frac{\partial \Delta G}{\partial \bar{n}} \frac{\partial \bar{n}}{\partial \bar{\psi}} + \frac{\partial \Delta G}{\partial \bar{p}} \frac{\partial \bar{p}}{\partial \bar{\psi}} \right) \\
S_{2,2} &= \frac{\partial E_{2,k}}{\partial y_{2,k-1}} = 0 \\
S_{2,3} &= \frac{\partial E_{2,k}}{\partial y_{3,k-1}} = -1 \\
S_{2,4} &= \frac{\partial E_{2,k}}{\partial y_{4,k-1}} = -q\Delta x \frac{\partial \Delta G}{\partial |D|} = q\Delta x \frac{\partial R_{opt}}{\partial |D|} \\
S_{2,5} &= \frac{\partial E_{2,k}}{\partial y_{5,k-1}} = -q\Delta x \frac{\partial \Delta G}{\partial \bar{n}} \frac{\partial \bar{n}}{\partial \bar{\phi}_n} \\
S_{2,6} &= \frac{\partial E_{2,k}}{\partial y_{6,k-1}} = -q\Delta x \frac{\partial \Delta G}{\partial \bar{p}} \frac{\partial \bar{p}}{\partial \bar{\phi}_p} \\
S_{2,7} &= \frac{\partial E_{2,k}}{\partial y_{1,k}} = S_{2,1} \\
S_{2,8} &= \frac{\partial E_{2,k}}{\partial y_{2,k}} = 0 \\
S_{2,9} &= \frac{\partial E_{2,k}}{\partial y_{3,k}} = -S_{2,3} \\
S_{2,10} &= \frac{\partial E_{2,k}}{\partial y_{4,k}} = S_{2,4}
\end{aligned}
$$

$$S_{2,11} = \frac{\partial E_{2,k}}{\partial y_{5,k}} = S_{2,5}$$
$$S_{2,12} = \frac{\partial E_{2,k}}{\partial y_{6,k}} = S_{2,6}$$

j=3

$$S_{3,1} = \frac{\partial E_{3,k}}{\partial y_{1,k-1}} = -q\Delta x \left(\frac{\partial \bar{p}}{\partial \bar{\psi}} - \frac{\partial \bar{n}}{\partial \bar{\psi}} \right)$$
$$S_{3,2} = \frac{\partial E_{3,k}}{\partial y_{2,k-1}} = 0$$
$$S_{3,3} = \frac{\partial E_{3,k}}{\partial y_{3,k-1}} = 0$$
$$S_{3,4} = \frac{\partial E_{3,k}}{\partial y_{4,k-1}} = -1$$
$$S_{3,5} = \frac{\partial E_{3,k}}{\partial y_{5,k-1}} = q\Delta x \frac{\partial \bar{n}}{\partial \bar{\phi}_n}$$
$$S_{3,6} = \frac{\partial E_{3,k}}{\partial y_{6,k-1}} = -q\Delta x \frac{\partial \bar{p}}{\partial \bar{\phi}_p}$$
$$S_{3,7} = \frac{\partial E_{3,k}}{\partial y_{1,k}} = S_{3,1}$$
$$S_{3,8} = \frac{\partial E_{3,k}}{\partial y_{2,k}} = 0$$
$$S_{3,9} = \frac{\partial E_{3,k}}{\partial y_{3,k}} = 0$$
$$S_{3,10} = \frac{\partial E_{3,k}}{\partial y_{4,k}} = -S_{3,4}$$
$$S_{3,11} = \frac{\partial E_{3,k}}{\partial y_{5,k}} = S_{3,5}$$
$$S_{3,12} = \frac{\partial E_{3,k}}{\partial y_{6,k}} = S_{3,6}$$

j=4

$$S_{4,1} = \frac{\partial E_{4,k}}{\partial y_{1,k-1}} = q\mu_n \left(y_{5,k} - y_{5,k-1} \right) \frac{\partial \bar{n}}{\partial \bar{\psi}}$$

$$
\begin{aligned}
S_{4,2} &= \frac{\partial E_{4,k}}{\partial y_{2,k-1}} = \frac{\Delta x}{2} \\
S_{4,3} &= \frac{\partial E_{4,k}}{\partial y_{3,k-1}} = 0 \\
S_{4,4} &= \frac{\partial E_{4,k}}{\partial y_{4,k-1}} = q\bar{n}\left(y_{5,k} - y_{5,k-1}\right)\frac{\partial(\mu_n)}{\partial|D|} \\
S_{4,5} &= \frac{\partial E_{4,k}}{\partial y_{5,k-1}} = q\mu_n\frac{\partial}{\partial\bar{\phi}_n}\left(y_{5,k}\bar{n} - y_{5,k-1}\bar{n}\right) \\
S_{4,6} &= \frac{\partial E_{4,k}}{\partial y_{6,k-1}} = 0 \\
S_{4,7} &= \frac{\partial E_{4,k}}{\partial y_{1,k}} = S_{4,1} \\
S_{4,8} &= \frac{\partial E_{4,k}}{\partial y_{2,k}} = S_{4,2} \\
S_{4,9} &= \frac{\partial E_{4,k}}{\partial y_{3,k}} = 0 \\
S_{4,10} &= \frac{\partial E_{4,k}}{\partial y_{4,k}} = S_{4,4} \\
S_{4,11} &= \frac{\partial E_{4,k}}{\partial y_{5,k}} = S_{4,5} \\
S_{4,12} &= \frac{\partial E_{4,k}}{\partial y_{6,k}} = 0
\end{aligned}
$$

j=5

$$
\begin{aligned}
S_{5,1} &= \frac{\partial E_{5,k}}{\partial y_{1,k-1}} = q\mu_p\left(y_{6,k} - y_{6,k-1}\right)\frac{\partial\bar{p}}{\partial\bar{\psi}} \\
S_{5,2} &= \frac{\partial E_{5,k}}{\partial y_{2,k-1}} = 0 \\
S_{5,3} &= \frac{\partial E_{5,k}}{\partial y_{3,k-1}} = \frac{\Delta x}{2} \\
S_{5,4} &= \frac{\partial E_{5,k}}{\partial y_{4,k-1}} = q\bar{p}\left(y_{6,k} - y_{6,k-1}\right)\frac{\partial(\mu_p)}{\partial|D|} \\
S_{5,5} &= \frac{\partial E_{5,k}}{\partial y_{5,k-1}} = 0 \\
S_{5,6} &= \frac{\partial E_{5,k}}{\partial y_{6,k-1}} = q\mu_p\frac{\partial}{\partial\bar{\phi}_p}\left(y_{6,k}\bar{p} - y_{6,k-1}\bar{p}\right) \\
S_{5,7} &= \frac{\partial E_{5,k}}{\partial y_{1,k}} = S_{5,1}
\end{aligned}
$$

$$
\begin{aligned}
S_{5,8} &= \frac{\partial E_{5,k}}{\partial y_{2,k}} = 0 \\
S_{5,9} &= \frac{\partial E_{5,k}}{\partial y_{3,k}} = S_{5,3} \\
S_{5,10} &= \frac{\partial E_{5,k}}{\partial y_{4,k}} = S_{5,4} \\
S_{5,11} &= \frac{\partial E_{5,k}}{\partial y_{5,k}} = 0 \\
S_{5,12} &= \frac{\partial E_{5,k}}{\partial y_{6,k}} = S_{5,6}
\end{aligned}
$$

j=6

$$
\begin{aligned}
S_{6,1} &= \frac{\partial E_{6,k}}{\partial y_{1,k-1}} = -\epsilon_o \bar{\epsilon}_s \\
S_{6,2} &= \frac{\partial E_{6,k}}{\partial y_{2,k-1}} = 0 \\
S_{6,3} &= \frac{\partial E_{6,k}}{\partial y_{3,k-1}} = 0 \\
S_{6,4} &= \frac{\partial E_{6,k}}{\partial y_{4,k-1}} = \frac{\Delta x}{2} \\
S_{6,5} &= \frac{\partial E_{6,k}}{\partial y_{5,k-1}} = 0 \\
S_{6,6} &= \frac{\partial E_{6,k}}{\partial y_{6,k-1}} = 0 \\
S_{6,7} &= \frac{\partial E_{6,k}}{\partial y_{1,k}} = -S_{6,1} \\
S_{6,8} &= \frac{\partial E_{6,k}}{\partial y_{2,k}} = 0 \\
S_{6,9} &= \frac{\partial E_{6,k}}{\partial y_{3,k}} = 0 \\
S_{6,10} &= \frac{\partial E_{6,k}}{\partial y_{4,k}} = S_{6,4} \\
S_{6,11} &= \frac{\partial E_{6,k}}{\partial y_{5,k}} = 0 \\
S_{6,12} &= \frac{\partial E_{6,k}}{\partial y_{6,k}} = 0
\end{aligned}
$$

B.3 Useful Derivatives

B.3.1 $\bar{n}$ derivatives

$$\begin{aligned}
\frac{\partial \bar{n}}{\partial \bar{\psi}} &= \frac{\partial \bar{n}}{\partial y_{1,k}} = \frac{\partial \bar{n}}{\partial y_{1,k-1}} = \frac{\beta}{2}\bar{n} \\
\frac{\partial \bar{n}}{\partial J_n} &= \frac{\partial \bar{n}}{\partial y_{2,k}} = \frac{\partial \bar{n}}{\partial y_{2,k-1}} = 0 \\
\frac{\partial \bar{n}}{\partial J_p} &= \frac{\partial \bar{n}}{\partial y_{3,k}} = \frac{\partial \bar{n}}{\partial y_{3,k-1}} = 0 \\
\frac{\partial \bar{n}}{\partial D} &= \frac{\partial \bar{n}}{\partial y_{4,k}} = \frac{\partial \bar{n}}{\partial y_{4,k-1}} = 0 \\
\frac{\partial \bar{n}}{\partial \bar{\phi}_n} &= \frac{\partial \bar{n}}{\partial y_{5,k}} = \frac{\partial \bar{n}}{\partial y_{5,k-1}} = -\frac{\beta}{2}\bar{n} \\
\frac{\partial \bar{n}}{\partial \bar{\phi}_p} &= \frac{\partial \bar{n}}{\partial y_{6,k}} = \frac{\partial \bar{n}}{\partial y_{6,k-1}} = 0
\end{aligned}$$

B.3.2 $\bar{p}$ derivatives

$$\begin{aligned}
\frac{\partial \bar{p}}{\partial \bar{\psi}} &= \frac{\partial \bar{p}}{\partial y_{1,k}} = \frac{\partial \bar{p}}{\partial y_{1,k-1}} = -\frac{\beta}{2}\bar{p} \\
\frac{\partial \bar{p}}{\partial J_n} &= \frac{\partial \bar{p}}{\partial y_{2,k}} = \frac{\partial \bar{p}}{\partial y_{2,k-1}} = 0 \\
\frac{\partial \bar{p}}{\partial J_p} &= \frac{\partial \bar{p}}{\partial y_{3,k}} = \frac{\partial \bar{p}}{\partial y_{3,k-1}} = 0 \\
\frac{\partial \bar{p}}{\partial D} &= \frac{\partial \bar{p}}{\partial y_{4,k}} = \frac{\partial \bar{p}}{\partial y_{4,k-1}} = 0 \\
\frac{\partial \bar{p}}{\partial \bar{\phi}_n} &= \frac{\partial \bar{p}}{\partial y_{5,k}} = \frac{\partial \bar{p}}{\partial y_{5,k-1}} = 0 \\
\frac{\partial \bar{p}}{\partial \bar{\phi}_p} &= \frac{\partial \bar{p}}{\partial y_{6,k}} = \frac{\partial \bar{p}}{\partial y_{6,k-1}} = \frac{\beta}{2}\bar{p}
\end{aligned}$$

B.3.3 ΔG derivatives (SRH)

$$
\begin{aligned}
\Delta G &= G(x) - R(x) \\
\\
R &= \frac{(\bar{n}\bar{p} - \bar{n}_i^2)}{D} \\
D &= (\bar{n} + \bar{n}_i)\,\bar{\tau}_p + (\bar{p} + \bar{n}_i)\,\bar{\tau}_n
\end{aligned}
$$

$$
\begin{aligned}
\frac{\partial \Delta G}{\partial \bar{n}} &= -\frac{\partial R}{\partial \bar{n}} = \frac{\bar{\tau}_p R - \bar{p}}{D} \\
\frac{\partial \Delta G}{\partial \bar{p}} &= -\frac{\partial R}{\partial \bar{p}} = \frac{\bar{\tau}_n R - \bar{n}}{D}
\end{aligned}
$$

$$
\begin{aligned}
\frac{\partial \Delta G}{\partial \bar{\psi}} &= \frac{\partial \Delta G}{\partial y_{1,k}} = \frac{\partial \Delta G}{\partial y_{1,k-1}} = \frac{\partial \Delta G}{\partial \bar{n}}\frac{\partial \bar{n}}{\partial \bar{\psi}} + \frac{\partial \Delta G}{\partial \bar{p}}\frac{\partial \bar{p}}{\partial \bar{\psi}} \\
\frac{\partial \Delta G}{\partial \bar{\phi}_n} &= \frac{\partial \Delta G}{\partial y_{5,k}} = \frac{\partial \Delta G}{\partial y_{5,k-1}} = \frac{\partial \Delta G}{\partial \bar{n}}\frac{\partial \bar{p}}{\partial \bar{\phi}_n} \\
\frac{\partial \Delta G}{\partial \bar{\phi}_p} &= \frac{\partial \Delta G}{\partial y_{6,k}} = \frac{\partial \Delta G}{\partial y_{6,k-1}} = \frac{\partial \Delta G}{\partial \bar{p}}\frac{\partial \bar{p}}{\partial \bar{\phi}_p}
\end{aligned}
$$

B.3.4 ΔG derivatives (OPT)

$$
\begin{aligned}
\Delta G &= G(x) - R_{opt}(x) \\
\\
R_{opt} &= \lambda\left(\bar{n}\bar{p} - \bar{n}_i^2\right) \\
\\
\lambda &= \frac{q4\pi\mu_0}{\epsilon_0\epsilon_s}\exp\left(\sqrt{\frac{|D|}{D_0}}\right)
\end{aligned}
$$

$$
\begin{aligned}
\frac{\partial \Delta G}{\partial \bar{n}} &= -\frac{\partial R_{opt}}{\partial \bar{n}} = \lambda\frac{\beta}{2}\bar{p} \\
\frac{\partial \Delta G}{\partial \bar{p}} &= -\frac{\partial R_{opt}}{\partial \bar{p}} = \lambda\frac{\beta}{2}\bar{n} \\
\frac{\partial \Delta G}{\partial \bar{p}} &= -\frac{\partial R_{opt}}{\partial |D|} = \frac{\lambda}{2\sqrt{|D|}}
\end{aligned}
$$

$$
\begin{aligned}
\frac{\partial \Delta G}{\partial \bar{\psi}} &= \frac{\partial \Delta G}{\partial y_{1,k}} = \frac{\partial \Delta G}{\partial y_{1,k-1}} = \frac{\partial \Delta G}{\partial \bar{n}} \frac{\partial \bar{n}}{\partial \bar{\psi}} + \frac{\partial \Delta G}{\partial \bar{p}} \frac{\partial \bar{p}}{\partial \bar{\psi}} \\
\frac{\partial \Delta G}{\partial \bar{\phi}_n} &= \frac{\partial \Delta G}{\partial y_{5,k}} = \frac{\partial \Delta G}{\partial y_{5,k-1}} = \frac{\partial \Delta G}{\partial \bar{n}} \frac{\partial \bar{p}}{\partial \bar{\phi}_n} \\
\frac{\partial \Delta G}{\partial \bar{\phi}_p} &= \frac{\partial \Delta G}{\partial y_{6,k}} = \frac{\partial \Delta G}{\partial y_{6,k-1}} = \frac{\partial \Delta G}{\partial \bar{p}} \frac{\partial \bar{p}}{\partial \bar{\phi}_p}
\end{aligned}
$$

B.4 S's Matrices at Boundary Mesh Points

B.4.1 Boundary Equations

Device material is n-type, bias is applied on the RHS. Barrier height lowering and field dependent mobilities are on.

LHS Contact $(S_{1,jsf} = S_{2,jsf} = S_{3,jsf} = 0)$

$$
\begin{aligned}
E_{4,1} &= y_{1,k1} - \psi(k1) - \Delta\phi_{Bn} \\
E_{5,1} &= y_{2,k1} - qV_{rn}(k1)n_{eq}(k1)\mu_n(k1)\left[\exp\left(-\beta y_{5,k1}\right) - 1\right]\exp\left(\beta\Delta\phi_{Bn}\right) \\
E_{6,1} &= y_{3,k1} + qV_{rp}(k1)p_{eq}(k1)\mu_p(k1)\left[\exp\left(\beta y_{6,k1}\right) - 1\right]\exp\left(-\beta\Delta\phi_{Bn}\right)
\end{aligned}
$$

$$
\Delta\phi_{Bn} = \begin{cases} \sqrt{\frac{q|y_{4,k1}|}{4\pi(\epsilon_0\epsilon_s)^2}} & : \quad y_{4,k1} \leq 0 \\ 0 & : \quad y_{4,k1} > 0 \end{cases} \tag{B.1}
$$

RHS Contact $(S_{4,jsf} = S_{5,jsf} = S_{6,jsf} = 0)$

$$
\begin{aligned}
E_{1,1} &= y_{1,k2} - \psi(k2) - \Delta\phi_{Bn} \\
E_{2,1} &= y_{2,k2} + qV_{rn}(k2)n_{eq}(k2)\mu_n(k2)\left[\exp\left(-\beta(y_{5,k2} + V_{app})\right) - 1\right]\exp\left(\beta\Delta\phi_{Bn}\right) \\
E_{3,1} &= y_{3,k2} - qV_{rp}(k2)p_{eq}(k2)\mu_p(k2)\left[\exp\left(\beta(y_{6,k2} + V_{app})\right) - 1\right]\exp\left(-\beta\Delta\phi_{Bn}\right)
\end{aligned}
$$

$$\Delta\phi_{Bn} = \begin{cases} \sqrt{\frac{q|y_{4,k2}|}{4\pi(\epsilon_0\epsilon_s)^2}} & : \quad y_{4,k2} \geq 0 \\ 0 & : \quad y_{4,k2} < 0 \end{cases} \tag{B.2}$$

B.4.2 Derivatives

k1=1 and **k2=M+1** where M is the number of mesh points.

All S matrices are zero except those specified

LHS Contact

$$S_{4,7} = \frac{\partial E_{4,1}}{\partial y_{1,k1}} = 1$$

$$S_{4,10} = \frac{\partial E_{5,1}}{\partial y_{4,k1}} = -\frac{\partial}{\partial y_{4,k1}}(\Delta\phi_{Bn})$$

$$S_{5,8} = \frac{\partial E_{5,1}}{\partial y_{2,k1}} = 1$$

$$S_{5,10} = \frac{\partial E_{5,1}}{\partial y_{4,k1}} = -qV_{rn}(k1)n_{eq}(k1)\left[\exp\left(-\beta y_{5,k1}\right) - 1\right]\frac{\partial}{\partial y_{4,k1}}\left(\mu_n(k1)\exp\left(\beta\Delta\phi_{Bn}\right)\right)$$

$$S_{5,11} = \frac{\partial E_{5,1}}{\partial y_{5,k1}} = -qV_{rn}(k1)n_{eq}(k1)\mu_n(k1)\exp\left(\beta\Delta\phi_{Bn}\right)\frac{\partial}{\partial y_{5,k1}}\left(\exp\left(-\beta y_{5,k1}\right) - 1\right)$$

$$S_{6,9} = \frac{\partial E_{6,1}}{\partial y_{3,k1}} = 1$$

$$S_{6,10} = \frac{\partial E_{6,1}}{\partial y_{4,k1}} = qV_{rp}(k1)p_{eq}(k1)\left[\exp\left(\beta y_{6,k1}\right) - 1\right]\frac{\partial}{\partial y_{4,k1}}\left(\mu_p(k1)\exp\left(-\beta\Delta\phi_{Bn}\right)\right)$$

$$S_{6,12} = \frac{\partial E_{6,1}}{\partial y_{6,k1}} = qV_{rp}(k1)p_{eq}(k1)\mu_p(k1)\exp\left(-\beta\Delta\phi_{Bn}\right)\frac{\partial}{\partial y_{6,k1}}\left(\exp\left(\beta y_{6,k1}\right) - 1\right)$$

RHS Contact

$$S_{1,7} = \frac{\partial E_{1,1}}{\partial y_{1,k1}} = 1$$

$$S_{1,10} = \frac{\partial E_{1,1}}{\partial y_{4,k1}} = -\frac{\partial}{\partial y_{4,k1}}(\Delta\phi_{Bn})$$

$$
\begin{aligned}
S_{2,8} &= \frac{\partial E_{5,1}}{\partial y_{2,k1}} = 1 \\
S_{2,10} &= \frac{\partial E_{5,1}}{\partial y_{4,k1}} = qV_{rn}(k1)n_{eq}(k1)\left[\exp\left(-\beta(y_{5,k1}+V_{app})\right)-1\right]\frac{\partial}{\partial y_{4,k1}}\left(\mu_n(k1)\exp\left(\beta\Delta\phi_{Bn}\right)\right) \\
S_{2,11} &= \frac{\partial E_{5,1}}{\partial y_{5,k1}} = qV_{rn}(k1)n_{eq}(k1)\mu_n(k1)\exp\left(\beta\Delta\phi_{Bn}\right)\frac{\partial}{\partial y_{5,k1}}\left(\exp\left(-\beta(y_{5,k1}+V_{app})\right)-1\right) \\
S_{3,9} &= \frac{\partial E_{6,1}}{\partial y_{3,k1}} = 1 \\
S_{3,10} &= \frac{\partial E_{6,1}}{\partial y_{4,k1}} = -qV_{rp}(k1)p_{eq}(k1)\left[\exp\left(\beta(y_{6,k1}+V_{app})\right)-1\right]\frac{\partial}{\partial y_{4,k1}}\left(\mu_p(k1)\exp\left(-\beta\Delta\phi_{Bn}\right)\right) \\
S_{3,12} &= \frac{\partial E_{6,1}}{\partial y_{6,k1}} = -qV_{rp}(k1)p_{eq}(k1)\mu_p(k1)\exp\left(-\beta\Delta\phi_{Bn}\right)\frac{\partial}{\partial y_{6,k1}}\left(\exp\left(\beta(y_{6,k1}+V_{app})\right)-1\right)
\end{aligned}
$$